

Accepted Manuscript

Geological Society, London, Memoirs

Antarctic Upper Mantle Rheology

E. R. Ivins, W. van der Wal, D. A. Wiens, A. J. Lloyd & L. Caron

DOI: <https://doi.org/10.1144/M56-2020-19>

To access the most recent version of this article, please click the DOI URL in the line above. When citing this article please include the above DOI.

Received 29 July 2020

Revised 17 February 2021

Accepted 17 February 2021

© 2021 Jet Propulsion Laboratory, California Institute of Technology. This is an Open Access article distributed under the terms of the Creative Commons Attribution 4.0 License (<http://creativecommons.org/licenses/by/4.0/>). Published by The Geological Society of London. Publishing disclaimer: www.geolsoc.org.uk/pub_ethics

Manuscript version: Accepted Manuscript

This is a PDF of an unedited manuscript that has been accepted for publication. The manuscript will undergo copyediting, typesetting and correction before it is published in its final form. Please note that during the production process errors may be discovered which could affect the content, and all legal disclaimers that apply to the book series pertain.

Although reasonable efforts have been made to obtain all necessary permissions from third parties to include their copyrighted content within this article, their full citation and copyright line may not be present in this Accepted Manuscript version. Before using any content from this article, please refer to the Version of Record once published for full citation and copyright details, as permissions may be required.

Antarctic Upper Mantle Rheology

E. R. Ivins¹

ORCHID ID 0000-0003-0148-357X

W. van der Wal²

ORCHID ID 0000-0001-8030-9080

D. A. Wiens³

ORCHID ID 0000-0002-5169-4386

A. J. Lloyd⁴

ORCHID ID 0000-0002-2253-1342

and L. Caron^{1,5}

ORCHID ID 0000-0001-8946-1222

¹Jet Propulsion Laboratory, California Institute of Technology, Pasadena, CA, 91109, USA

²Faculty of Aerospace Engineering, Delft University of Technology, Delft, The Netherlands

³Department of Earth and Planetary Sciences, Washington University, St. Louis, MO, 63130, USA

⁴Lamont Doherty Earth Observatory, Columbia University, Palisades, NY 10964, USA

⁵JIFRESS, University of California at Los Angeles, Los Angeles, CA, 90095, USA

Abstract

The Antarctic mantle and lithosphere are known to have large lateral contrasts in seismic velocity and tectonic history. These contrasts suggest differences in the response time scale of mantle flow across the continent, similar to those documented between the northeastern and southwestern upper mantle of North America. Glacial isostatic adjustment and geodynamical modeling rely on independent estimates of lateral variability in effective viscosity. Recent improvements in imaging techniques and the distribution of seismic stations now allow resolution of both lateral and vertical variability of seismic velocity, making detailed inferences about lateral viscosity variations possible. Geodetic and paleo sea-level investigations of Antarctica provide quantitative ways of independently assessing the three-dimensional mantle viscosity structure. While observational and causal connections between inferred lateral viscosity variability and seismic velocity changes are qualitatively reconciled, significant improvements in the quantitative relations between effective viscosity anomalies and those imaged by P- and S-wave tomography have remained elusive. Here we describe several methods for estimating effective viscosity from S-wave velocity. We then present and compare maps of the viscosity variability beneath Antarctica based on the recent S-wave velocity model ANT-20 using three different approaches.

1 Introduction

Solid Earth *rheology* is that discipline which deals with the laws that govern the deformation of rocks under the high temperature and pressure conditions of the mantle. Observations linked to rheology require input from many disciplines in the geological and geophysical sciences, and examples include composition, temperature and pressure conditions from xenoliths, elastic parameters from seismic wave propagation, and density variations derived from gravity, topography and magnetic anomaly data (e.g., Scheinert et al., 2016; Martos et al., 2017; Pappa et al., 2019). Simulations of mantle circulation (Bredow and Steinberger, this volume), glacial isostatic adjustment (GIA), post-seismic deformation

(Barletta and Nield, this volume) and their surface expressions, require quantifying large variations in mantle rheology. For several areas of the world we have some quantitative bounds on lateral variability in upper mantle viscosity, such as the contrast between Fennoscandia and Iceland (H. Wang et al., 2008). Antarctica has long been known to have contrasting mantle and lithosphere properties between east and west, somewhat akin to the contrasts between the Precambrian craton of eastern Canada and the geologically younger crust and mantle of western North America (Crittenden, 1963; Austermann et al., 2020).

A broader goal of this Chapter is to make quantitative connections between flow laws derived in the rock deformation laboratory and the integrative power of the data sets for constraining crustal motion and Earth structure using a network of Global Positioning System (GPS) and broadband seismic instruments. A period of intense data collection began after the 4th International Polar Year of 2007 and was organized as the POLENET project. Much of this integrated data set may be brought to bear on understanding the nature of the Antarctic lithosphere (e.g., Shen et al., 2018; Nield et al., 2018). An overview of seismic imaging of the Antarctic crust, lithosphere and upper mantle is given in the Chapter by Wiens et al. (this volume) that includes tectonophysical interpretations, thus complementing the study of Earth rheology. The reader may also find the recent review by Jordan et al. (2020) to be useful. However, in this Chapter we focus on the mantle response to changes in surface ice loading over centennial to millennial time scales with steady-state high-temperature creep. The rate of strain associated with this creep may be causally connected to both vertical uplift and horizontal crustal motion rates that have been measured using bedrock GPS (e.g., James & Ivins, 1995; Groh et al., 2012; Barletta et al., 2018). This motion also occurs where it cannot be measured, deep below the surface of the ice sheet, over extensive regions of the vast ice covered interior. Such extensive continental-scale mantle and crustal motion is important to model since the vertical component creates a time-varying gravity field. The modeled GIA signal needs to be removed from gravimetry measurements, such that accurate ice mass balance trends for the Antarctic ice sheet and its contribution to ongoing sea-level rise may be retrieved using space gravity mission data (e.g., Caron & Ivins, 2020).

Early surface wave studies in Antarctica (e.g., Knopoff & Vane, 1978; Ritzwoller et al., 2001; Danesi & Morelli, 2001) revealed the existence of a major contrast in the structure of the uppermost 300 km of the mantle between east and west Antarctica. The boundary between these deep structural elements is roughly coincident with the surface expression of the Transantarctic Mountains (TAM see Figure 1). The seismic data retrieved since 2007 are of sufficiently high-quality that we can begin to quantify the lateral heterogeneity in the viscous response of the mantle to ice mass surface load changes. Lateral heterogeneity in the mantle is important for reconciling observed and predicted crustal motion in GIA models (Powell et al., 2020) and is an important aspect for determining the stability of the ice sheet over a changing bed topography, both in the past and in the future (Gomez et al., 2018). Lateral variability in elastic wave velocity (see Figure 1) is related to lateral temperature variations. Using the temperature-dependence of elastic constants and anelasticity determined by theory and experiment we can try to relate seismic velocity change to changes in effective mantle viscosity, since the latter are known to be strongly dependent on temperature.

The focus of this Chapter is to examine the feasibility of developing causal interconnections between seismic tomographic imaging, mantle viscosity retrieved from Maxwellian 1D GIA models, and flow laws for steady-state creep quantified by high pressure and temperature laboratory experiments. This is a rather grand challenge, and may have consequences for regions other than Antarctica. However, here we restrict our study only to a

single tomographic S-wave imaging study (Lloyd et al., 2020) for Antarctica and restrict ourselves to the upper mantle. The feasibility of establishing causal interconnection is tested by conducting an inter-comparison of three methods at three different depths. The methods for each are documented in the remaining pages of this Chapter. In Table 1 we give a short synopsis of some of the differences in the methods. Later we refer to these as Approaches 1, 2 and 3 (see # in Table 1). Not only is the selection of laboratory flow laws generally different, so are the implementation steps yielding anelastic slowing of the shear-wave velocity. The latter are necessary to derive the appropriate thermal deviation $\delta T(r, \theta, \phi)$ from tomography. We anticipate from the outset, that there will be large differences amongst the predictions. These should manifest themselves as differences in mapped $\log_{10}\Delta\eta(r, \theta, \phi)$ for the Antarctic mantle and in comparisons to the inferences from 1-D GIA models compatible with geodetic data.

The scope of study in this Chapter is limited by the fact that Antarctica is an ice sheet covered continent having a logistically difficult environment in which to obtain bedrock GPS, relative sea-level (RSL) data and maintain seismic station operation. We are perhaps blessed by the fact that geochronological and ice core constraints on the ice sheet history during the late-Quaternary place tight constraints on the millennial time-scale ice load history (e.g., Bentley et al., 2014; J. B. Anderson et al., 2014; Whitehouse et al., 2017), a critical ingredient for establishing viable GIA predictions. Neither a comprehensive 3-D compressional (P-wave) map can be combined with S-wave mapping (e.g., Goes et al., 2000), nor does an attenuation map of the upper mantle for Antarctica exist (e.g., Lawrence & Prieto, 2011). This fact diminishes the capability of retrieving higher fidelity mapping of $\delta T(r, \theta, \phi)$ that can be produced in upper mantle environments where seismic station coverage is denser in both space and time (e.g., Goes et al., 2000). Nonetheless, in this Chapter we demonstrate that a coherent rationale exists for quantitatively connecting Antarctic seismic tomography to GIA-determined mantle viscosity and laboratory flow laws. This inference may have impact on the construction of future models of glacial isostatic adjustment with lateral variation in Earth structure (GIA-LV) and for formulating paradigms for their uncertainty.

In this Chapter, we will first review the factors controlling mantle rheology as well as seismic wave velocities in the mantle. We then discuss a general computational strategy for estimating 3-D mantle viscosity from seismic observations and present new maps of viscosity for the Antarctic upper mantle derived in three different ways. In our conclusions we attempt to draw out robust predictions that are common to the three methods. A common starting point for our estimates is the ANT-20 S-wave velocity model (Lloyd et al., 2020). This model takes advantage of recent increases in seismic station density and computational techniques to derive higher resolution images of mantle structure using full waveform adjoint tomography (Wiens et al., this volume). The focus of this Chapter is on the most basic elements of the large uncertainties encountered in deriving viscosity from seismic models. We identify and detail a number of the relevant quantitative elastic and plastic deformation parameters, but assess their relative uncertainty in a more qualitative way. Our main conclusions will, hopefully, offer clarity and guidance for further efforts to reduce this uncertainty and thereby improve our estimation of mantle rheology.

2 Background

Deformation in the mantle is controlled by the mobility of defects in the crystal structure, either within, or at the boundaries of rock grains (Kohlstedt & Hansen, 2015; Masuti et al.,

2019). Therefore, this chapter begins with a brief synopsis of some of the microphysical models derived from laboratory deformation experiments. Such experiments reveal the same defect structures that are found in field samples of mantle rocks (e.g., Matsyuk et al., 1998; Johanesen & Platt, 2015).

While the essence of rock flow at mantle temperature and pressure is to be found microscopically, all geodynamic simulations rely on the continuum hypothesis. This hypothesis asserts that the constitutive law governing the relations between stress and strain, and their time derivatives, are independent of scale. While a computational convenience is to describe mantle flow controlled by a constitutive equation that has an effective Newtonian viscosity, a large body of experimental results suggest a non-Newtonian behavior. Hence, any discussion of Antarctic mantle rheology must probe this issue. Detailed descriptions of the experimental basis of the laws derived from studies of the mechanical strength of mantle rocks at high temperature and pressure is well beyond the scope of this chapter.

Overall, there exists a gap between laboratory-based flow laws and the rheology obtained by models of geodetically measured solid Earth deformation. This gap may only be reconciled by placing both methodologies into a rigorous statistical framework that will define a subset of the flow laws and model predictions that are mutually compatible (e.g., Jain et al., 2019). It is hoped, that by writing this Chapter we can lay some ground work that might further this aim for the Antarctic mantle.

2.1 The Role of Experiments

Figure 2 shows a classic representation of the deformation diagram used in study of mantle rheology to define regimes of control by microscopic mechanisms as they vary with stress, strain rate, temperature, and/or grain-size. Here we show one example of a deformation map produced by Karato (2010) for olivine, a rock type that dominates the mantle above 410 km depth. The portion of the deformation diagram in Figure 2 that shows stress values below 100 MPa corresponds to the regime in which GIA generated stresses occur. GIA stresses may reach 10 MPa in Antarctica near the lithosphere-asthenosphere boundary for realistic ice loading and unloading (e.g., Ivins et al., 2003). In this regime, two microscopic mechanisms may control effective rheology: diffusion or dislocation creep. Later in this Chapter, both of these mechanisms are to play a role in the scaling to S-wave seismic tomography.

There are caveats that are well known when applying experimentally derived flow laws to geodynamic and GIA models. An obvious caveat is the difference between mantle strain rates $\mathcal{O}10^{-15} - 10^{-12} \text{ sec}^{-1}$ and those of the laboratory $\mathcal{O}10^{-6} - 10^{-3} \text{ sec}^{-1}$ (see the light contour lines in Figure 2). (Here the symbol \mathcal{O} indicates 'order of magnitude'). There is the additional caveat that the principal shear stresses are higher in the laboratory (see Figure 2). Some experiments at higher strain rate $\mathcal{O}10^{-3} \text{ sec}^{-1}$ and higher stress $\mathcal{O}80 - 100 \text{ MPa}$ are relevant to shear localization in the lithosphere (e.g., L. N. Hansen et al., 2012). In Figure 2, the upper portion shows a region of the deformation map (deviatoric stress vs rock grain-size) that corresponds to the material response that involves a plastic yield stress. This type of deformation may occur at relatively low temperature and high stress. In this regime, on a microscopic level, dislocation glide may dominate, a mechanism generally known as Peierls mechanism. This mechanism may be important to deep lithospheric shear zones (Kameyama

et al., 1999). Such rheology has not been accounted for in GIA models and we do not treat this rheology in this Chapter.

Constraints provided by seismology can be linked to temperature and pressure-dependent creep laws for mantle rock aggregates composed of typical mantle minerals (olivine, pyroxene, Al-silicate). A modicum of understanding of the physics involved in both elastic wave propagation *and* dislocation and impurity diffusion within the rock grain interior and at grain boundaries is required. These will be briefly reviewed in this paper, along with some of the caveats that accompany these linkages. Furthermore, we assemble the current state-of-the-art interconnections among the high pressure and temperature thermodynamics and solid state relations that allow us to quantify the effective mantle viscosity.

2.2 Steady-State vs Transient Laboratory Experiments

The experimental setups for steady-state and transient creep are described by Karato (2010), Paterson and Olgaard (2000) and Kohlstedt and Hansen (2015). Two fundamental quantities must be extracted from such experiments for our application. These are the activation enthalpy for steady-state and transient, or anelastic, creep, H^* , and H_D^* , respectively. The latter activation parameter was introduced into the interpretation of seismic tomography by Karato and Spetzler (1990) and Karato (1993). There are two types of high pressure and temperature mechanical strength laboratory experiments. Mantle flow models typically use experimental results that report 'steady-state' creep laws from static microstrain devices (e.g., Karato, 2010; Kohlstedt & Hansen, 2015), while models of seismic attenuation employ forced-oscillation devices over a range of oscillation frequencies (e.g., Berckhemer et al., 1982; Jackson, 2019). Attaining a true steady state in the static experiments, wherein the rate of creation and destruction of microscopic elements at grain boundaries and within grains reaches equilibrium, is one of the challenges for developing creep laws that are acceptable in modeling mantle flow. As a rock deformation experiment begins, those microscopic elements that are capable of being mobilized under an imposed shear stress move relatively quickly. After a time, these elements (e.g., gliding or climbing dislocations, grain boundary slip, etc.) may become blocked by obstacles, including their own bending or tangling, and as a consequence, the creep rate of the rock aggregate slows. Technically, the macroscopic phenomenon is referred to as strain hardening (e.g., Peltier et al., 1980) and formal connections may be made between the damping of seismic waves to the microscopic viscoelastic strain (e.g., Minster & Anderson, 1980; Jackson, 2019). The mechanisms controlling the transition from transient to steady-state creep are numerous (e.g., Hanson & Spetzler, 1994). While complex, these are linked to the anelastic properties of mantle rocks (e.g., Faul & Jackson, 2015; Masuti et al., 2019; Jackson, 2019).

2.3 Some General Geophysical Observations

Although our understanding of the physics of creep at upper and lower mantle conditions is limited, there is a clear observational connection between regions of low seismic wave velocity and rapid isostatic response measured by geodetic uplift and/or rapid post-glacial land emergence (e.g., Sigmundsson, 1991). While accounting for lateral heterogeneity in mantle deformation has been addressed over many decades (Wu, 1999), today both higher resolution seismic tomography *and* more dense and accurate geodetic networks are reporting data, meaning that the study of lateral heterogeneity in mantle rheology is evolving into a new frontier in solid Earth sciences (e.g., Austermann et al., 2013; Lau et al., 2018; Huang et al., 2019). Estimates of viscosity based on seismic wave speeds and high-temperature creep

experiments can be tested using geodetic data that are capable of constraining GIA or post-seismic modeled crustal motions. This enhances our knowledge of regional mantle rheological structure, and produces more confident viscosity estimates than in continental areas that lack such geodetic data constraints.

2.4 Scaling S-Wave Velocity to Viscosity: Retrospective for GIA

The general study of GIA has a substantial impact on how we interpret the rheology of the Earth's mantle and lithosphere over millennial to million year time scales. The preponderance of the GIA models that are used to simulate gravitational viscoelastic flow over the ice ages assume a radially stratified mantle that is approximated as a 3-D linear Maxwell viscoelastic material in tensor form (e.g., Peltier et al., 1981). In this model rheological framework the Earth responds viscously and elastically over long and short time scales, respectively. Its success in giving rational explanation to both geodetic (e.g., Milne et al., 2004) and RSL data (e.g., Lambeck et al., 2014) has meant that extensions to Maxwellian setups that contain nonlinear power law viscosity (e.g., Gasperini et al., 2004) generally fall outside of the GIA model paradigm most commonly used in cryospheric sciences, by geodesists and in the paleo-oceanography community (e.g., Wahr et al., 2000; Dobslaw et al., 2020; Whitehouse, 2018).

The structural roots of modeling GIA with laterally varying Earth structure (GIA-LV) have a number of commonalities. Seismic tomography provides elastic wave velocity in 3-D space (r, θ, ϕ) , where the three spatial variables are radial position, co-latitude and longitude, respectively. A systematic way to describe this data is in the form $\delta v_s(r, \theta, \phi) / v_{s_0}(r)$ where the numerator of this expression, δv_s , represents the deviation of velocity from a mean value, v_{s_0} , that depends only the radial position. Both v_{s_0} and δv_s are related to absolute temperature. The temperature-dependence of the elastic constants governing wave propagation are known through theoretical and semiempirical methods (e.g., Kumazawa & Anderson, 1969). All of the GIA-LV models developed to date, including those that incorporate nonlinear power law viscosity, have assumed that the deviations from the mean are caused by a temperature deviation $\delta T(r, \theta, \phi)$ away from a radially dependent mean $T_0(r)$. Paulson et al. (2005), for example, assumed that the deviations in δv_s were linearly related to lateral density anomalies $\delta \rho$, such that

$$dlnv_s(r, \theta, \phi) = 3.33 dln\rho(r, \theta, \phi), \quad (1)$$

where here we use the logarithmic notation for the ratio of lateral deviation to the mean (see Karato (2008), p. 372). The factor 3.33 is one that may be deduced from high-temperature and pressure mineral physics (e.g., O. L. Anderson, 1995; Stixrude & Lithgow-Bertelloni, 2010; Stixrude & Jeanloz, 2015). (We elaborate on the physical relations for this factor later in this Chapter.) Paulson et al. (2005) also assumed that the relationship of seismic velocity to temperature is completed by additionally assuming that Equation (1) is divided by the thermal expansivity, α_{th} , thus deriving the spatial dependence of the thermal deviation $\delta T(r, \theta, \phi)$ from the mean $T_0(r)$. The reader may note that this is the method adopted by A et al. (2013) for GIA-LV predictions for Antarctica. Both a nominal radial

average temperature and its aspherical deviation, were assumed to be known, and written in the form

$$T(r, \theta, \phi) = T_0(r) + \delta T(r, \theta, \phi), \quad (2)$$

and entered the viscosity relationship as

$$\eta(r, \theta, \phi) = A_0 \exp\left[g T_m(r) / (T_0(r) + \delta T(r, \theta, \phi))\right], \quad (3)$$

where there is a prefactor A_0 , a dimensionless activation energy, g , and $T_m(r)$ is the melting temperature (e.g., Poirier, 2000). Thus, all of the ingredients for performing finite element model (FEM) solutions of the time-dependent sixth-order partial differential equation system for GIA-LV are defined.

Latychev et al. (2005) also developed a numerical finite volume method for GIA-LV that also used Equations (1) and (2), but made no assumption about the details of the governing rheology other than the Arrhenius-dependency given by the temperature in the exponential term. Therein, a viscosity ratio is defined

$$\Delta\eta \equiv \eta(r, \theta, \phi) / \eta_0(r) = \exp[-\varepsilon \delta T(r, \theta, \phi)], \quad (4)$$

where the parameter ε is used to adjust the total lateral variability in viscosity assumed in any GIA-LV computer simulation. A typical value for this adjustment parameter is $\varepsilon \approx 0.04^\circ K^{-1}$ (e.g., Austermann et al., 2013). Like Paulson et al. (2005), Latychev et al. (2005) assumed

$$\delta T(r, \theta, \phi) = -\frac{1}{\alpha_{th}} d \ln \rho(r, \theta, \phi). \quad (5)$$

Latychev et al. (2005) and Paulson et al. (2005) developed simple and flexible scaling relations, but which are not closely tied to rheological laws that are currently in debate in the experimental rock deformation community (e.g., Kohlstedt & Hansen, 2015). In contrast, the FEM formulation for GIA-LV by Wu (2005) sought to expand the scaling method so that it explicitly accounted for activation enthalpy of high temperature creep, its decomposition into activation energy, activation volume, along with the pressure dependence. This was accomplished by adopting the formulation of Ivins and Sammis (1995). The latter method also forced the globally averaged radially-dependent viscosity, $\eta_0(r)$, to be defined by the same rheological dependencies. This guarantees an internal self-consistency, such that the rheological parameters could be tested against the most robust among competing 1-D GIA inversions for mantle viscosity. The formulation proposed by Ivins and Sammis (1995) used the same assumptions for the relationship of elastic shear wave velocity to density and temperature as in Equations (1), (2) and (5), though it more rigorously accounted for the

Grüneisen parameter, a fundamental property of theoretical thermal elasticity (e.g., Isaak et al., 1992; Stacey & Hodgkinson, 2019). These relationships will be explicitly given in Sections Methods for Approach 1 and Methods for Approach 2 in this Chapter.

Wu (2005) adopted the \log_{10} representation of the viscosity field and employed the relationship to the activation enthalpy parameter, H^* , as proposed by Ivins and Sammis (1995). This representation can be written as the ratio

$$\Delta\eta = \frac{\exp[a/(T_0 + \delta T)]}{\exp[a/T_0]}, \quad (6)$$

with $a \equiv H^*/R_G$ and R_G being the Universal Gas Constant. Upon taking \log_{10} of both sides of Equation (6) this becomes

$$\frac{\log_{10}\Delta\eta}{\log_{10}e} = \frac{a\delta T}{(T_0 + \delta T)}, \quad (7)$$

clearly a nonlinear relationship between viscosity and lateral thermal anomaly. Ivins and Sammis (1995) further demonstrated with several global shear wave seismic tomographic models that it was feasible to linearize this relationship by using a Taylor expansion about $\delta T = 0$:

$$\frac{\log_{10}\Delta\eta}{a\log_{10}e} \approx -\frac{\delta T}{T_0^2} + \text{higher order terms.} \quad (8)$$

By truncating the expansion at a single term, we arrive at the form employed in Wu (2005) and to be used in our inter-comparison of methods. The approximation is also inherent to the strategy of Latychev et al. (2005). In the Appendix to this Chapter we use variability up to the maximum temperature differences found in the Antarctic thermal model of An et al. (2015) at a depth of 240 km, to give a quantitative evaluation of this approximation. Although Wu (2005) used this form, a later GIA-LV model (H. Wang et al., 2008) extended the relation for connecting $\delta\nu_s$ and δT to include anelastic corrections that were earlier advocated by Karato (1993). It is this anelastically corrected form that is the starting point of our inter-comparative study entertained later in this Chapter.

3 Microphysics

It has long been understood that deformation mechanisms in ceramic materials at high temperature are controlled by the diffusion of ionic impurities (point defects) or by slip due to dislocations (linear or planar defects) in the crystal lattice. Ceramic materials are distinguished by their covalent and ionic atomic bonding, usually involving one or more oxygen atoms. This intra-crystalline bonding allows experiments to be performed on certain analogue materials having crystal structure like the rock materials at mantle temperatures and

pressures, thus relevant to both thermal elasticity and creep. This section discusses the main mechanisms, as well as a generalized flow law and the main rationale used to approximate an 'effective' viscosity.

3.1 Steady-State Flow Law and Temperature-dependent Anelasticity

The diffusion of point defects and the slip of dislocations are the microscopic manifestations of diffusion and dislocation creep, respectively. Both creep mechanisms are controlled at some stage by diffusion, and hence by temperature. The strain rate, $\dot{\epsilon}$, in the presence of a background stress, σ , is then exponentially dependent on the local mantle, T , typical of all thermal activation processes (e.g., Kittel, 2004; Cressler & Moen, 2012). The form is

$$\dot{\epsilon} = \tilde{f}(\dot{\epsilon}_0) \sigma^n \exp(-H^*/R_G T). \quad (9)$$

where H^* is the activation enthalpy associated with diffusivity in solids (Poirier, 2000; Karato, 2008), R_G the Universal Gas Constant (8.314×10^{-3} kJ/mol K), n a semi-empirical exponent ($1 \leq n \leq 5$) and $\tilde{f}(\dot{\epsilon}_0)$ a constant coefficient having units of $\text{sec}^{-1} \text{Pa}^{-n}$ which is often tagged to a reference strain-rate $\dot{\epsilon}_0$, or by other specific features of the microphysics operating. The temperature-dependence derives from the Maxwell-Boltzmann statistics governing the ionic-molecular interactions at the crystalline level, hence Equation (9) must have the temperature expressed in Kelvin (e.g., Kittel, 2004). In laboratory settings high confining pressures are required to stabilize the sample while reaching measurable strain rates. A tractable parameter to solve for is H^* at a series of temperature values. In this Chapter we shall make use of two activation enthalpies, one for steady-state creep and the other for anelastic and transient (viscoelastic) strain processes in mantle rock. These activation enthalpies are decomposed into two terms:

$$H^* = E^* + PV^*, \quad (10)$$

and

$$H_D^* = E_D^* + PV_D^*, \quad (11)$$

where P is pressure and pairs E^* , E_D^* and V^* , V_D^* are the activation energies and volume, for the steady-state and transient creep states, respectively. Each activation parameter will be unique to the different creep mechanisms that operate within a crystalline rock structure, either within or at the boundaries of the rock grains. Generally, E^* is more straightforward to recover from laboratory experiments than are values of V^* , and similarly for their transient counterparts, E_D^* and V_D^* . While the former may be recovered at relatively lower confining pressures, experiments determining V^* must accommodate stepwise increases in pressure while carefully accounting for all other factors influencing creep mobility (Dixon & Durham, 2018).

It is to be understood that these activation parameters are arguments in exponential functions multiplying T^{-1} . Hence, they represent the fact that there is a strong temperature-dependence to both steady-state creep and to seismic dissipation and dispersion (e.g. Wiens et al., 2008). The latter viscoelastic properties are essential for properly developing transfer functions between S-wave velocity and mantle viscosity.

The normal procedure for determining E_D^* from experimental results is to fix V_D^* to roughly the values determined by steady-state creep experiments ($V_D^* \sim V^* \approx 15 \pm 5 \times 10^{-6} \text{ m}^3 \text{ mol}^{-1}$) (e.g., Jackson & Faul, 2010; Dixon & Durham, 2018). For estimating the temperature-dependent anelastic influence on shear wave velocity, we will assume pairs E_D^*, V_D^* , corresponding to the experimental results of Jackson and Faul (2010).

If the constitutive laws only involved these two thermodynamic variables, while likely non-unique, the problem of mapping seismic velocity to viscosity using the methods of either Ivins and Sammis (1995) or H. Wang et al. (2008) is quite tractable, provided that both the temperature and the rate-controlling creep mechanism are decipherable. However, not only is it difficult to decipher the rate-controlling mechanism, but the pre-exponential constant $\tilde{f}(\dot{\epsilon}_0)$ is dependent on both grain-size and volatile impurities, such as water, or free ions of hydrogen and oxygen. While current controversy exists over the realistic magnitude of the effect of volatile impurities, it may be treated in a formal way by including an additional pre-exponential term: $f_{H_2O}^{\bar{r}}(P, T)$, where f is the fugacity of the respective impurity in the rock material (Karato, 2008). It also represents the partial pressure of the invasive atomic species in the crystal structure. (Here \bar{r} is an experimentally determined exponent). The larger these impurity effects are, the more intractable becomes building a relation between seismic imaging in the mantle and lateral variations in effective viscosity, since impurities in the mantle may have spatial dependencies that do not follow, or even mimic, those of the spatial dependencies of $T(r, \theta, \phi)$. Therefore, they are briefly discussed in the following section.

3.2 Role of Water and Grain-size

Small grain sizes tend to promote material transport by grain boundary diffusion (Karato & Wu, 1993), whereas large grain-size promotes deformation by dislocation creep. Also, experiments with mantle olivine and synthetic anorthosite indicate that trace amounts of structurally bound water have a pronounced weakening effect (Mackwell et al., 1985; Hirth & Kohlstedt, 1996; Mei & Kohlstedt, 2000; Dimanov et al., 1999), thus indicating the importance of water-weakening in increasing the mobility of rock in the lithosphere and upper mantle environment. A wet sample of rock is defined when there are roughly 500 - 3000 H per 10^6 Si and a dry sample at one order of magnitude smaller fraction H content. (1 ppm H/Si $\approx 10^{-5}$ wt % of water in olivine, or 5×10^{-3} to 3×10^{-2} wt % H_2O). Proper quantification of the effect of water-weakening at mantle temperatures and pressures remains controversial (Fei et al., 2013). Generally, volatile impurities, such as water, are a subclass of point defects. Other atomic or molecular species may also be important in controlling mobility.

In order to account for grain-size in the constitutive equations, $\tilde{f}(\dot{\epsilon}_0)$ is set equal to Ad^{-p} (Karato et al., 1986; Dimanov et al., 1999), and for both grain-size and wetness content to

$Ad^{-p}f_{\text{H}_2\text{O}}^q$, where the units and interpretation of the constant A , are dependent on the inclusion, or exclusion, of the effects. Here p and q are experimentally determined exponents. Possibly the most complete prefactor would be to set

$$\tilde{f}(\dot{\epsilon}_0) = Ad^{-p}f_{\text{H}_2\text{O}}^q \exp(\bar{\alpha}\bar{\phi}), \quad (12)$$

which would additionally account for the influence of the fraction of partial melt content, $\bar{\phi}$, ($\bar{\alpha}$ being a constant) on solid deformation (Hirth & Kohlstedt, 2004). One of our approaches uses the prefactor in the form of Equation (12). Lateral heterogeneity in grain-size (Dannberg et al., 2017) and water content (O'Donnell et al., 2017) might be important for Antarctica. Examining these latter causes is warranted should we discover especially poor resemblance of effective viscosity scaled to shear wave velocity maps, $v_s(r, \theta, \phi)$.

It is worth noting that both structurally bound water and grain-size likely affect seismic velocities, although quantitative relationships are uncertain, and thus difficult to implement formally in viscosity estimates. Water is proposed to reduce seismic velocities by increasing anelasticity, through a similar mechanism to its effect on viscosity (Karato, 2003). Recent laboratory experiments indicate a small direct seismic velocity perturbation due to the presence of water (Cline II et al., 2018), yet a substantial sensitivity to oxygen fugacity, f_{O_2} , a property that often positively correlates with water content. Rock mechanics experiments do show a significant dependence of anelasticity on grain-size at upper mantle temperatures, suggesting that small grain-size can lower seismic velocity (Jackson & Faul, 2010). The effect of water and small grain-size both reduce seismic velocity and mantle viscosity. Thus, they both qualitatively simulate the effects of higher temperatures and both act to reduce mechanical strength. Ignoring the effects of water and grain-size in converting seismic velocities to viscosity will at least lead to viscosity anomalies of the correct sign, if not the correct magnitude.

3.3 Deformation Mechanisms in Mantle Conditions

Simulation of upper mantle conditions in the laboratory are limited by confining pressure, limited temperature ranges and relatively high strain-rates that must be studied in the laboratory. None-the-less, there are advantages in that experiments have been performed on natural or synthetic rocks of either the major constituents of the mantle or their analogues. Sampling of upper mantle rocks under a microprobe reveal those sub-grain scale dislocation sites that are associated with ceramic high-temperature creep mobility. If diffusion creep dominates deformation in the upper mantle, $n \approx 1$ in Equation (9), an assumption often employed in GIA models. However, this requires the upper mantle to have small grain sizes throughout, contrary to observations (Karato & Wu, 1993; Dannberg et al., 2017; Coltorti et al., this volume). For large grain-size, or large stress, dislocation creep dominates as in Figures 2 and 3. An alternative mechanism, which has been studied extensively over the past several years is grain boundary sliding (GBS)(Hirth & Kohlstedt, 2004; L. Hansen et al., 2011). While this mechanism may be controlled by diffusion for small grain-size, experiments with naturally occurring olivine reveal that dislocation accommodated GBS can dominate creep with $n \approx 2.9$ at upper mantle conditions and realistic grain-size ($d \sim 1 - 10$ mm). Figure 3 shows the dominant deformation mechanisms in a stress, temperature diagram

for cases of small (0.01 mm) and large (1 mm) grain sizes. As an example, consider the contour line corresponding to a strain rate of 10^{-15} s^{-1} for an olivine with a 1 mm grain-size. At high temperature and low stress, diffusion creep will dominate. With increased stress, dislocation creep will become more important. The stress at which the transition occurs will be higher when grain-size is decreased. For very small grain-sizes ($\sim 10\mu\text{m}$), diffusion creep will give way to GBS, when stress is increased.

4 Continuum approach and effective viscosity

In the continuum point of view taken in geodynamic flow simulations, material behavior can be well described by the Maxwell model (e.g., Ivins et al., 1982; Karato, 2008). In the Maxwell model elastic deformation occurs instantaneously, while at relatively long timescales movement ($\geq 1-10$ thousand years) is described by slow flow in a viscous fluid. GIA codes bookkeep the elastic deformation, as this is important for RSL and Little Ice Age geodetic computation (Ivins et al., 2000; Sabadini et al., 2016), but they are usually ignored in geodynamic models wherein the total viscous strain vastly exceeds that of the elastic components over tens of millions of years, or greater. The Maxwell model is generally faithful to the microphysical processes; it corresponds to a situation in which defects can move indefinitely after an initial elastic strain (Karato & Spetzler, 1990; Karato, 2010). To use the Maxwell model, a viscosity parameter is needed. The viscosity in such models can be linked to both the laboratory-based laws and to seismically based mantle models by defining a so-called effective viscosity.

4.1 Choice of Effective Viscosity Relation

The advantage of defining an effective viscosity, $\bar{\eta}$, is that it can be conveniently linked to the laboratory-based laws, to seismically based mantle models (Doubrovine et al., 2012) and to the boundary value problems typically employed in the GIA problem (Spada et al., 2011). Three different forms that have been proposed by Poirier (2000) and Ranalli (2001). Each, however, require some flow variable to be fixed. The three relationships yielding an effective viscosity are given below. At constant local background strain rate

$$\bar{\eta} = \eta_\epsilon = \frac{1}{2} \tilde{f}_\epsilon \dot{\epsilon}^{(1-n)/n} \exp(H^*/nR_G T), \quad (13)$$

while at constant background stress

$$\bar{\eta} = \eta_\sigma = \frac{1}{2} \tilde{f}_\sigma \sigma^{(1-n)} \exp(H^*/R_G T). \quad (14)$$

Finally, at constant rate of energy dissipated in the flow

$$\bar{\eta} = \eta_\Phi = \frac{1}{2} \tilde{f}_\Phi \Phi^{(1-n)/(1+n)} \exp[2H^*/(n+1)R_G T], \quad (15)$$

where $\Phi = \dot{\epsilon}\sigma$ and the constant factors \tilde{f}_ϵ , \tilde{f}_σ and \tilde{f}_ϕ are functions of the experimental fits involving water or oxygen fugacity, grain-size, partial melt and the power law exponent n (for example, see Equation 12). The reader may consult Ranalli (2001) or Karato (2008) (eqs. 19.3a-c) for the corresponding details. The Maxwell assumption so often used in GIA modelling is that either $n=1$ or that one of the above relations offers a link to laboratory data. We have already mentioned that it is possible to formulate Maxwellian models with $n>1$. Should the laboratory experiments be well fit with $n=1$ (diffusion creep), then the classic Newtonian viscosity, η , defined with the equation

$$\eta \equiv \frac{\sigma}{2\dot{\epsilon}_0} \quad (16)$$

applies, and there are no ambiguities. Models using any approximations represented by Equations (13) through (15) (e.g., Ivins, 1989; Zhu, 2014) are not as tightly linked to the laboratory experiments as are mantle flow modeling that directly incorporate Equation (9), and perhaps (12), into the computations (e.g., Wu, 2002; Dal Forno et al., 2005).

Since the time of Norman Haskell's work in the 1930's, the simple Newtonian viscosity, η , is the parameter sought for the mantle interior in various forward-inverse GIA and mantle flow models. In what follows in this Chapter we will be using the effective viscosity as defined by Equation (14). This will avoid employing the power-law exponent n for dislocation creep into the argument of the exponential in the flow law. We remark that in doing so, we choose that approximation which will tend to maximize the lateral variability predicted from the ANT-20 seismic tomography model.

4.2 Maxwell Models: Why are they Relatively Successful?

Considering that most laboratory experiments yield $n \sim 3$, it might come as a surprise that the Newtonian assumption, when inserted into the Maxwell constitutive relation, does fairly well at numerically simulating mantle geoid and GIA. There can be many reasons for this that are beyond the scope of our discussion. Limitations of the data sets for constraining geodynamic models is just one obvious source. Two popular ideas are proposed as logical explanations. First, is that the flow law actually is Newtonian, a prediction shown in the two deformation diagrams of Figure 3 labeled diffusion creep. Second, is a suggestion offered by Karato and Wu (1993) that mantle flow is self-regulating, via modifications of grain-size. Here, the idea is that stress increases during the rise of ice loading/unloading phases with the consequence that grain-size is reduced. Such reduction moves the local mantle creep state to the left in the deformation diagram of Figure 3, closer to the boundary between diffusional ($n=1$) and dislocation ($n \sim 3$) dominant mechanisms. This might allow the operative microscopic plasticity to hover quite close to the boundaries between competing solid state creep mechanisms (see the solid lines in Figure 3 that separate diffusion, dislocation and grain boundary sliding regimes).

5 Viscosity Estimates for Antarctica

As is clear from the previous section, viscosity involves many parameters that are themselves uncertain. Past studies of laterally varying viscosity beneath Antarctica (e.g.,

Kaufmann et al., 2005; A et al., 2013; van der Wal et al., 2015; Gomez et al., 2018) have all agreed on a larger East Antarctic viscosity, owing to the faster seismic velocities imaged there. The results of these studies, however, substantially differ in the predicted magnitudes. Although, the resolution of the mantle seismic structure has improved through the years, much of the differences may be caused by methods employed in transforming seismic velocity to viscosity.

In the several sections which follow we estimate Antarctic viscosity in three different ways. In the first approach viscosity perturbations are calculated directly from seismic models according to the approach of Wu et al. (2013). These use the temperature derivatives of shear velocity from Karato (2008) to estimate a temperature anomaly and to estimate viscosity anomaly relative to a reference viscosity model. The second method uses the structural form derived by Ivins and Sammis (1995), but is extended to capture the anelastic correction using the theoretical development of Karato and Karki (2001) and Karato (2008). The third method has similarities to the first two approaches, but assumes a complete representation of the rock experimental results, including the non-thermodynamic prefactors. Both the 1st and 3rd approaches will rely on temperature derivatives as explicitly computed by Karato (2008). In all approaches we assume that global average 1-D seismic velocity and mantle temperature are models that are relatively well known. In addition, Approaches 1 and 2 assume that radial 1-D viscosity models, $\eta_0(r)$, for the upper mantle are well determined. They then compute a 3-D viscosity model based on perturbations to these global averages based on a straightforward conversion from seismic velocity to effective viscosity. Naturally, in each case of Approach 1 and 2, $\eta_0(r)$ must also be logically linked to the flow law assumed. To give clarity to the formulations of the 3 methods, we give some of the requisite fundamentals of the classical thermodynamics and elasticity theory. To better elucidate the comparison and the uncertainties, the three methods all start from the same seismic structure model of Lloyd et al. (2020) (Wiens et al., this volume) termed ANT-20, which is the highest resolution continental scale model available. Figure 4 shows the ANT-20 $\delta ln v_s(r, \theta, \phi)$ field at depths of 150 and 550 km. Together with the map of Figure 1, these show the lateral variations in shear wave velocity common to all three Approaches for estimating effective viscosity that will be discussed in the next 4 Sections of this Chapter.

5.1 Relations Among Elastic and Seismic Parameters

Seismic velocity in isotropic rock media is related to density, ρ , elastic bulk and shear moduli, κ, μ , respectively, by

$$v_s = \left[\frac{\mu}{\rho} \right]^{1/2}, \quad (17)$$

$$v_p = \left[\frac{\kappa + \frac{4}{3}\mu}{\rho} \right]^{1/2}. \quad (18)$$

Thus, both shear (S) and compressional (P) seismic velocities are related to density. It is often useful to consider seismic velocities as anomalies relative to a 1D radial background (reference) model. For example, the change in shear velocity, δv_s ($v_s - v_{S_0}$), relative to the background model, v_{S_0} , is expressed as the ratio, $\frac{\delta v_s}{v_{S_0}}$, for such anomalies. This quantity is accurately approximated using the natural logarithm and doing so is advantageous for our purposes.

$$\delta \ln v_s \approx \frac{\delta v_s(r, \phi, \theta)}{v_{S_0}(r)}, \quad (19)$$

and

$$\delta \ln v_p \approx \frac{\delta v_p(r, \phi, \theta)}{v_{P_0}(r)}. \quad (20)$$

In the following we focus on the shear wave velocities, as shear velocity models generally show the highest continent-wide resolution in the Antarctic upper mantle. D. L. Anderson (1987) derived relations from thermodynamic and solid state physics principles that interrelate seismic velocity anomalies and density anomalies. One goal of linking global seismic mapping and geodynamical modeling is to constrain the ratio of variable seismic velocity to variable density, $\delta \ln v_s / \delta \ln \rho$ (e.g., Dziewonski et al., 1993). In theory, inversion of such ratios can be linked to thermodynamic quantities derived from pressure and temperature derivatives of elastic parameters of mantle mineralogy. For interpreting seismic velocity anomalies and converting them to viscosity, a fundamental interrelation used by Ivins and Sammis (1995) was:

$$\frac{d \ln v_s}{d \ln \rho} = \frac{1}{2} \left[\frac{\partial \ln \mu}{\partial \ln \rho} - 1 \right]. \quad (21)$$

The ratio appearing on the right hand side of Equation (21) is the Grüneisen parameter for the shear modulus, c_1 :

$$c_1 \equiv \frac{\partial \ln \mu}{\partial \ln \rho}. \quad (22)$$

c_1 is identical to δ_μ as defined in the monograph by Karato (2008) (see equation 4.35b). The thermal Grüneisen parameter is defined as a ratio of vibrational frequencies to molecular volume, γ_μ ,

$$c_1 = 2\gamma_\mu + \frac{1}{3}. \quad (23)$$

The relations we have presented in this short section establish the basic theory for relating seismic wave velocity to the Grüneisen parameter, a fundamental property of the thermodynamic state of crystalline rock at high temperatures and pressures. In the next section we show how this is a key link to temperature derivatives of the shear wave velocity. Here we strictly employ the thermodynamic and elasticity approach that is advocated by D. L. Anderson (1988); O. L. Anderson and Isaak (1995); Karato (2008); Stixrude and Jeanloz (2015); Stacey and Hodgkinson (2019) and others. We must also be cognizant of the uncertainties associated with the thermal elastic constants of mineral physics at high temperatures and pressures of the mantle. For the reader unfamiliar with thermal and seismic equations of state, but who wants to delve further into this subject for its practical ramifications (e.g., Núñez-Valdez et al., 2013), understanding the interrelationship between elastic constants and thermodynamic variables is quite important.

5.2 Thermal Parameters

A key element of any geodynamical model is the thermally induced buoyancy. For our purposes, one element of this buoyancy, the thermal expansivity $\alpha_{th} \equiv -\partial \ln \rho / \partial T$ is a simple elastic parameter that can be derived by mineral physics (e.g., O. L. Anderson et al., 1992; Katsura et al., 2010) and it expresses the volume changes that occur due to heat content. The radial dependency of α_{th} can be adopted, for example, from O. L. Anderson et al. (1992) for the upper mantle and from Chopelas and Boehler (1992) for the lower mantle. Here we select the depth-dependence derived by Katsura et al. (2010). Our goal is to isolate anomalous heat content through its influence on shear wave speed. Thus, the essential parameters are the thermal expansivity α_{th} and c_1 or γ_μ . These parameters were the essence of the Ivins and Sammis (1995) method and implicitly enter in all of the approaches in this Chapter.

To describe anomalous heat content it is important to have a three-dimensional description of the temperature distribution in the mantle. We define anomalous temperature as $\delta T(r, \theta, \phi)$, that part of the temperature that deviates from the globally based spherically symmetric part. Stated formally: $\delta T(r, \theta, \phi) \equiv T - T_0(r)$ wherein $T_0(r)$, is the global spherically averaged temperature at radius, r . This decomposition is standard procedure in computing free convection in planetary interiors (e.g., Durney, 1968). To infer effective viscosity, all approaches require, implicitly or explicitly, a reference temperature profile in order to specify a radial variation of viscosity and a distinct laterally varying viscosity. Under the approximations developed in Ivins and Sammis (1995) these viscosity and temperature fields may be expanded in orthogonal functions. Hence, the relations for the viscosity and seismic velocity fields can both be expanded in spherical harmonics and interrelated in the spectral domain. We do not, however, give the details of this procedure in this Chapter. Table 2 gives the $T_0(r)$ values used for all three approaches where we also show non-global averages at 150 km depth.

The elastic parameters can be combined to form the desired derivative that relates seismic velocity anomalies to temperature anomalies:

$$\frac{\partial \ln v_s^{(ah)}}{\partial T} = -\frac{1}{2} \alpha_{th} (c_1 - 1). \quad (24)$$

where superscript *ah* denotes anharmonic, meaning that the elastic lateral variation in velocity results from thermal expansion and associated changes in elastic structure. (See equation 4.40a of Karato (2008).)

What follows is a discussion of the three approaches to deriving lateral viscosity variations from a seismic model. This requires an estimate of the global average temperature, T_0 , at each depth. Three depths are chosen for the inter-comparison: $z = 150, 300$ and 550 km. Because the reference seismic and viscosity models are global, it is essential that the reference temperatures represent global averages. The 150 km depth lies within the conducting lithosphere for some locations. Thus for T_0 at 150 km, we use the global average estimate of 1473 ± 40 °K from Stacey and Davis (2008). Should non-global T_0 values for relatively hot or cold subcontinental mantle be assumed (see Table 2), they will seriously bias the predictions of deviations from a purely radially dependent viscosity. We employ estimates of the isentropic, convecting, variation with depth for our value of T_0 for the deeper depths, arriving at 1722 ± 42 °K for 300 km and 1930 ± 50 °K for 550 km depth (see the fig. 3 and 4 presented in Katsura et al. (2010)). Karato and Karki (2001) pointed out the potential pitfalls of deriving seismic constraints on either mantle temperature and/or driving buoyancy in geodynamic models without a priori correction for anelasticity. We return to this issue in the section discussing Approach 2.

5.3 Road Map for the Three Approaches

Karato and Spetzler (1990) and Karato (1993) demonstrated that all realistic mantle rock mineral assemblages will have elastic wave velocities diminished by thermally activated defect processes, so-called anelastic dispersion (e.g., Jackson et al., 2002). This must be accounted for in seismic studies, and the three approaches generally do so in different ways. Some elements of the approaches are summarized in Tables 1 and 3. Approach 1 uses a method which was partly described in the maps of the lateral variation in mantle viscosity derived using a combination of the scaling described by Ivins and Sammis (1995) with the modifications described by Wu et al. (2013). As a consequence, a number of features of Approach 1 and Approach 2 are similar, and we shall attempt not to be redundant in describing these overlapping features. Each method does apply an anelastic correction, as first suggested by Karato (1993). The latter is a necessary feature of deriving variable temperature from seismic tomography. However, the detailed application of this correction differs among approaches. For Approach 1 and 3, the anelastic correction simply follows from the table recommended by Karato (2008) (Table 20.2, page 376). For Approach 2 we assemble the components of the anelastic correction from the general relationships for diffusion-controlled energy loss as described by Karato and Karki (2001) and in the monograph of Karato (2008) (equations 18.5, 18.6, 20.12 and 20.13, therein). We also rederived the asymptotic relationships of Karato (2008) (equations 20.15b and discussion). This revealed that the asymptotics come with the added caveat that the frequency-dependent power-law exponent (α) must be restricted to $\alpha \leq 0.3$. Without the asymptotics, the root of the anelastic theory and its temperature dependence is essentially identical to that employed by Guerri et al. (2016).

For our inter-comparison exercise we generally assume rather different flow laws to be operative. Approach 1 assumes diffusion creep as described and quantified by Hirth and Kohlstedt (2004) and Approach 2 assumes GBS dislocation creep as described and quantified by L. Hansen et al. (2011). Readers that may be interested in the derivation that leads to the linear relations between $dlnv_s$ and δT and the viscosity variability that we describe below, $\log_{10} \Delta\eta(r, \phi, \theta)$ may wish to consult the paper by Ivins and Sammis (1995) and the Appendix to this Chapter.

Approach 3 is unique in that it uses flow laws in a composite form, combining olivine dislocation, diffusion and GBS micromechanics for calculations at 150 and 300 km depth, and similarly for ringwoodite at 550 km for dislocation and diffusion. Other differences that distinguish Approach 3 are summarized in Tables 1 and 3. Approach 3 uses thermoelastic plus anelastic scaling to δlnv_s that is identical to Approach 1.

5.4 Inference from Modeling Geodetic Data

The construction of trends from time series of geodetic observations of the movement of the crust for the past 3 decades (e.g., Dietrich et al., 2004; Bevis et al., 2009) provides essential information for the Antarctic GIA modeling community. Inferences of mantle viscosity beneath Antarctica from geodetic observations are useful for fine tuning, and even calibrating, the parameters used in mapping seismic velocity to viscosity. Unfortunately these estimates generally require some assumption about ice load history, which is not well understood, and thus different estimates for the same region can vary significantly. Nield et al. (2014) use GPS-measured uplift following the 2002 breakup of Larsen B Ice Shelf to constrain the upper mantle viscosity beneath the Northern Antarctic Peninsula to about 1×10^{18} Pa s or less. A more recent GIA analysis by Samrat et al. (2020) also favors a quite low shallow mantle viscosity in this region ($0.3\text{--}3 \times 10^{18}$ Pa s) and a modest upper mantle viscosity of 4×10^{20} Pa s deeper than 400 km depth. For the northern Antarctic Peninsula, Ivins et al. (2011) used a different GPS data set and Gravity Recovery and Climate Experiment (GRACE) data. The modeled GIA uplift also included an ice model with historical retreat (~100 - 150 years) and determined a best-fit mantle viscosity of $4\text{--}7 \times 10^{19}$ Pa s. Wolstencroft et al. (2015) and Bradley et al. (2015) estimated upper mantle viscosity at $1\text{--}3 \times 10^{20}$ Pa s across the southernmost Antarctic Peninsula and western Weddell Sea based on GPS measurements and improved ice load history. Zhao et al. (2017) also modeled regional mantle viscosity in the central Peninsula and found values in excess of 2×10^{19} Pa s with an ice loss history documented back to 1966 using remote sensing data. Late Holocene beach uplift data was modeled by Simms et al. (2012) for the South Shetland Islands glacial advance and retreat and associated viscoelastic GIA response. They determined a best-fit upper mantle viscosity value of 1.0×10^{18} Pa s, applicable to the asthenospheric mantle adjacent to the actively spreading Bransfield Strait Basin (e.g., Lawver et al., 1995). In summary, estimates of upper mantle viscosity beneath the Antarctic Peninsula range from less than 10^{18} Pa s to about 3×10^{20} Pa s, with lower values generally predominating in the northern and western areas.

A few viscosity estimates are also available for other areas of West Antarctica. Nield et al. (2016) suggested, based on observed responses to the stagnation of the Kamb Ice Stream, that upper mantle viscosity beneath the Central Siple Coast cannot be less than 1×10^{20} Pa s.

Barletta et al. (2018) modeled extremely rapid GPS uplift rates in the Amundsen Sea Embayment region. After corrections for the elastic response from current ice mass loss are applied, an upper mantle viscosity that is lower than the canonical upper mantle values ($2\text{--}6 \times 10^{20}$ Pa s) can be inferred. Their best fitting model revealed a mantle viscosity of 4×10^{18} Pa s from 65–200 km depth, underlain by 1.6×10^{19} Pa s from 200–400 km depth and 2.5×10^{19} Pa s from 400–660 km. Using a shorter ice unloading history than Barletta et al. (2018), a GIA model proposed by Powell et al. (2020) that employed seismic scaling, suggests that viscosity as low as several times 10^{18} Pa s in the shallow upper mantle and several times 10^{19} Pa s down to a 900 km depth might be responsible for the rapid GPS uplift. Inevitably, these estimates of Antarctic mantle viscosity will improve as our constraints on past ice change become more robust (e.g., Nichols et al., 2019; Johnson et al., 2020).

We caution the reader that here we have discussed the ability of Maxwell Earth models, having a single parameter, $\bar{\eta}$, for steady-state viscosity per radial layer, to simulate Antarctic GPS crustal motion trend data. It is possible that more sophisticated models involving higher order viscoelasticity, of the type used to model torsion experiments, may also be appropriate to satisfying the geodetic data sets (e.g., Faul & Jackson, 2015; Lau & Holtzman, 2019; Ivins et al., 2020).

In the following three sections we describe the methods and calibration for each of the three inter-comparative approaches. Approach 2 also presents a disambiguation of the anelastic correction parameters. Here, analytical representation facilitates studying the sensitivity to all parameters. It is important to provide the reader with a concrete set of principles that the inter-comparisons obey. In Table 3 provides some additional rules that we follow. These supplement those presented in Table 1. The next three sections further detail those rules in the inter-comparison that are defined in Table 3 'free'. (The term 'imposed' means common to the three approaches.) Before we proceed, the background, or globally averaged effective viscosity at depth $\bar{\eta}_0(r)$ should be explained, as these are different for each approach. For Approach 1, $\bar{\eta}_0(r)$ takes on a constant value of 2×10^{20} Pa s, a value found for the upper mantle using the Antarctic GIA model of Ivins et al. (2013). Approach 2, tests the rheological law assumed at a depth of $z = 225$ km and compares it to the most reliable estimates that are available from the Northern Hemisphere. In Approach 2, $\bar{\eta}_0(r)$ varies with the complete rheological law. Finally, for Approach 3 the value of $\bar{\eta}_0(r)$ is neither explicitly computed or assumed, and its effective value follows from the complete composite rheology that will later be described.

6 Approach 1

6.1 Methods for Approach 1

We now pursue computation of the ratio $\Delta\eta(r, \theta, \phi) \equiv \bar{\eta}(r, \theta, \phi) / \bar{\eta}_0(r)$ as a fundamental measure of global viscosity variation. Introducing the parameters on the right-hand-side of Equation (25), Ivins and Sammis (1995) proposed the simple relationship:

$$\log_{10}\Delta\eta(r,\theta,\phi) = M \frac{2a}{\alpha_{th}T_0^2} \cdot \frac{1}{(c_1-1)} \frac{\delta v_s(r,\theta,\phi)}{v_{S_0}}, \quad (25)$$

and assumed that the observed S-wave anomaly $\delta v_s/v_{S_0} \equiv \delta \ln v_s$ could be equated to the anharmonic (*ah*) velocity change derived from mineral physics and elasticity. The relation uses $M \equiv \log_{10}e$ and $a \equiv (E^* + PV^*)/R_G$. Here we recognize the exponent from the strain rate Equation (9) or the effective viscosity η_σ as in Equation (14). Provided one recognizes the qualifications for writing Equation (14), the approximation (25) is not particularly tied to diffusional creep laws, as it is equally valid for any dislocational creep law. It is assumed that there is an r,θ,ϕ dependence will be associated with $\log_{10}\Delta\eta$ and δv_s , but only radial dependency with the other parameters. Clearly, the assumption of material homogeneity is implied in Equations (9), (14) and (12), and is also implied in the practical application of the partial derivative relations derived from the elasticity relations for a realistic Earth model.

Wu et al. (2013) introduced a formulation that adds the anharmonic contribution of Equation (24) to the contribution from anelastic dispersion:

$$[\partial \ln v_s / \partial T]_{\text{total}} \equiv \frac{\partial \ln v_s^{(ah)}}{\partial T} + \frac{\partial \ln v_s^{(an)}}{\partial T}. \quad (26)$$

This results in:

$$\log_{10}\Delta\eta(r,\phi,\theta) = -\frac{M\beta}{[\partial \ln v_s / \partial T]_{\text{total}}} \frac{a}{T_0^2} \frac{\delta v_s}{v_{S_0}}, \quad (27)$$

with β discussed below. Karato (2008) provides approximations for the two derivatives on the right-hand-side of Equation (26) with values given in his Table 20.2.

Computing viscosity using this method requires choices of global reference models for shear velocity, temperature, and viscosity. Since the ANT-20 Antarctic seismic model was developed by Lloyd et al. (2020) from the global 3D model 362ANI, which was based on the 1D model STW105 (Kustowski et al., 2008), we use STW105 as the shear velocity reference model. The temperatures are common to all three methods and are discussed in the previous section. Conductive temperature in the lithosphere is from a thermal boundary layer geotherm of Stacey and Davis (2008). The intersection of this profile and that of an adiabatic mantle occur at about 200 km where we interpolate the geotherm onto the adiabatic temperature gradient of Katsura et al. (2010).

The computation requires rheological parameters for the construction of a in Equation (25). For the activation energy, E^* , Hirth and Kohlstedt (2004) suggests a value of 375 kJ/mol for either wet or dry diffusion creep. While the activation volume, V^* , is poorly determined from experimental work, Hirth and Kohlstedt (2004) suggest it could range from $2-10 \times 10^{-6} \text{ m}^3/\text{mol}$ for dry diffusion creep and $V^* \leq 20 \times 10^{-6} \text{ m}^3/\text{mol}$ for wet diffusion

creep, so we use $5 \times 10^{-6} \text{ m}^3/\text{mol}$ in this calculation. These values are used for olivine mineralogy as it forms the dominant mineral phase above 410 km depth. At the depth of 550 km, we assume ringwoodite mineral assemblage, and hence laboratory experiments with this silicate phase are needed. Experiments by Fei et al. (2017) determined dislocation annealing-based mobility and its Arrhenius-dependence for both wet ringwoodite and bridgemanite at the appropriate mantle temperature and pressure. Here we use their estimates of activation enthalpy and the same value for activation volume as in Fei et al. (2017) to arrive at an estimate of the effective viscosity at 550 km depth.

The conversion of mantle shear velocity to mantle viscosity relies on the assumption that temperature variations are responsible for variations in both shear velocity and viscosity. However, other factors, particularly variations in mineralogy and volatile content, will also influence shear velocity. Here, the factor β ranges from 0 to 1, and is meant to account for effects on shear wave velocity other than temperature (H. Wang et al., 2008). In the GIA analysis of Wu et al. (2013) β is used to relax the amplitude of the scale factor in fits to GIA-related data sets. In GIA analysis it forms a way of assessing the relative role of temperature in comparison to other factors affecting both the seismic velocity and $\log_{10}\Delta\eta$.

6.2 Calibration of Approach 1

The recent Maxwell viscoelastic models for GIA developed during the past decade in Antarctica are used for calibration (see Section 5.4). These model-based estimates are a potential source for placing realistic constraints on the parameter choices for the viscosity conversion. The extremely low upper mantle viscosity estimates of $1-4 \times 10^{18} \text{ Pa s}$ in the Northern Antarctic Peninsula and the Amundsen Sea Embayment can only be approximately fit using the IJ05-R2 upper mantle reference viscosity model of Ivins et al. (2013), which has the lowest continent-wide 1-D upper mantle viscosity ($2 \times 10^{20} \text{ Pa s}$). Providing an acceptable match to these GIA-modeled observations also requires that shear velocity variations result entirely from thermal variations (i.e., $\beta = 1$), at least in West Antarctica. A β close to 1 is compatible with evidence from compositional modeling indicating that temperature variations have the largest effect on mantle shear velocities, as realistic compositional variability produces only modest changes in seismic velocity (e.g., Goes et al., 2000; Lee, 2003, and others), and melt extraction produces only minor velocity increases in the upper mantle (Afonso & Schutt, 2012).

A complete absence of compositional influence on shear velocities is unreasonable in East Antarctica, a craton which is underlain by thick continental lithosphere. On a global comparative basis, such lithosphere has been shown to be depleted, with high Mg/Fe ratios producing fast seismic velocity anomalies (e.g., Jordan, 1981; van der Lee, 2001; Lee, 2003). Thus, we use $\beta = 1$, but the high mantle shear velocities in the upper reaches of the East Antarctic mantle are reduced by an appropriate factor prior to viscosity conversion. Assuming that depletion affects mantle shear velocity at the ~2% level, Approach 1 makes a depletion correction by subtracting up to 1.7% from East Antarctic velocity anomalies greater than 3%, with the correction increasing with increasing velocity anomaly. The magnitude of this correction is based on both xenolith data from outside of Antarctica (Lee, 2003) and petrological modeling (Afonso & Schutt, 2012).

Clarification of the role of globally averaged T_0 is important. Thermal convection in the upper mantle causes the globally averaged temperature gradient to deviate from an isentropic geotherm. However, using a common temperature for $T_0(r)$ allows internally consistent results to be employed that come from high pressure experimental and theoretical thermal elasticity. In Table 2 we give values for T_0 that span relatively hot and cold subcontinental mantle environments and a global average estimate. This is important, because in the shallow upper mantle where the anelastic influence on $\delta \ln v_s$ is largest, the total $\log_{10} \Delta \eta$ predicted is sensitive to the choice of geotherms, as shown in Figure 5 where we employ the 'hot' and 'cold' examples alongside the global average (see Table 2) as a function of the activation enthalpy for anelastic mobility.

7 Approach 2

7.1 Methods for Approach 2

A second method is now introduced which builds on the formulation of Ivins and Sammis (1995) as written in Equation (25), but accounting for the anelastic effects, as represented in the second term on the right hand side of Equation (26). Here we will disambiguate the components of the anharmonic ("ah") and anelastic ("an") contributions to the velocity anomaly, to aid in deciphering sources of error and bias.

The observed shear wave velocity anomaly can be partitioned as

$$\delta \ln v_s = \delta \ln v_s^{(ah)} + \delta \ln v_s^{(an)}. \quad (28)$$

All of the approaches essentially assume that $\delta \ln v_s^{(ah)}$ has a thermal origin.

One might logically ask: to zeroth order what is the temperature deviation from spherically averaged value that is caused by anelasticity? A zeroth order estimate of the thermal anomaly is

$$\delta T = -\frac{1}{\alpha_{th}} \frac{2}{(c_1 - 1)} \cdot \delta \ln v_s. \quad (29)$$

We should note that derivations of the theoretical anharmonic estimates of δT , as in Equation (29), depend on the exact flavor of the experimental and theoretical representations used, but at a basic level each must deal with the Grüneisen parameter and the temperature derivatives of the elastic moduli (e.g., Isaak et al., 1992; Núñez-Valdez et al., 2013).

The anelastic effect depends on the seismic shear wave attenuation Q_s . The physics describing this attenuation is more nuanced than is the description of seismic wave velocity using the theory of thermal elasticity. At the grain boundary level and interior to rock grains, some strain during seismic wave propagation involves motions that cannot be described with elasticity because they involve microstructural imperfections. Although the causal mechanical interactions at grain boundaries and of interior dislocation distortions and point

defect motions may be numerous, one feature is clear: they are highly sensitive to temperature through thermally activated processes (e.g., Schwarz & Granato, 1975). Hence, these processes are also described by an Arrhenius temperature-dependence with an activation enthalpy, H_D^* (e.g., Karato & Spetzler, 1990; Gribb & Cooper, 1998).

Karato (1993) found an approximate solution for the amplitude of the incremental diminution in velocity that is a function of this temperature anomaly and that is related to the observed shear wave seismic Q_s and the activation enthalpy

$$\delta \ln v_s^{(an)}|_{\delta Q} = -\frac{H_D^*}{\pi R_G T_0 Q_s} \cdot \frac{\delta T}{T_0}. \quad (30)$$

Equation (30) shows the strongly non-linear relationship between seismic velocity and the thermal anomaly ratio $\delta T/T_0$. This particular form is strictly valid for the case of frequency-independent Q_s . Such a lack of dependency is consistent with the construction of ANT-20 using the Durek and Ekström (1996) mantle Q_s model. A rederivation of the frequency-dependent equivalent, however, shows that the approximation by Equation (30) is nonetheless accurate to 10% provided the power exponent of the frequency-dependence is less than 1/2, consistent with experimental estimates (Jackson & Faul, 2010; Faul & Jackson, 2015). We term this H_D^* in Equation (30) as the activation enthalpy of attenuation. We note that Equation (30) is consistent with the anelasticity effect on S-wave velocity written by Takei et al. (2014) for high temperature background dissipation (equation 26 therein). This allows a first order anelastic correction to be applied to the observed S-wave anomaly map. The anharmonic anomalies can be calculated from the observed S-wave anomalies ($\delta \ln v_s$) as

$$\delta \ln v_s^{(ah)} = \delta \ln v_s - \delta \ln v_s^{(an)} = \delta \ln v_s \left[1 - \frac{2H_D^*}{\pi R_G T_0^2 Q_s \alpha_{th} (c_1 - 1)} \right]. \quad (31)$$

This result is essentially all that is needed to employ the method originally proposed by Ivins and Sammis (1995) that lacked corrections for temperature-dependent modulus dispersion (anelasticity). With this correction, we simply note that

$$\frac{\delta v_s}{v_{S_0}} \rightarrow \delta \ln v_s^{(ah)} \quad (32)$$

in Equation (25), and no other change needs to be applied in generating maps of $\log_{10} \Delta \eta(r, \phi, \theta)$.

The advantage of computing the velocity anomaly explicitly with Equation (31) is that the dependence on the seismic quality factor, Q_s , can be appropriately tailored to any attenuation model, whereas this cannot occur when employing the derivatives $[\partial \ln v_s / \partial T]_{\text{total}}$ tabulated in

Karato (2008). There is little fundamental difference in the way Approach 1 and 2 treat anelasticity. However, for Approach 1 all of the anelastic corrections are captured in the single term $[\partial \ln V_s / \partial T]_{\text{total}}$ and these may be recovered from a table of values supplied by Karato (2008). For Approach 2, this term is disambiguated into its constituent parts, thus aiding in developing formal uncertainties as they relate to the formal uncertainties of those constituent parameters.

7.2 Parameter Sensitivity

A large body of experimental results quantify the spectrum of transient relaxation mechanics associated with thermally activated anelastic dispersion for olivine aggregates at high temperature ($1173 \leq T \leq 1473^{\circ}\text{K}$) and pressure ($\sim 0.2\text{GPa}$) (e.g., Jackson et al., 2002; Jackson et al., 2004; Jackson & Faul, 2010; Jackson et al., 2014; Faul & Jackson, 2015). Included are least-square fits to the experimental parameters on ensembles of samples strained under oscillatory conditions. These yield values for the activation energy for anelastic dispersion E_D^* and, together with an estimate of the activation volume, V_D^* , we can assemble a large number of estimates of H_D^* .

There is considerable sensitivity of the computed values of $\log_{10}\Delta\eta$ at our depths of interest to c_1 and H_D^* and we therefore sample a range of probable values. In Figures 6 and 7 we demonstrate the important role of H_D^* in determining the total lateral variation in viscosity for a 2% δV_s seismic anomaly. The grey zone represents the breadth of values recommended by Karato (2008) and which satisfy laboratory values reported by Jackson and Faul (2010). The vertical dash-dot lines in Figures 6 show a value of H_D^* also determined by Jackson et al. (2014) using an alternative parameterization of torsional experimental data and modeling of deformation in dry olivine. The latter quantified $E_D^* = 259 \pm 25$ kJ/mol with $V_D^* = 10 \times 10^{-6} \text{ m}^3/\text{mol}$. Clearly, the latter parameterization has a large impact on the interpretation of $\log_{10}\Delta\eta$ in terms of the observed lateral variability in S-wave velocity. A logical deduction from Figures 6 and 7 is that progress in theoretical and experimental interpretations of seismic anelasticity does impact our ability to make predictions of $\log_{10}\Delta\eta$ in Antarctica.

7.3 Calibration of Approach 2

Calibration of Approach 2 uses only past inferences of effective upper mantle viscosity in the Northern Hemisphere. The quality and abundance of the RSL and geodetic data in Fennoscandia makes it an ideal location for calibration, considering that our reference parameterization is global in nature. Studies which rely on the exponential decay curves of Holocene near-field uplift are especially important in Fennoscandia and Hudson Bay (e.g., Mitrovica, 1996; Kuchar et al., 2019). The strongest sensitivity of these studies to the effective mantle viscosity is in the mid-upper mantle depth range. An ensemble of Fennoscandian ice sheet reconstructions by Nordman et al. (2015) demonstrated that the GIA model solutions for upper mantle viscosity using the sea-level emergence record along the river valley of Ångermanälven on the western coast of the Gulf of Bothnia are decoupled from uncertainty in the ice loading model. Such decoupling is critical to recovering tight

bounds on the upper mantle viscosity, since the exponential decay of the rate of land emergence can be tightly coupled to the viscosity (e.g., Kleemann & Wolf, 2005). This fact motivates calibrating the $\eta_0(r)$ to the experimentally developed flow law in Approach 2.

We place the activation enthalpies from experiments by L. Hansen et al. (2011) that determined the flow law for GBS dislocation mechanism into the approximation for effective viscosity using Equation (14), resulting in

$$\bar{\eta} = \frac{1}{2A_{GBS}} \sigma^{1-n_{GBS}} \cdot d^{p_{GBS}} \exp\left[H_{GBS}^*/R_G T\right]. \quad (33)$$

In L. Hansen et al. (2011) experimental data were fit with $A_{GBS} = 10^{4.8} \pm 0.8 \mu\text{m}^{p_{GBS}}$ MPa $^{-n_{GBS}}$ sec, $n_{GBS} = 2.9 \pm 0.3$, $p_{GBS} = 0.7 \pm 0.1$ and $H_{GBS}^* = 445 \pm 20$ kJ/mol.

At an average background deviatoric flow stress $\sigma = 0.5$ MPa and a mantle depth of 220 km, where $T_0 \approx 1500^\circ\text{K}$ (Davies et al., 2012), we can obtain quite plausible values for $\bar{\eta}$. Toward this aim, the value of activation volume, $V^* = 18 \times 10^{-6} \text{ m}^3/\text{mol}$ suggested by L. Hansen et al. (2011) is also employed. At a depth 220 km, hydrostatic pressure is roughly 7.1 GPa, and accounting for the confining pressures of the experiments (300 MPa) to determine the effective activation energy: $E^* \approx 439.6$ kJ / mol. We find, with a grain-size, d , of 4.5 mm, as suggested for application to the mantle by L. Hansen et al. (2011), and the appropriate hydrostatic pressure at this depth, $\bar{\eta}_{220\text{ km}} = 5.56 \times 10^{20}$ Pa s. This is a value quite consistent with what we know from GIA data-based inferences in central Canada and the Gulf of Bothnia (e.g., Wolf et al., 2006; Nordman et al., 2015), sites of relatively cold lithosphere. We note that GBS rheology is not assumed in Approach 1, so comparisons between the predictions of Approaches 1 and 2 may reveal biases that are tied specifically to the assumption of flow mechanism.

To derive an estimate of the effective viscosity at 550 km depth, we use the parameters derived by Fei et al. (2017) for hydrous ringwoodite. Using the activation enthalpy determined for ringwoodite (and activation volume, temperature and pressure estimate, see Table 4), we can estimate viscosity only by somewhat arbitrarily selecting additional parameters which have been derived in experiments for olivine, specifically using Equation (12) with $A = 1600$, $d = 25.5$ mm, $\bar{r} = 1.2$, $p = 3$, $\alpha = \phi = 0$, and $n = 3.5$, $\sigma = 0.2$ MPa (c.f., Hirth & Kohlstedt, 2004). With these, we calculate $\bar{\eta}_{550\text{ km}} = 6.0 \times 10^{20}$ Pa s, quite close to the most probable global value based upon a Bayesian statistical GIA analysis using global RSL and GPS vertical trend data sets by Caron et al. (2018). The estimates that we have made calibrate the H^* and temperature at depth estimations we employ for $\log_{10}\Delta\eta$. Ultimately the predictions should also be tested against Antarctic GIA inferences as in Approach 1.

7.4 Uncertainty Quantification

We give the predictions of the formal uncertainties in lateral variations of viscosity in Figure 8. The uncertainties are constructed from a combination of Equations (25) and (29) through (32) yielding:

$$\log_{10}\Delta\eta = \frac{2MH^*}{R_G\alpha_{th}T_0^2(c_1-1)} \delta\ln\nu_s \left[1 - \frac{2H_D^*}{\pi R_G\alpha_{th}T_0^2Q_S(c_1-1)} \right], \quad (34)$$

and then taking partials with respect to each of the parameters. Note that in writing Equation (34) that all the parameters which have model uncertainties are revealed. Assuming that H^* , H_D^* , α_{th} , T_0 and c_1 are the important contributors to the uncertainty of the viscosity variations, and that they follow a Gaussian distribution, we can calculate the uncertainty of $\log_{10}\Delta\eta$ as the following:

$$\sigma_{\log_{10}\Delta\eta} = \sqrt{\sum_{\sigma_x=\{H^*, H_D^*, \alpha_{th}, T_0, c_1\}} \left(\frac{\partial \log_{10}\Delta\eta}{\partial x} \sigma_x \right)^2}, \quad (35)$$

with partial derivatives formed from Equation (34) and the symbol σ_x representing any one of the error estimates of the corresponding parameters in the sum. For example,

$$\frac{\partial \log_{10}\Delta\eta}{\partial H_D^*} = -\frac{4MH^*}{\pi Q_S [R_G(c_1-1)\alpha_{th}]^2 T_0^4} \cdot \delta\ln\nu_s. \quad (36)$$

We give parameters assumed for the maps of Figure 8 in Table 4. These are guided by the parameter studies conducted as in Figures 6 and 7. Note that the estimates provide uncertainties for the viscosity conversion, but do not take into account any uncertainties in the shear velocities in the seismic model ANT-20. Furthermore, larger uncertainties than we can quantify here may be associated with unknown variability in composition, grain-size, or water. Deep uncertainty is also associated with the arbitrary selection of the effective Newtonian viscosity $\bar{\eta}$ from among the various constant background forms of Equations (13), (14) and (15). Figure 8 allows a view of the formal uncertainties derived from the sum of an enumerable set of parameter uncertainties. Note that the larger uncertainties are obtained for regions with larger amplitude velocity anomalies. The continuing advances in the model interpretations of creep and anelasticity from static creep and torsion experiments, respectively, must temper any over-interpretation of these uncertainty maps.

8 Approach 3

8.1 Methods for Approach 3

The roots of Approach 3 have been applied previously to Antarctic rebound by van der Wal et al. (2015). The temperature, $T_0 + \delta T$ is obtained following the description in Section 5.2 and inserted into a fully robust olivine flow law. The flow law allows diffusion, intragranular dislocation creep and GBS creep mechanics to operate simultaneously, each contributing to the macroscopic mantle strain (e.g., Ranalli, 2001; Barnhoorn et al., 2011; Kohlstedt & Hansen, 2015).

Dislocation creep is nonlinearly related to stress as has already been discussed. Viscosity, therefore, also carries this nonlinear dependence, as is readily deduced from Equations (9) and (16). van der Wal et al. (2013) formulates the composite rheology with the intent of solving time-dependent GIA loading-unloading problems in which effective viscosity evolves in time, as does the deviatoric stress and strain rate. However, here we desire a simpler approach, one that would facilitate inter-comparison with the predictions of Approaches 1 and 2. We provide estimates for a constant stress state. Using the seismic velocity anomaly model ANT-20, the relative change in viscosity is computed as in Equations (26) and (27). The spherically averaged global background temperatures used are identical to Approaches 1 and 2 as described in Table 2. The derivatives of seismic velocity anomaly to temperature anomaly are provided as a function in depth in Karato (2008), thus accounting both the anelastic and anharmonic contributions to S-wave velocity perturbations.

Unique to Approach 3 is that we add this microscopic contributions to the strain rate owing to diffusion, dislocation and GBS mobility in the following way

$$\dot{\epsilon}_{tot} = \dot{\epsilon}_{dif} + \dot{\epsilon}_{disc} + \dot{\epsilon}_{GBS}, \quad (37)$$

wherein the subscripts 'tot', 'dif', 'disc' and 'GBS', refer to total strain rate and the diffusional, dislocation and GBS contributions, respectively. We note that we cannot employ a simple form like in Equation (33), but rather we need forms like

$$\dot{\epsilon}_{GBS} = A_{GBS} \sigma^{n_{GBS}} d^{-p_{GBS}} \exp\left[-\left(E_{GBS}^* + PV_{GBS}^*\right)/R_G T\right], \quad (38)$$

with the appropriate constants found in L. Hansen et al. (2011). Similar relations apply to the dislocation and diffusional component of the strain rate. To complete the evaluation of effective viscosity the resultant $\dot{\epsilon}_{tot}$ is employed in Equation (16) with a constant stress selected. The grain-size and stress are taken as constants and set to 4 mm and 0.1 MPa, respectively, for the purposes of our map computation shown in Figures 10c and 11c. The experimentally-based flow parameters of Approach 3 are summarized in Table 5.

As in Approaches 1 and 2 we assume the ringwoodite phase dominates at the 550 km depth. Here, however, we select experimental results published by Kawazoe et al. (2016). In Figure 9 we show the lateral variability in viscosity that is predicted if we assume the parameters that are derived from experiments with ringwoodite at 18 GPa by Kawazoe et al. (2016). The experiments of Fei et al. (2017) used an annealing technique to obtain activation enthalpy values for dislocation mobility at temperatures and pressures relevant to the 550 km depth. However annealing experiments do not apply a controlled shear stress and hence are not capable of determining a flow law. By contrast, the deformation experiments by Kawazoe et al. (2016) allowed a dislocation creep law to be derived, but with rather large uncertainties on the activation enthalpy. For a fit to the data in which power exponent n was fixed to 3, $H^* = 345 \pm 90$ kJ/mol, and when n was simultaneously solved for using the data: $H^* = 279 \pm 105$ kJ/mol, with $n = 2.4 \pm 0.7$. In Figure 9 we see that for a 2% S-wave anomaly a discrepancy of no more than about 20% arises from the two differing fits to the data of Kawazoe et al. (2016). At 550 km depth it is also probable that diffusion at grain boundaries contributes, and Shimojuku et al. (2009) provided diffusion constants for Si and O atomic

species with activation enthalpies at 402 and 246 kJ/mol, respectively. We can use the former slowest diffusing species as rate controlling for diffusion creep in ringwoodite and form an estimate for the composite strain rate limited to $\dot{\epsilon}_{df}$ and $\dot{\epsilon}_{disc}$ in Equation (37). We note that the dislocation component dominates any reasonable estimate of the total strain rate, and, therefore, primarily reflects the estimate of the viscosity that is mapped in Figure 12 c.

Unlike Approaches 1 and 2, wherein the full forms of the experimental flow laws are used for calibration purposes, the mapviews generated for Approach 3 for 150 km and 300 km depths attempt to explicitly use the experimentally determined prefactor and grain-size (Figures 10c and 11c). For the ringwoodite mineralogy it is more difficult to generate prefactors directly from the experiments and there are no experiments that collectively reveal the grain-size dependence. For computing frame (c) of Figure 12 we set stress to 0.002 MPa and derive a self-consistent prefactor.

8.2 Calibration of Approach 3

The largest uncertainties in obtaining effective viscosity from Approach 3 comes from the grain-size, water content and stress (Hirth & Kohlstedt, 2004; O'Donnell et al., 2017). Effective viscosity is very sensitive to these values, because no average viscosity is assumed in the calculation of effective viscosity. To establish that the approach is realistically retrieving effective viscosity, model predictions can be compared to GIA data. The general composite approach with both linear (diffusion control) and non-linear (dislocation control) constitutive relations are employed in computing predictions of vertical land motion and compared to GPS observations in Antarctica (van der Wal et al., 2015), Fennoscandian RSL and GPS crustal motion data (e.g., Tushingham & Peltier, 1992; Lidberg et al., 2010), and GRACE gravity trends (e.g., van der Wal et al., 2013). The computations are also used to estimate the GIA correction for the present-day mass balance of the Antarctic and Greenland ice sheets (e.g., Bouman et al., 2014; Xu et al., 2016). In general, a rheology with grain sizes of 4 mm, or larger, resulted in better fits to the uplift and gravity trend data sets. In contrast, a lower viscosity associated with smaller grain-size and wet rheology predict GIA signatures that underestimate the observed uplift rates. The dry rheology with 4 mm grain-size is the preferred model in van der Wal et al. (2013) and is used here as the reference model. A stress of 0.5 MPa is assumed, a representative stress level for GIA induced stress beneath the lithosphere locations underneath and near the margin of an ice sheet (van der Wal et al., 2010). Mantle stress levels, however, depend not only on the stress induced by GIA, but also on mantle convection (Bredow and Steinberger, this volume). There are some important caveats regarding our preferred grain-size and water content values. Firstly, it is cautioned that these results are obtained with ice loading histories that are implicitly based on 1D Earth profiles of linear viscosity. Progress with ice histories based on composite rheology are under investigation (Huang et al., 2019). Second, on the basis of xenolithic rocks recovered in Antarctica (see Chatzaras and Krukenberg, this volume), small grain sizes and wet olivine cannot be excluded (e.g., van der Wal et al., 2015; Chatzaras et al., 2016).

9 Mapviews Predicted by the Three Approaches

Viscosity variation in \log_{10} units in plan view is predicted using the three approaches at the three inter-comparative upper mantle depths. The predictions are given in Figures 10, 11 and 12.

9.1 Synopsis of Results for Approach 1

The resulting predictive model from Approach 1 is generally in approximate agreement with the ice-load geodetic viscosity estimates mentioned above (see frame (a) of Figures 10, 11 and 12 that show the three depth predictions). For example, in the Amundsen Sea Embayment, the modeled effective viscosity for the asthenosphere shallower than 200 km is 5×10^{18} Pa s, compared to 4×10^{18} estimated by Barletta et al. (2018). The modeled values for the rest of the upper mantle are somewhat higher than in Barletta et al. (2018), but still within a half of an order of magnitude. We note that in a GIA-LV model, Powell et al. (2020) inferred a viscosity in this same region of 2×10^{18} Pa s. The prediction of Approach 1 is unable to match the extremely low viscosity ($\sim 1 \times 10^{18}$ Pa s) estimated for the Northern Antarctic Peninsula, and near Graham Land, by Simms et al. (2012) and Nield et al. (2014), yielding 7×10^{18} Pa for 65–200 km depth, and higher viscosity values at greater upper mantle depths. At a depth of 550 km, lateral variability is further reduced, and predicted effective viscosity is close to 10^{20} Pa s. At this depth two regions, one in West Antarctica and the other in East Antarctica beneath Wilkes Subglacial Basin, have viscosity predicted to be near $4–8 \times 10^{19}$ Pa s.

9.2 Synopsis of Results for Approach 2

Figure 10b shows the predictions for Approach 2 at 150 km depth. Here much of East Antarctica has an effective viscosity η_σ , of slightly above 10^{21} Pa s, rising to just above 10^{22} Pa s in a cratonic core region that extends ~ 1100 km from the South Pole into the interior of East Antarctica and along the Wilkes Subglacial Basin. At 150 km beneath West Antarctica η_σ is predicted to be between about 2×10^{19} to 10^{20} Pa s. A viscosity as low as 10^{18} Pa s is predicted southwest of the Balleny Trough in the Indian Ocean and 20 degrees latitude north of Marie Byrd Land in the Pacific Ocean sector, each being far from the Antarctic continent. The $1-\sigma$ uncertainties propagated from the experimentally based parameters might allow for the West Antarctic mantle effective viscosity to be lowered to just below 10^{19} Pa s.

At 300 km depth (Figure 11b) the East Antarctic pattern is similar to 150 km. However, at this depth a large swath of the subcontinent extending from the coast adjacent to Wilkes Subglacial Basin to the southern Antarctic Peninsula and Weddell Sea region is essentially Fennoscandian in character ($\eta_0 \sim 4 \times 10^{20}$ Pa s). Along this swath our $\bar{\eta}$ (η_σ) takes on values near $3–8 \times 10^{20}$ Pa s. A portion of coastal West Antarctica and Marie Byrd Land may be in the range $0.9–10 \times 10^{19}$ Pa s, not too different in value from 150 km depth prediction, but now of smaller overall regional extent. Again, the $1-\sigma$ uncertainties could allow predictions to descend to values slightly below 10^{19} Pa s in a small section of the mantle beneath Marie Byrd Land. (At this 300 km depth beneath Marie Byrd Land, P-wave tomography by Lucas et al. (2020) shows this region has a robust slow anomaly relative to surrounding West Antarctic mantle). The variability predicted at 550 km depth (Figure 12b) is much reduced, with viscosity everywhere below 10^{21} Pa s, and is similar to that predicted by Approach 1.

We anticipate for all approaches that there will be large viscosity contrasts located at the upper half of the upper mantle, for it is here where convective temperature and partial melts may express themselves strongly (e.g., Yuen et al., 1993; Vacher et al., 1996). Indeed, we see that about 4 orders of magnitude characterize the prediction shown in Figure 10 for each

frame at 150 km depth when considering both continent and oceanic regions in mapview. Excluding variability beneath oceanic crust in Figure 10, the variability reaches approximately 3 orders of magnitude. The largest variation occurs between coastal Marie Byrd Land, a region known for active volcanism, and the East Antarctic craton. At 300 km depth 4 orders of magnitude variability is also reached if we include oceanic mantle. Hot oceanic upper mantle may be the site of highly channelized flow, at least in some interpretations of $\delta\ln\nu_s$ at this depth (e.g., French et al., 2013). Our focus, however, is on mantle beneath the continent of Antarctica where it is possible to retrieve corroborative viscosity information using bedrock geodesy.

At the depth of 550 km we predict that lateral variability is much reduced, and, in fact seems characterized by 1 to 1.5 orders of magnitude. This is caused by the smaller activation enthalpy for ringwoodite (see Table 4). We cautiously note that while Fei et al. (2017) discovered substantial variability, possibly from water content, we have not modeled this possible origin for lateral variability in rheology, for seismic models like ANT-20 are unlikely to deliver the required quantitative information.

Confining the assessment to West Antarctic mantle, the contrast in effective viscosity reduces to a little less than three orders at 150 km and 300 km depths. We carefully note that examination of Figure (6a) reveals that a reduction of the anelastic activation enthalpy, H_D^* , from 394 kJ/mol, assumed for the predictive maps, to 307 kJ/mol, a value preferred in the summary of Jackson et al. (2014), increases the \log_{10} variability by a factor of 1.56 at 150 km depth. Regardless of which value is assumed, Approach 2 predicts strong contrasts that will influence various ice history-geodetic solutions for mantle viscosity estimated through comparison to GPS crustal motions. This is because of the regional viscosity has an exponential control on the isostatic decay time. Note that the preliminary 1- σ errors at 150, 300 and 550 km do not alter this conclusion.

9.3 Synopsis of Results for Approach 3

The predictions using Approach 3 are distinctive in that they are constructed with the assumption of composite micromechanics and explicit adoption of the corresponding flow laws, at least at depths of 150 and 300 km. At a depth of 150 km the cratonic mantle beneath East Antarctica is predicted to be $10^{22} - 10^{23}$ Pa s, and possibly higher in some locations (Figure 10 c). This high viscosity extends well into the surrounding oceanic environment. A small portion of the Antarctic Peninsula and Marie Byrd Land are predicted to be near 10^{19} Pa s, and a small region well offshore beneath the Balleny Trough effective viscosity is predicted to be a few times 10^{18} Pa s. At this same depth there is a 3 orders of magnitude gradient in viscosity predicted on-continent between the southern Transantarctic Mountains and Marie Byrd Land.

Viscosity at 300 km depth is predicted to be a few times 10^{18} Pa s in oceanic regions (Figure 11 c). This prediction of sub-oceanic mantle viscosity is a ubiquitous feature, except in the Weddell Sea region. The Marie Byrd Land viscosity prediction is near 5×10^{18} Pa s. A narrow corridor of viscosity beneath West Antarctica extends from northern Victoria Land to Thurston Island and west of the Bellingshausen Sea that is below about 6×10^{19} Pa s. A somewhat parallel band of Fennoscandian-like viscosity extends from just south of the Balleny Trough to the western Weddell Sea and northern Antarctic Peninsula. Also, East

Antarctica is predicted to have a distinctively Fennoscandian character from the coast to 500 - 1000 km into the interior from 0° E to 90° E. At 550 km depth Approach 3 predicts two pockets of relatively low viscosity ($\geq 3 \times 10^{19}$) Pa s beneath Marie Byrd Land and Wilkes Subglacial Basin (Figure 12 c). Nearly all other regions are near Fennoscandian values, except for small pockets just west of the Syowa Coast and in the Antarctic Peninsula region where viscosity values are predicted to be in the 10^{21} to 10^{22} Pa s range.

10 ANT-20 Based Viscosity Versus Model Inferences

It is useful to display the GIA model results and the predictions of scaled effective viscosity at 150 and 550 km depths alongside one another, as is done in Table 6. Here we have not listed GIA models and our predictions at 300 km depth because the cases of 1-D model viscosity at that depth are identical to the value assumed at 150 km. In Table 6 only the study by Powell et al. (2020) assumed a GIA-LV (3-D) model. Differences among GIA model predictions can arise from differences in the details of the GPS time series employed, the ice load history or depth parameterization. Given the underlying deep uncertainty in parameterizing the scaling factor *and* the fact that the values of the viscosity that best fit geodetic data depends on the selection of the model thickness of the uppermost mantle layer (e.g., Hu & Freymueller, 2019), we caution against over-interpreting Table 6.

10.1 Assessment using ice history-geodetic estimates of viscosity

Given the simplicity of our assumption that seismic tomography can be used to infer temperature, and therefore an effective viscosity, it should not be too surprising to find deficiencies in correlating mapped 1-D viscosity to mapped shear wave speed. Lateral heterogeneity in water or melt content, chemistry, anisotropy may also influence the viscosity and seismic velocity fields, and these factors we have not attempted to account for. However, when comparing our results from the three approaches we find general agreement with geodetic and paleosealevel inferences of effective viscosity from GIA modeling. Basically, all three methods predict high viscosity beneath East Antarctic cratonic lithosphere and low viscosity beneath West Antarctica, with the centers of predicted low viscosity beneath Ross Island and Marie Byrd Land, sites of extensive Quaternary volcanism (e.g., Kyle, 1990; Wilch et al., 1999; Smellie et al., 2021).

Low viscosity regions are also imaged along the Amundsen Sea Coast and the Antarctic Peninsula. Furthermore, there are vast and continuous swaths of mid-level upper mantle where Fennoscandian-like viscosity (e.g., Mitrovica, 1996; Lidberg et al., 2010; Nordman et al., 2015) is predicted, consistent with inferences of a number of continent-wide 1-D GIA models (e.g., Whitehouse et al., 2012; Ivins et al., 2013; Argus et al., 2014). Among the most notable failures of the continent-wide 1-D GIA models is their inability to predict large present-day vertical uplift on bedrock sites in the Amundsen Sea Sector (e.g., Groh et al., 2012), several hundred km from the Voigt-averaged S-wave anomaly minimum of ANT-20 beneath Marie Byrd Land. A low viscosity region is predicted in this general region by each of the three approaches at 150 and 300 km. This is quite generally in accord with inferences of low viscosity that come from regional GIA modeling (e.g., Barletta et al., 2018; Powell et al., 2020; Kachuck et al., 2020). As we have discussed in reference to each of the predictions from the three approaches, there is discord on the magnitude of the inferred viscosity minimum. We do not speculate further on the causes of such a discrepancy. The list might include: seismology, poor ice reconstruction, insufficient layering, low-temperature plasticity,

transient creep or subtle effects of the heterogeneity itself. However, a positive result of our study is that the viscosity contrasts inferred from scaling seismic tomography to temperature, and then to viscosity, do correlate well with the patterns of upper mantle viscosity inferred from GIA models that are well-rooted in geodetic observation.

10.2 Scrutiny of the Antarctic Peninsula

The northern Antarctic Peninsula (Graham Land) is one region that rather poorly correlates with the ANT-20 scaling to viscosity in at least two of the three approaches, as each are limited to treating lateral variability as dominated only by thermal control. The most optimistic correlation is predicted by Approach 1 at $z = 150$ km (see Figure 10a). Models by Simms et al. (2012) and Nield et al. (2014) infer shallow upper mantle viscosity in the range of 0.7 to 2×10^{18} Pa s. The viscosity we present in this Chapter based upon scaling to ANT-20 is nearly an order of magnitude higher than this at all depths we compute and for all approaches, presenting a challenge for interpretation.

In dealing with this enigma, three candidate causes are of primary consideration. First, there are potential changes in mantle grain-size and volatile content caused by a youthful ridge subduction tectonics that characterize the northernmost Peninsula upper mantle environment (e.g., Bercovici et al., 2015). Secondly, is a resolution issue: A sharp variation in viscosity near the Bransfield Strait spreading center might be captured in the geodetic data, but smeared out in the Voigt-average ANT-20 model. Generally, the model has approximately 150–200 km lateral resolution and about 50 km depth resolution at 150 km depth, but this resolution diminishes with depth. Thirdly, is the possibility that both the GIA forward model set-ups and the experimental flow laws assume 'steady-state' properties, the former from the Maxwell viscoelastic assumption and the latter from creep experiments that have reached steady-state, and therefore lack any transient behavior. We are not yet in a position to distinguish between these three possibilities, and any further elaboration should be tempered by the fact that a higher viscosity solution was derived from geodetic data by Ivins et al. (2011). The latter are seemingly compatible with two of the three predictions at 150 and 300 km depth, as these are between 1 to 9×10^{19} Pa s (cf. Figures 10a and b and 11a,b and c). Additional seismic imaging of the upper mantle in this complex region might shed further light on these issues (e.g., Park et al., 2012).

11 Discussion and Conclusions

The three inter-comparative approaches that we have used to convert the ANT-20 S-wave tomography of the Antarctic upper mantle to viscosity has been an exercise in testing for coherency in the resulting maps of $\log_{10}\Delta\eta(r, \theta, \phi)$, noting the considerable differences in the underlying assumptions and procedures. The contrasts in the approaches are substantial, as can be deduced from the summary Tables 1 and 3. In fact, what we have sampled, are methods that are in current use, and therefore give the reader a sense for the spread in results that underly any transfer function for S-wave images to $\log_{10}\Delta\eta(r, \theta, \phi)$ using laboratory-based steady-state flow laws. A more systematic study might be designed in the future that would consider a somewhat more broadened scope than what we have developed here.

A key part of this Chapter on rheology has been to revisit the issue of anelasticity in deriving quantitative relationships between lateral variation in effective mantle viscosity and S-wave velocity anomalies. Central to the physics of anelasticity are the grain-scale

deformation processes associated with seismic wave motion. During the past two decades, torsional oscillation studies of GBS and static creep deformation in olivine reveal that diffusional assisted interionic mobility is a key feature of seismic attenuation (e.g., Jackson, 2000; Marquardt & Faul, 2018). Here we have taken the basic approach outlined in the monograph of Karato (2008). As the process of seismic wave attenuation involves grain boundary assisted diffusion, an activation enthalpy of a transient creep, H_D^* , is a key controlling parameter. Our assessment employs experiments on olivine samples that are derived from torsional oscillation experimental work (e.g., Jackson et al., 2002; Jackson & Faul, 2010; Jackson et al., 2014; Faul & Jackson, 2015). However, these experiments are performed under an array of conditions (e.g., grain sizes, pressures, temperatures, synthetic preparation procedures, etc.) and, hence, there is a relatively broad range of H_D^* that may apply to the upper mantle beneath Antarctica.

Our results reveal that among competing parameters for calculations at $z = 150$ and 300 km for a 2% S-wave anomaly, H_D^* can have a half to full order of magnitude influence on the $\log_{10}\Delta\eta$ that is predicted. Approaches 1 and 3 have selected values for the anelastic correction that are taken directly from the numerical values as a function of depth as supplied by Karato (2008). Karato (2008) has cautioned about the sensitivity to the background Q_s model. However, we find that these cause negligible differences in the predictions among the three different approaches for Antarctic upper mantle. The background Q_s model used in construction of ANT-20 ($Q_s = 70$) differs only modestly from the model presented by Karato (2008) with $Q_s = 80$ at $z = 150$ km. In Figure 13 we explore the prediction for $\delta\ln\nu_s = -6\%$, a value characterizing the minimum S-wave velocity anomaly in ANT-20. Similar comparisons at 300 and 550 km depths lead to the same conclusions; that the differences in these particular Q_s models ($\mathcal{O} 10\%$) play a negligible role. However, if the background Q_s model is larger by a factor ~ 2 , then the inverted S-wave anomaly values increase (e.g., Lloyd et al., 2020) (see their Fig. S7). In addition, the influence on the anelastic correction would then be smaller, resulting in a larger prediction of $\log_{10}\Delta\eta(r, \theta, \phi)$ associated with a thermal perturbation $\delta T(r, \theta, \phi)$.

In Figure 13 we relax the rule of thumb suggested by Karato (2008) ($0.8 \leq \xi \leq 1$) in the relation $H_D^* \approx \xi H^*$. Jackson et al. (2014) suggest a relaxation in the lower bound on ξ , to allow $\xi \approx 0.5$. Such lowering of ξ is also consistent with the analysis of McCarthy et al. (2011). A reduction to this value does have some consequence. For example, the map of Figure 10b shows viscosity variability weaker than that allowed in Figure 13. At $H_D^* = 200$ kJ/mol (the lowest value of the shaded region in Figure 13), $\log_{10}\Delta\eta$ would be raised by about a half an order of magnitude with respect to values in Figure 10b if using this lower activation enthalpy for thermally activated anelasticity. Potentially, ambiguities in the range of acceptable H_D^* values are a possible source of bias in the results delivered by any one of the Approaches examined in this Chapter. In Figure 13 we see that the maximum diminution of viscosity at 6% S-wave anomaly is 3 orders of magnitude, but that 4 orders is never achieved, provided the anelastic correction is applied. Our Chapter concludes that future experimental and theoretical progress for improved constraints on anelastic H_D^* will aid in better constraining a priori lateral viscosity models derived from seismology.

One method that can account for the different creep mechanisms that correspond to laboratory derived flow laws is to abandon the use of viscosity as a single controlling parameter, and employ the creep law of Equation (9) directly into the initial-value boundary-value problem (IVBVP) code structure that solve geodynamic and GIA model setups. This, in fact, has been done in GIA models (e.g., Wu, 1999; Zhong et al., 2003). Diffusion, dislocation and GBS creep can operate simultaneously in the mantle (Ranalli, 2001; Kohlstedt & Hansen, 2015), and a composite rheology has been used in mantle convection (e.g., van den Berg et al., 1995; Becker, 2006; Dannberg et al., 2017) and in GIA models (e.g., van der Wal et al., 2013; Huang et al., 2019). In this case, a mean effective viscosity could only be defined as a retrospective summary of the class of full numerical simulations, should the fully nonlinear constitutive equations be employed. As our goal has been to discuss the rheology of the mantle beneath the Antarctic Ice Sheet that can be derived from a comprehensive S-wave tomographic image, we must acknowledge this limitation. Tractable relations between S-wave anomaly and the single Newtonian-like effective viscosity make bold approximations in order to be easily compared to viscosity derived from ice history-geodetic reconstructions of GIA (e.g., Ivins et al., 2011; Nield et al., 2014; Barletta et al., 2018; Powell et al., 2020). The latter models are nearly all based upon a Maxwell constitutive assumption and report a Newtonian viscosity value. Hence, the scaling methods explored in this paper have a practical utilitarian value since the preponderance of GIA models are 1-D and assume a Newtonian viscous element in a Maxwell rheology. An inherent goal of developing coherent transfer functions between tomography and viscosity is to develop more advanced 3-D structures for use in GIA models. For example, in a study of the ASE, Powell et al. (2020) show that the sensitivity of horizontal GPS station motions to 3-D structure is substantial. For regions peripheral to the locus of ice mass change, 3-D structure can also influence vertical motions since bulge migration involves lateral transport of mantle material (Klemann et al., 2007).

We conclude that the basic philosophy of deriving scaling relationships is a coherent and rationale one. With quantification and propagation of laboratory and seismically derived uncertainty, we are also able to describe some of the uncertainties in the scaling to effective regional viscosity. A future challenge may be to more fully explore various poorly understood biases, and to better understand the grain-size dependency and impurity effects in the deeper upper mantle for wadsleyite and ringwoodite mineralogy. The issue of lower mantle viscosity just below the 660 km discontinuity has important implications for the space gravimetric interpretation of present-day ice mass changes in East Antarctica, as shown recently by Caron and Ivins (2020). The coming decade will see the development of increasingly sophisticated numerical models for GIA-LV, possibly even those that will employ adjoint methods (e.g., Crawford et al., 2018). Critical to these advanced 3-D approaches is having high confidence in a starting model that is well rooted spatially. For this purpose, seismic mapping in the mantle will be a valuable tool. Among a number of caveats we have not touched on, the most important is the *other* implication of the mobility processes associated with the activation parameter H_D^* : transient rheology. In studies of post-seismic relaxation it is now widely acknowledged that this is a critical component of deformation models (e.g., Lau & Holtzman, 2019; Ivins et al., 2020). Transient rheology could help explain the high amplitudes of geodetically determined responses to decade time-scale ice unloading events in Antarctica. How to deal with this short time scale rheology will be a major future challenge.

Appendix A Linearization of the Thermal Perturbation

In this appendix we show the level of bias that is inherent to a linearization of δT in Equation (7). The approximation is technically unnecessary, but it eases a direct use of spherical harmonics for simultaneously treating global tomography models and semi-analytic formulations of the GIA-LV problem (e.g., Tromp & Mitrovica, 2000; Martinec, 2000; Tanaka et al., 2011). Spherical harmonic representation of the field $\log_{10}\Delta\eta(r, \theta, \phi)$ is then smoothed with the same resolution and fidelity as the seismic tomographic map of $\delta v_s(r, \theta, \phi)/v_{S_0}$ (e.g., Kaufmann et al., 2005). Additional terms in Equation (8) include

$$\frac{\log_{10}\Delta\eta}{a\log_{10}e} \approx -\frac{\delta T}{T_0^2} - \frac{\delta T^2}{T_0^3} - \frac{\delta T^3}{T_0^4} + \text{higher order terms.} \quad (\text{A1})$$

Comparison of the exact relation (Equation 7) and two levels of approximation are shown in Figure A1. Also shown here (dotted curve overlaying the yellow dash-dots) is the method of Latychev et al. (2005), which is also a 1st order approximation. The study by An et al. (2015) used a Rayleigh wave dispersion analysis to determine shear wave structure. It is of note that if we adjust the parameter ε of Latychev et al. (2005) in Equation (4) to a value of 0.067°K^{-1} the predictions become identical to the 1st order approximation that employ physics into the parameterization. This contrasts to the ε value assumed in the global modeling by Austermann et al. (2013), $\varepsilon = 0.04^\circ\text{K}^{-1}$, and to one of the values used for Antarctica by Hay et al. (2017) ($\varepsilon = 0.037^\circ\text{K}^{-1}$).

In Figure A2 we show the positions from the steady state thermal model computed by An et al. (2015) that are used in constructing Figure A1. Our method employed in this Chapter uses a different set of relationships to compute temperature as a vehicle to estimate lateral viscosity contrasts. Nonetheless, we use Meijian An's model as an independent method for estimating δT and T_0 for the Antarctic mantle. It therefore provides an independent way of testing the linear approximation for $\log_{10}\Delta\eta$ widely assumed in the GIA-LV modeling community (e.g., Hay et al., 2017; Powell et al., 2020).

Acknowledgments

We dedicate this Chapter to the memory of Orson L. Anderson and Donald L. Anderson. We thank the editor, Adam Martin, Pippa Whitehouse and two anonymous reviewers for quite thorough and helpful suggestions. This research was carried out at the Jet Propulsion Laboratory (JPL), California Institute of Technology, under a contract with the National Aeronautics and Space Administration (NASA) and funded through NASA Post-doctoral Program, and through NASA's Earth Surface and Interior Focus Area Program (grant #NNH15ZDA001N-ESI), the Sea-Level Change Science Team (grant #NNH16ZDA001N-SLCT), the GRACE Follow-On Science Team (grant #NNH19ZDA001N-GRACEFO) and the NASA Cryosphere Program.

References

- A, G., Wahr, J., & Zhong, S. (2013). Computations of the viscoelastic response of a 3-D compressible Earth to surface loading: an application to glacial isostatic adjustment in Antarctica and Canada. *Geophys. J. Int.*, 192(2), 557–572.
- Afonso, J. C., & Schutt, D. L. (2012). The effects of polybaric partial melting on density and seismic velocities of mantle restites. *Lithos*, 134-135, 289 - 303.
- Amalvict, M., Willis, P., Wöppelmann, G., Ivins, E. R., Bouin, M., Testut, L., & Hinderer, J. (2009). Isostatic stability of the East Antarctic station Dumont d'Urville from long-term geodetic observations and geophysical models. *Polar Research*, 28(2), 193-202. doi: 10.3402/polar.v28i2.6112
- An, M., Wiens, D. A., Zhao, Y., Feng, M., Nyblade, A., Kanao, M., ... Léveque, J.-J. (2015). Temperature, lithosphere-asthenosphere boundary, and heat flux beneath the Antarctic Plate inferred from seismic velocities. *J. Geophys. Res. Solid Earth*, 120(12), 8720-8742. doi: 10.1002/2015JB011917
- Anderson, D. L. (1987). A seismic equation of state II. shear properties and thermodynamics of the lower mantle. *Phys. Earth Planet. Interiors*, 45(4), 307 - 323. doi: 10.1016/0031-9201(87)90039-2
- Anderson, D. L. (1988). Temperature and pressure derivatives of elastic constants with application to the mantle. *J. Geophys. Res. Solid Earth*, 93, 4688–4700.
- Anderson, J. B., Conway, H., Bart, P. J., Witus, A. E., Greenwood, S. L., McKay, R. M., ... Stone, J. O. (2014). Ross Sea paleo-ice sheet drainage and deglacial history during and since the LGM. *Quatern. Sci. Rev.*, 100, 31 - 54. doi: 10.1016/j.quascirev.2013.08.020
- Anderson, O. L. (1995). *Equations of State of Solids for Geophysics and Ceramic Sciences*. Oxford University Press.
- Anderson, O. L., & Isaak, D. J. (1995). Seismic tomography and geodynamics. In T. J. Ahrens (Ed.), *Mineral Physics and Crystallography: A Handbook of Physical Constants*, AGU Reference Shelf, Volume 2 (p. 64-96).
- AGU. Anderson, O. L., Oda, H., & Isaak, D. (1992). A model for the computation of thermal expansivity at high compression and high temperatures: MgO as an example. *Geophys. Res. Lett.*, 19(19), 1987-1990. doi: 10.1029/92GL02145
- Argus, D. F., Peltier, W. R., Drummond, R., & Moore, A. W. (2014). The Antarctica component of postglacial rebound model ICE-6G_C (VM5a) based on GPS positioning, exposure age dating of ice thicknesses, and relative sea level histories. *Geophys. J. Int.*, 198, 537-563. doi: 10.1093/gji/ggu140
- Austermann, J., Chen, C., Lau, H., Maloof, A., & Latychev, K. (2020). Constraints on mantle viscosity and Laurentide ice sheet evolution from pluvial paleolake shorelines in the western United States. *Earth Planet. Sci. Lett.*, 532, 116006. doi: 10.1016/j.epsl.2019.116006

Austermann, J., Mitrovica, J. X., Latychev, K., & Milne, G. A. (2013). Barbados-based estimate of ice volume at Last Glacial Maximum affected by subducted plate. *Nature Geoscience*, 6(7), 553–557.

Barletta, V. R., Bevis, M., Smith, B. E., Wilson, T., Brown, A., Bordoni, A., ... Wiens, D. A. (2018). Observed rapid bedrock uplift in Amundsen Sea Embayment promotes ice-sheet stability. *Science*, 360, 1335–1339. doi: 10.1126/science.aao1447

Barnhoorn, A., van der Wal, W., Vermeersen, B. L., & Drury, M. R. (2011). Lateral, radial, and temporal variations in upper mantle viscosity and rheology under Scandinavia. *Geochemistry, Geophysics, Geosystems*, 12(1).

Becker, T. W. (2006). On the effect of temperature and strain-rate dependent viscosity on global mantle flow, net rotation, and plate-driving forces. *Geophys. J. Int.*, 167(2), 943–957.

Bentley, M. J., Cofaigh, C., Anderson, J. B., Conway, H., Davies, B., Graham, A. G., ... Zwartz, D. (2014). A community-based geological reconstruction of Antarctic Ice Sheet deglaciation since the Last Glacial Maximum. *Quatern. Sci. Rev.*, 100, 1 - 9. doi: 10.1016/j.quascirev.2014.06.025

Berckhemer, H., Kampfmann, W., Aulbach, E., & Schmeling, H. (1982). Shear modulus and Q of forsterite and dunite near partial melting from forced-oscillation experiments. *Phys. Earth Planet. Interiors*, 29(1), 30 - 41. doi: 10.1016/0031-9201(82)90135-2

Bercovici, D., Schubert, G., & Ricard, Y. (2015). Abrupt tectonics and rapid slab detachment with grain damage. *Proceedings of the National Academy of Sciences*, 112(5), 1287–1291. doi: 10.1073/pnas.1415473112

Bevis, M., Kendrick, E., Smalley Jr., R., Dalziel, I., Caccamise, D., Sasgen, I., ... Konfal, S. (2009). Geodetic measurements of vertical crustal velocity in West Antarctica and the implications for ice mass balance. *Geochemistry, Geophysics, Geosystems*, 10(10). doi: 10.1029/2009GC002642

Bouman, J., Fuchs, M., Ivins, E. R., Van der Wal, W., Schrama, E., Visser, P., & Horwath, M. (2014). Antarctic outlet glacier mass change resolved at basin scale from satellite gravity gradiometry. *Geophys. Res. Lett.*, 41, 5919–5926. doi: 10.1002/2014GL060637

Bradley, S. L., Hindmarsh, R. C., Whitehouse, P. L., Bentley, M. J., & King, M. A. (2015). Low post-glacial rebound rates in the Weddell Sea due to Late Holocene ice-sheet readvance. *Earth Planet. Sci. Lett.*, 413, 79 - 89. doi: 10.1016/j.epsl.2014.12.039

Caron, L., & Ivins, E. R. (2020). A baseline Antarctic GIA correction for space gravimetry. *Earth Planet. Sci. Lett.*, 531, 115957. doi: 10.1016/j.epsl.2019.115957

Caron, L., Ivins, E. R., Larour, E., Adhikari, S., Nilsson, J., & Blewitt, G. (2018). GIA model statistics for GRACE hydrology, cryosphere, and ocean science. *Geophys. Res. Lett.*, 45(5), 2203-2212. doi: 10.1002/2017GL076644

Chatzaras, V., Kruckenberg, S. C., Cohen, S. M., Medaris Jr., L. G., Withers, A. C., & Bagley, B. (2016). Axial-type olivine crystallographic preferred orientations: The effect of

strain geometry on mantle texture. *J. Geophys. Res. Solid Earth*, 121(7), 4895–4922. doi: 10.1002/2015JB012628

Chopelas, A., & Boehler, R. (1992). Thermal expansivity in the lower mantle. *Geophys. Res. Lett.*, 19(19), 1983–1986. doi: 10.1029/92GL02144

Cline II, C. J., Faul, U. H., David, E. C., Berry, A. J., & Jackson, I. (2018). Redox-influenced seismic properties of upper-mantle olivine. *Nature*, 555, 355–358.

Crawford, O., Al-Attar, D., Tromp, J., Mitrovica, J. X., Austermann, J., & Lau, H. C. P. (2018). Quantifying the sensitivity of post-glacial sea level change to laterally varying viscosity. *Geophys. J. Int.*, 214(2), 1324–1363. doi: 10.1093/gji/ggy184

Cressler, J. M., & Moen, K. A. (2012). Physics of temperature and temperature's role in carrier transport. In J. M. Cressler & H. A. Mantooth (Eds.), *Extreme Environments Electronics* (pp. 61–70). CRC Press.

Crittenden, M. J. (1963). New data on the isostatic deformation of Lake Bonneville. In *US Geol. Survey Prof. Paper 454-E* (pp. 1–33). U.S. Geol. Survey.

Dal Forno, G., Gasperini, P., & Boschi, E. (2005). Linear or nonlinear rheology in the mantle: a 3D finite-element approach to postglacial rebound modeling. *Journal of Geodynamics*, 39, 183–195. doi: 10.1016/j.jog.2004.08.008

Danesi, S., & Morelli, A. (2001). Structure of the upper mantle under the antarctic plate from surface wave tomography. *Geophys. Res. Lett.*, 28(23), 4395–4398. doi: 10.1029/2001GL013431

Dannberg, J., Eilon, Z., Faul, U., Gassmöller, R., Moulik, P., & Myhill, R. (2017). The importance of grain size to mantle dynamics and seismological observations. *Geochemistry, Geophysics, Geosystems*, 18(8), 3034–3061.

Davies, D. R., Goes, S., Davies, J. H., Schuberth, B., Bunge, H.-P., & Ritsema, J. (2012). Reconciling dynamic and seismic models of Earth's lower mantle: The dominant role of thermal heterogeneity. *Earth Planet. Sci. Lett.*, 353, 253–269.

Dietrich, R., Rülke, A., Ihde, J., Lindner, K., Miller, H., Niemeier, W., ... Seeber, G. (2004). Plate kinematics and deformation status of the Antarctic Peninsula based on GPS. *Global and Planetary Change*, 42, 313–321. doi: 10.1016/j.gloplacha.2003.12.003

Dimanov, A., Dresen, G., Xiao, X., & Wirth, R. (1999). Grain boundary diffusion creep of synthetic anorthite aggregates: The effect of water. *J. Geophys. Res. Solid Earth*, 104(B5), 10483–10497.

Dixon, N. A., & Durham, W. B. (2018). Measurement of activation volume for creep of dry olivine at upper-mantle conditions. *J. Geophys. Res. Solid Earth*, 123(10), 8459–8473. doi: 10.1029/2018JB015853

Dobslaw, H., Dill, R., Bagge, M., Kleemann, V., Boergens, E., Thomas, M., ... Flechtner, F. (2020). Gravitationally consistent mean barystatic sea level rise from leakage-corrected

monthly grace data. *J. Geophys. Res. Solid Earth*, 125(11), e2020JB020923. doi: 10.1029/2020JB020923

Doubrovine, P. V., Steinberger, B., & Torsvik, T. H. (2012). Absolute plate motions in a reference frame defined by moving hot spots in the Pacific, Atlantic, and Indian oceans. *J. Geophys. Res. Solid Earth*, 117(B9). doi: 10.1029/2011JB009072

Durek, J. J., & Ekström, G. (1996). A radial model of anelasticity consistent with long-period surface-wave attenuation. *Bull. Seismo. Soc. Am.*, 86, 144–158.

Durney, B. (1968). Convective spherical shell: I. No rotation. *J. Atmos. Science*, 25, 372–380. Dziewonski, A. M., Forte, A. M., Su, W., & Woodward, R. L. (1993). Seismic tomography and geodynamics. In K. Aki & R. Dmowska (Eds.), *Relating Geophysical Structures and Processes: The Jeffreys Volume*, *Geophysical Monograph* 76 (p. 67–105). AGU. doi: 10.1029/GM076p0067

Faul, U., & Jackson, I. (2015). Transient creep and strain energy dissipation: An experimental perspective. *Ann. Rev. Earth Planet. Sci.*, 43, 541–569.

Fei, H., Wiedenbeck, M., Yamazaki, D., & Katsura, T. (2013). Small effect of water on upper-mantle rheology based on silicon self-diffusion coefficients. *Nature*, 498(7453), 213–215.

Fei, H., Yamazaki, D., Sakurai, M., Miyajima, N., Ohfuchi, H., Katsura, T., & Yamamoto, T. (2017). A nearly water-saturated mantle transition zone inferred from mineral viscosity. *Science Advances*, 3(6). doi: 10.1126/sciadv.1603024

French, S., Lekić, V., & Romanowicz, B. (2013). Waveform tomography reveals channeled flow at the base of the oceanic asthenosphere. *Science*, 342(6155), 227–230. doi: 10.1126/science.1241514

Gasperini, P., Dal Forno, G., & Boschi, E. (2004). Linear or non-linear rheology in the Earth's mantle: the prevalence of power-law creep in the postglacial isostatic readjustment of Laurentia. *Geophys. J. Int.*, 157(3), 1297–1302. doi: 10.1111/j.1365-246X.2004.02319.x

Goes, S., Govers, R., & Vacher, P. (2000). Shallow mantle temperatures under Europe from P and S wave tomography. *J. Geophys. Res. Solid Earth*, 105(B5), 11153–11169.

Gomez, N., Latychev, K., & Pollard, D. (2018). A coupled ice sheet-sea level model incorporating 3D Earth structure: Variations in Antarctica during the Last deglacial retreat. *Journal of Climate*, 31, 4041 - 4054. doi: 10.1175/JCLI-D-17-0352.1

Gribb, T. T., & Cooper, R. F. (1998). Low-frequency shear attenuation in polycrystalline olivine: Grain boundary diffusion and the physical significance of the Andrade model for viscoelastic rheology. *J. Geophys. Res. Solid Earth*, 103(B11), 27267–27279. doi: 10.1029/98JB02786

Groh, A., Ewert, H., Scheinert, M., Fritsche, M., Rülke, A., Richter, A., ... Dietrich, R. (2012). An investigation of glacial isostatic adjustment over the Amundsen Sea sector, West

Antarctica. *Global and Planetary Change*, 98-99, 45 - 53. doi: 10.1016/j.gloplacha.2012.08.001

Guerri, M., Cammarano, F., & Tackley, P. (2016). Modelling Earth's surface topography: Decomposition of the static and dynamic components. *Phys. Earth Planet. Interiors*, 261, 172 - 186. doi: 10.1016/j.pepi.2016.10.009

Hansen, L., Zimmerman, M. E., & Kohlstedt, D. L. (2011). Grain boundary sliding in San Carlos olivine: Flow law parameters and crystallographic-preferred orientation. *J. Geophys. Res. Solid Earth*, 116(B8).

Hansen, L. N., Zimmerman, M. E., & Kohlstedt, D. L. (2012). The influence of microstructure on deformation of olivine in the grain-boundary sliding regime. *J. Geophys. Res. Solid Earth*, 117(B9). doi: 10.1029/2012JB009305

Hanson, D. R., & Spetzler, H. A. (1994). Transient creep in natural and synthetic, iron-bearing olivine single crystals: Mechanical results and dislocation microstructures. *Tectonophysics*, 235(4), 293 - 315. doi: 10.1016/0040-1951(94)90191-0

Hay, C. C., Lau, H. C. P., Gomez, N., Austermann, J., Powell, E., Mitrovica, J. X., ... Wiens, D. A. (2017). Sea level fingerprints in a region of complex Earth structure: The case of WAIS. *Journal of Climate*, 30(6), 1881 - 1892. doi: 10.1175/JCLI-D-16-0388.1

Hirth, G., & Kohlstedt, D. (2004). Rheology of the upper mantle. In J. Eiler (Ed.), *Inside the Subduction Factory and the Mantle Wedge: A View From the Experimentalists*, *Geophys. Monogr. Ser* (Vol. 138, pp. 83–106). AGU.

Hirth, G., & Kohlstedt, D. L. (1996). Water in the oceanic upper mantle: implications for rheology, melt extraction and the evolution of the lithosphere. *Earth Planet. Sci. Lett.*, 144(1), 93–108. doi: 10.1016/0012-821X(96)00154-9

Hu, Y., & Freymueller, J. T. (2019). Geodetic observations of time-variable glacial isostatic adjustment in southeast Alaska and its implications for Earth rheology. *J. Geophys. Res. Solid Earth*, 124(9), 9870-9889. doi: 10.1029/2018JB017028

Huang, P., Wu, P., & Steffen, H. (2019). In search of an ice history that is consistent with composite rheology in Glacial Isostatic Adjustment modelling. *Earth Planet. Sci. Lett.*, 517, 26 - 37. doi: 10.1016/j.epsl.2019.04.011

Isaak, D. G., Anderson, O. L., & Cohen, R. E. (1992). The relationship between shear and compressional velocities at high pressures: reconciliation of seismic tomography and mineral physics. *Geophys. Res. Lett.*, 19(8), 741–744.

Ivins, E. R. (1989). New aspects of rotational dynamics within the North American-Pacific ductile shear zone. In J. Hillhouse (Ed.), *Deep Structure and Past Kinematics of Accreted Terranes*, *AGU Monograph Series* (Vol. 50, p. 179-201). AGU. doi: 10.1029/GM050p0179

Ivins, E. R., Caron, L., Adhikari, S., Larour, E., & Scheinert, M. (2020). A linear viscoelasticity for decadal to centennial time scale mantle deformation. *Reports on Progress in Physics*, 83. (106801) doi: 10.1088/1361-6633/aba346

Ivins, E. R., James, T. S., & Klemann, V. (2003). Glacial isostatic stress shadowing by the Antarctic ice sheet. *J. Geophys. Res. Solid Earth*, 108(B12). doi: 10.1029/2002JB002182

Ivins, E. R., James, T. S., Wahr, J., O. Schrama, E. J., Landerer, F. W., & Simon, K. M. (2013). Antarctic contribution to sea level rise observed by GRACE with improved GIA correction. *J. Geophys. Res. Solid Earth*, 118(6), 3126–3141. doi: 10.1002/jgrb.50208

Ivins, E. R., Raymond, C. A., & James, T. S. (2000). The influence of 5000 year-old and younger glacial mass variability on present-day crustal rebound in the Antarctic Peninsula. *Earth, Planets & Space*, 152(11), 1023–1029. doi: 10.1186/BF03352325

Ivins, E. R., & Sammis, C. G. (1995). On lateral viscosity contrast in the mantle and the rheology of low-frequency geodynamics. *Geophys. J. Int.*, 123, 305–322.

Ivins, E. R., Unti, T. W. J., & Phillips, R. J. (1982). Large Prandtl number finite-amplitude thermal convection with Maxwell viscoelasticity. *Geophysical & Astrophysical Fluid Dynamics*, 22, 103–132. doi: 10.1080/03091928208221739

Ivins, E. R., Watkins, M. M., Yuan, D.-N., Dietrich, R., Casassa, G., & Rülke, A. (2011). On-land ice loss and glacial isostatic adjustment at the Drake Passage: 2003–2009. *J. Geophys. Res. Solid Earth*, 116. doi: 10.1029/2010JB007607

Jackson, I. (2000). Laboratory measurement of seismic wave dispersion and attenuation: recent progress. In S. I. Karato, A. Forte, R. Liebermann, G. Masters, & L. Stixrude (Eds.), *Earth's deep interior: Mineral physics and tomography from the atomic to the global scale*, AGU Monograph Series (Vol. 117, pp. 265–289). Washington, DC: AGU.

Jackson, I. (2019). Viscoelastic behaviour from complementary forced-oscillation and microcreep tests. *Minerals*, 9(721). doi: 10.3390/min9120721

Jackson, I., & Faul, U. H. (2010). Grainsize-sensitive viscoelastic relaxation in olivine: Towards a robust laboratory-based model for seismological application. *Phys. Earth Planet. Interiors*, 183(1-2), 151–163.

Jackson, I., Faul, U. H., Fitz Gerald, J. D., & Tan, B. H. (2004). Shear wave attenuation and dispersion in melt-bearing olivine polycrystals: 1. specimen fabrication and mechanical testing. *J. Geophys. Res. Solid Earth*, 109(B6). doi: 10.1029/2003JB002406

Jackson, I., Faul, U. H., & Skelton, R. (2014). Elastically accommodated grain-boundary sliding: New insights from experiment and modeling. *Phys. Earth Planet. Interiors*, 228, 203–210.

Jackson, I., Fitz Gerald, J. D., Faul, U. H., & Tan, B. H. (2002). Grain-size-sensitive seismic wave attenuation in polycrystalline olivine. *J. Geophys. Res. Solid Earth*, 107(B12), ECV 5-1-ECV 5-16. doi: 10.1029/2001JB001225

Jain, C., Korenaga, J., & Karato, S.-i. (2019). Global analysis of experimental data on the rheology of olivine aggregates. *J. Geophys. Res. Solid Earth*, 124(1), 310–334.

James, T. S., & Ivins, E. R. (1995). Present-day Antarctic ice mass changes and crustal motion. *Geophys. Res. Lett.*, 22(8), 973–976. doi: 10.1029/94GL02800

Jaupart, C., Labrosse, S., Lucaleau, F., & Mareschal, J.-C. (2015). Temperatures, heat, and energy in the mantle of the Earth. In G. Schubert (Ed.), *Treatise on geophysics* (Second Edition ed., p. 223-270). Oxford: Elsevier.

Johanesen, K. E., & Platt, J. P. (2015). Rheology, microstructure, and fabric in a large scale mantle shear zone, Ronda Peridotite, southern Spain. *Journal of Structural Geology*, 73, 1–17.

Johnson, J. S., Roberts, S. J., Rood, D. H., Pollard, D., Schaefer, J. M., Whitehouse, P. L., ... Smith, J. A. (2020). Deglaciation of Pope Glacier implies widespread early Holocene ice sheet thinning in the Amundsen Sea sector of Antarctica. *Earth Planet. Sci. Lett.*, 548, 116501. doi: 10.1016/j.epsl.2020.116501

Jordan, T. (1981). Continents as a chemical boundary layer. *Phil. Trans. Roy. Soc. London. A, Math. Phys. Sci.*, 301, 359–373. doi: 10.1098/rsta.1981.0117

Jordan, T., Riley, T., & Siddoway, C. (2020). The geological history and evolution of West Antarctica. *Nature Rev. Earth. Environ.*, 1, 117–133. doi: 10.1038/s43017-019-0013-6

Kachuck, S. B., Martin, D. F., Bassis, J. N., & Price, S. F. (2020). Rapid viscoelastic deformation slows marine ice sheet instability at Pine Island Glacier. *Geophys. Res. Lett.*, 47, e2019GL086446. doi: 10.1029/2019GL086446

Kameyama, M., Yuen, D. A., & Karato, S. (1999). Thermal-mechanical effects of low-temperature plasticity (the Peierls mechanism) on the deformation of a viscoelastic shear zone. *Earth Planet. Sci. Lett.*, 168(1–2), 159–172. doi: 10.1016/S0012-821X(99)00040-0

Karato, S.-I. (1993). Importance of anelasticity in the interpretation of seismic tomography. *Geophys. Res. Lett.*, 20(15), 1623–1626.

Karato, S.-I. (2003). Mapping water content in the mantle. *Geophysical Monograph*, 138, 135–152.

Karato, S.-I. (2008). *Deformation of Earth Materials: An Introduction to the Rheology of Solid Earth*. Cambridge University Press.

Karato, S.-I. (2010). Rheology of the Earth's mantle: A historical review. *Gondwana Research*, 18(1), 17–45.

Karato, S.-I., & Karki, B. (2001). Origin of lateral variation of seismic wave velocities and density in the deep mantle. *J. Geophys. Res. Solid Earth*, 106(B10), 21,771–21,783.

Karato, S.-I., Paterson, M. S., & FitzGerald, J. D. (1986). Rheology of synthetic olivine aggregates: Influence of grain size and water. *J. Geophys. Res. Solid Earth*, 91, 8151–8176. doi: 10.1029/JB091iB08p08151

Karato, S.-I., & Spetzler, H. (1990). Defect microdynamics in minerals and solid-state mechanisms of seismic wave attenuation and velocity dispersion in the mantle. *Reviews of Geophysics*, 28(4), 399–421.

Karato, S.-I., & Wu, P. (1993). Rheology of the upper mantle: A synthesis. *Science*, 260(5109), 771–778.

Katsura, T., Yoneda, A., Yamazaki, D., Yoshino, T., & Ito, E. (2010). Adiabatic temperature profile in the mantle. *Phys. Earth Planet. Interiors*, 183(1), 212 - 218. doi: 10.1016/j.pepi.2010.07.001

Kaufmann, G., Wu, P., & Ivins, E. R. (2005). Lateral viscosity variations beneath Antarctica and their implications on regional rebound motions and seismotectonics. *Journal of Geodynamics*, 39(2), 165–181.

Kawazoe, T., Nishihara, Y., Ohuchi, T., Miyajima, N., Maruyama, G., Higo, Y., ... Irifune, T. (2016). Creep strength of ringwoodite measured at pressure-temperature conditions of the lower part of the mantle transition zone using a deformation-DIA apparatus. *Earth Planet. Sci. Lett.*, 454, 10 - 19. doi: 10.1016/j.epsl.2016.08.011

Kittel, C. (2004). *Introduction to Solid State Physics*, 8th Edition. Wylie.

Klemann, V., Ivins, E. R., Martinec, Z., & Wolf, D. (2007). Models of active glacial isostasy roofing warm subduction: Case of the South Patagonian Ice Field. *J. Geophys. Res. Solid Earth*, 112(B9). doi: 10.1029/2006JB004818

Klemann, V., & Wolf, D. (2005). The eustatic reduction of shoreline diagrams: implications for the inference of relaxation-rate spectra and the viscosity stratification below Fennoscandia. *Geophys. J. Int.*, 162, 249-256. doi: 10.1111/j.1365-246X.2005.02637.x

Knopoff, L., & Vane, G. (1978). Age of East Antarctica from surface wave dispersion. *Pure Appl. Geophys.*, 117, 806–815. doi: 10.1007/BF00879981

Kohlstedt, D. L. (2007). Properties of rocks and minerals-constitutive equations, rheological behavior, and viscosity of rocks. In *Treatise on Geophysics* (pp. 389–417). Elsevier.

Kohlstedt, D. L., & Hansen, L. N. (2015). Constitutive equations, rheological behavior, and viscosity of rocks. In G. Schubert (Ed.), *Treatise on Geophysics (Second Edition) Vol. 2* (p. 441 - 472). Oxford: Elsevier.

Kuchar, J., Milne, G., Hill, A., Tarasov, L., & Nordman, M. (2019). An investigation into the sensitivity of postglacial decay times to uncertainty in the adopted ice history. *Geophys. J. Int.*, 220(2), 1172–1186. doi: 10.1093/gji/ggz512

Kumazawa, M., & Anderson, O. L. (1969). Elastic moduli, pressure derivatives, and temperature derivatives of single-crystal olivine and single-crystal forsterite. *J. Geophys. Res.*, 74(25), 5961-5972. doi: 10.1029/JB074i025p05961

Kustowski, B., Ekstrom, G., & Dziewonski, A. M. (2008). Anisotropic shear-wave velocity structure of the Earth's mantle: A global model. *J. Geophys. Res. Solid Earth*, 113(B6). doi: 10.1029/2007JB005169

Kyle, P. (1990). McMurdo Volcanic Group – Western Ross Embayment: Introduction. In W. LeMasurier & J. Thomson (Eds.), *Volcanoes of the Antarctic Plate and Southern Oceans. Antarctic Research Series* (Vol. 48, p. 19-25). American Geophysical Union, Washington, D.C.

Lambeck, K., Rouby, H., Purcell, A., Sun, Y., & Cambridge, M. (2014). Sea level and global ice volumes from the Last Glacial Maximum to the Holocene. *Proceedings of the National Academy of Sciences*, 111(43), 15296–15303. doi: 10.1073/pnas.1411762111

Latychev, K., Mitrovica, J. X., Tromp, J., Tamisiea, M. E., Komatitsch, D., & Christara, C. C. (2005). Glacial isostatic adjustment on 3-D Earth models: a finite-volume formulation. *Geophys. J. Int.*, 161(2), 421-444. doi: 10.1111/j.1365-246X.2005.02536.x

Lau, H. C. P., Austermann, J., Mitrovica, J. X., Crawford, O., Al-Attar, D., & Latychev, K. (2018). Inferences of mantle viscosity based on ice age data sets: The bias in radial viscosity profiles due to the neglect of laterally heterogeneous viscosity structure. *J. Geophys. Res. Solid Earth*, 123(9), 7237–7252. doi: 10.1029/2018JB015740

Lau, H. C. P., & Holtzman, B. K. (2019). “Measures of dissipation in viscoelastic media” extended: Toward continuous characterization across very broad geophysical time scales. *Geophys. Res. Lett.*, 46(16), 9544–9553. doi: 10.1029/2019GL083529

Lawrence, J. F., & Prieto, G. A. (2011). Attenuation tomography of the western United States from ambient seismic noise. *J. Geophys. Res. Solid Earth*, 116(B6). doi: 10.1029/2010JB007836

Lawrence, J. F., & Wysession, M. E. (2006). QLM9: A new radial quality factor (Q_μ) model for the lower mantle. *Earth Planet. Sci. Lett.*, 241(3), 962 – 971. doi: 10.1016/j.epsl.2005.10.030

Lawver, L., Keller, R., Fisk, M., & Strelin, J. (1995). Bransfield Strait, Antarctic Peninsula active extension behind a dead arc. In B. Taylor (Ed.), *Backarc basins*. Elsevier. doi: 10.1007/978-1-4615-1843-3_8

Lee, C.-T. (2003). Compositional variation of density and seismic velocities in natural peridotites at STP conditions: Implications for seismic imaging of compositional heterogeneities in the upper mantle. *J. Geophys. Res.*, 108. (2441) doi: 10.1029/2003JB002413

Lidberg, M., Johansson, J. M., Scherneck, H.-G., & Milne, G. A. (2010). Recent results based on continuous GPS observations of the GIA process in Fennoscandia from BIFROST. *Journal of Geodynamics*, 50(1), 8 - 18. doi: 10.1016/j.jog.2009.11.010

Lloyd, A. J., Wiens, D. A., Zhu, H., Tromp, J., Nyblade, A. A., Aster, R. C., ... O'Donnell, J. P. (2020). Seismic structure of the Antarctic upper mantle imaged with adjoint tomography. *J. Geophys. Res. Solid Earth*, 125(3). doi: 10.1029/2019JB017823

Lucas, E. M., Soto, D., Nyblade, A. A., Lloyd, A. J., Aster, R. C., Wiens, D. A., ... Huerta, A. D. (2020). P- and S-wave velocity structure of central West Antarctica: Implications for the tectonic evolution of the West Antarctic Rift System. *Earth Planet. Sci. Lett.*, 546, 116437. doi: 10.1016/j.epsl.2020.116437

Mackwell, S. J., Kohlstedt, D. L., & Paterson, M. S. (1985). The role of water in the deformation of olivine single crystals. *J. Geophys. Res. Solid Earth*, 90(B13), 11319-11333. doi: 10.1029/JB090iB13p11319

Marquardt, K., & Faul, U. (2018). The structure and composition of olivine grain boundaries: 40 years of studies, status and current developments. *Phys. Chem Minerals*, 45, 139–172. doi: 10.1007/s00269-017-0935-9

Martinec, Z. (2000). Spectral-finite element approach to three-dimensional viscoelastic relaxation in a spherical Earth. *Geophys. J. Int.*, 142(1), 117-141. doi: 10.1046/j.1365-246x.2000.00138.x

Martos, Y. M., Catalán, M., Jordan, T. A., Golynsky, A., Golynsky, D., Eagles, G., & Vaughan, D. G. (2017). Heat flux distribution of Antarctica unveiled. *Geophys. Res. Lett.*, 44(22), 11,417-11,426. doi: 10.1002/2017GL075609

Masuti, S., ichiro Karato, S., Girard, J., & Barbot, S. D. (2019). Anisotropic high-temperature creep in hydrous olivine single crystals and its geodynamic implications. *Phys. Earth Planet. Interiors*, 290, 1 - 9. doi: 10.1016/j.pepi.2019.03.002

Matsyuk, S., Langer, K., & Hösch, A. (1998). Hydroxyl defects in garnets from mantle xenoliths in kimberlites of the Siberian platform. *Contributions to Mineralogy and Petrology*, 132, 163-179. doi: 10.1007/s004100050414

McCarthy, C., Takei, Y., & Hiraga, T. (2011). Experimental study of attenuation and dispersion over a broad frequency range: 2. the universal scaling of polycrystalline materials. *J. Geophys. Res. Solid Earth*, 116(B9). doi: 10.1029/2011JB008384

McKenzie, D., Jackson, J., & Priestley, K. (2005). Thermal structure of oceanic and continental lithosphere. *Earth Planet. Sci. Lett.*, 233(3), 337 - 349. doi: 10.1016/j.epsl.2005.02.005

Mei, S., & Kohlstedt, D. L. (2000). Influence of water on plastic deformation of olivine aggregates: 2. dislocation creep regime. *J. Geophys. Res. Solid Earth*, 105(B9), 21471-21481. doi: 10.1029/2000JB900180

Milne, G. A., Mitrovica, J. X., Scherneck, H.-G., Davis, J. L., Johansson, J. M., Koivula, H., & Vermeer, M. (2004). Continuous GPS measurements of postglacial adjustment in Fennoscandia: 2. Modeling results. *J. Geophys. Res. Solid Earth*, 109(B2). doi: 10.1029/2003JB002619

Minster, J. B., & Anderson, D. L. (1980). Dislocations and nonelastic processes in the mantle. *J. Geophys. Res. Solid Earth*, 85(B11), 6347-6352. doi: 10.1029/JB085iB11p06347

Mitrovica, J. X. (1996). Haskell [1935] revisited. *J. Geophys. Res. Solid Earth*, 101(B1), 555-569. doi: 10.1029/95JB03208

Nichols, K. A., Goehring, B. M., Balco, G., Johnson, J. S., Hein, A. S., & Todd, C. (2019). New Last Glacial Maximum ice thickness constraints for the Weddell Sea Embayment, Antarctica. *The Cryosphere*, 13(11), 2935–2951. doi: 10.5194/tc-13-2935-2019

Nield, G. A., Barletta, V. R., Bordoni, A., King, M. A., Whitehouse, P. L., Clarke, P. J., ... Berthier, E. (2014). Rapid bedrock uplift in the Antarctic Peninsula explained by viscoelastic response to recent ice unloading. *Earth Planet. Sci. Lett.*, 397, 32 - 41.

Nield, G. A., Whitehouse, P. L., King, M. A., & Clarke, P. J. (2016). Glacial isostatic adjustment in response to changing Late Holocene behaviour of ice streams on the Siple Coast, West Antarctica. *Geophys. J. Int.*, 205(1), 1-21. doi: 10.1093/gji/ggv532

Nield, G. A., Whitehouse, P. L., van der Wal, W., Blank, B., O'Donnell, J. P., & Stuart, G. W. (2018). The impact of lateral variations in lithospheric thickness on glacial isostatic adjustment in West Antarctica. *Geophys. J. Int.*, 214(2), 811-824. doi: 10.1093/gji/ggy158

Nordman, M., Milne, G., & Tarasov, L. (2015). Reappraisal of the Ångerman River decay time estimate and its application to determine uncertainty in Earth viscosity structure. *Geophys. J. Int.*, 201(2), 811-822. doi: 10.1093/gji/ggv051

Núñez-Valdez, M., Wu, Z., Yu, Y. G., & Wentzcovitch, R. M. (2013). Thermal elasticity of $(Fe_xMg_{1-x})_2SiO_4$ olivine and wadsleyite. *Geophys. Res. Lett.*, 40, 290-294. doi: 10.1002/grl.50131

O'Donnell, J., Selway, K., Nyblade, A. A., Brazier, R., Wiens, D., Anandakrishnan, S., ... Winberry, J. (2017). The uppermost mantle seismic velocity and viscosity structure of Central West Antarctica. *Earth Planet. Sci. Lett.*, 472, 38–49.

Pappa, F., Ebbing, J., Ferraccioli, F., & van der Wal, W. (2019). Modeling satellite gravity gradient data to derive density, temperature, and viscosity structure of the Antarctic lithosphere. *J. Geophys. Res. Solid Earth*, 124(11), 12053-12076. doi: 10.1029/2019JB017997

Park, Y., Kim, K.-H., Lee, J., Yoo, H. J., & Plasencia L., M. P. (2012). P-wave velocity structure beneath the northern Antarctic Peninsula: evidence of a steeply subducting slab and a deep-rooted low-velocity anomaly beneath the central Bransfield Basin. *Geophys. J. Int.*, 191(3), 932-938. doi: 10.1111/j.1365-246X.2012.05684.x

Paterson, M., & Olgaard, D. (2000). Rock deformation tests to large shear strains in torsion. *Journal of Structural Geology*, 22(9), 1341 - 1358.

Paulson, A., Zhong, S., & Wahr, J. (2005). Modelling post-glacial rebound with lateral viscosity variations. *Geophys. J. Int.*, 163(1), 357-371. doi: 10.1111/j.1365-246X.2005.02645.x

Peltier, W. R., Wu, P., & Yuen, D. A. (1981). The viscosities of the Earth's mantle. In *Anelasticity in the Earth* (p. 59-77). AGU. doi: 10.1029/GD004p0059

Peltier, W. R., Yuen, D. A., & Wu, P. (1980). Postglacial rebound and transient rheology. *Geophys. Res. Lett.*, 7(10), 733-736. doi: 10.1029/GL007i010p00733

Poirier, J.-P. (2000). *Introduction to the Physics of the Earth's Interior*. Cambridge University Press.

Powell, E., Gomez, N., Hay, C., Latychev, K., & Mitrovica, J. X. (2020). Viscous effects in the solid Earth response to modern Antarctic ice mass flux: Implications for geodetic studies of WAIS stability in a warming world. *Journal of Climate*, 33(2), 443-459. doi: 10.1175/JCLI-D-19-0479.1

Ranalli, G. (2001). Mantle rheology: radial and lateral viscosity variations inferred from microphysical creep laws. *Journal of Geodynamics*, 32(4-5), 425–444.

Ritzwoller, M. H., Shapiro, N. M., Levshin, A. L., & Leahy, G. M. (2001). Crustal and upper mantle structure beneath Antarctica and surrounding oceans. *J. Geophys. Res. Solid Earth*, 106(B12), 30645-30670. doi: doi.org/10.1029/2001JB000179

Sabadini, R., Vermeersen, B., & Cambiotti, G. (2016). *Global Dynamics of the Earth: Applications of Viscoelastic Relaxation Theory to Solid-Earth and Planetary Geophysics*. Springer.

Samrat, N. H., King, M. A., Watson, C., Hooper, A., Chen, X., Barletta, V. R., & Bordoni, A. (2020). Reduced ice mass loss and three-dimensional viscoelastic deformation in northern Antarctic Peninsula inferred from GPS. *Geophys. J. Int.*, 222, 1013-1022. doi: 10.1093/gji/ggaa229

Scheinert, M., Ferraccioli, F., Schwabe, J., Bell, R., Studinger, M., Damaske, D., ... Richter, T. D. (2016). New Antarctic gravity anomaly grid for enhanced geodetic and geophysical studies in Antarctica. *Geophys. Res. Lett.*, 43, 600-610. doi: 10.1002/2015GL067439

Schwarz, R., & Granato, A. (1975). Theory of damping due to thermally assisted unpinning of dislocations. *Physical Review Letters*, 34, 1174–1177.

Shen, W., Wiens, D. A., Anandakrishnan, S., Aster, R. C., Gerstoft, P., Bromirski, P. D., ... Winberry, J. P. (2018). The crust and upper mantle structure of Central and West Antarctica from Bayesian inversion of Rayleigh wave and receiver functions. *J. Geophys. Res. Solid Earth*, 123(9), 7824-7849. doi: 10.1029/2017JB015346

Shimojuku, A., Kubo, T., Ohtani, E., Nakamura, T., Okazaki, R., Dohmen, R., & Chakraborty, S. (2009). Si and O diffusion in (Mg, Fe) 2SiO_4 wadsleyite and ringwoodite and its implications for the rheology of the mantle transition zone. *Earth Planet. Sci. Lett.*, 284(1), 103 - 112. doi: 10.1016/j.epsl.2009.04.014

Sigmundsson, F. (1991). Post-glacial rebound and asthenosphere viscosity in Iceland. *Geophys. Res. Lett.*, 18(6), 1131-1134. doi: 10.1029/91GL01342

Simms, A. R., Ivins, E. R., DeWitt, R., Kouremenos, P., & Simkins, L. M. (2012). Timing of the most recent Neoglacial advance and retreat in the South Shetland Islands, Antarctic Peninsula: insights from raised beaches and Holocene uplift rates. *Quatern. Sci. Rev.*, 47, 41 - 55. doi: 10.1016/j.quascirev.2012.05.013

Smellie, J. L., Panter, K. S., & Geyer, A. (2021). Introduction. In J. L. Smellie, K. S. Panter, & A. Geyer (Eds.), *Volcanism in Antarctica: 200 million years of Subduction, Rifting and Continental Break-up*. (Geological Society, London, Memoir 55) doi: 10.1144/M55-2021-XXX

Spada, G., Colleoni, F., & Ruggieri, G. (2011). Shallow upper mantle rheology and secular ice sheet fluctuations. *Tectonophysics*, 511(3), 89 - 98. doi: 10.1016/j.tecto.2009.12.020

Stacey, F. D., & Davis, P. (2008). *Physics of the Earth*. Cambridge University Press.

Stacey, F. D., & Hodgkinson, J. H. (2019). Thermodynamics with the Grüneisen parameter: Fundamentals and applications to high pressure physics and geophysics. *Phys. Earth Planet. Interiors*, 286, 42 - 68. doi: 10.1016/j.pepi.2018.10.006

Stixrude, L., & Jeanloz, R. (2015). Constraints on seismic models from other disciplines - constraints from mineral physics on seismological models. In G. Schubert (Ed.), *Treatise on Geophysics (2nd Ed.)* (p. 829 - 852). Oxford: Elsevier.

Stixrude, L., & Lithgow-Bertelloni, C. (2010). Thermodynamics of the Earth's mantle. *Rev. Mineral. Geochem.*, 71(1), 465-484. doi: 10.2138/rmg.2010.71.21

Takei, Y., Karasawa, F., & Yamauchi, H. (2014). Temperature, grain size, and chemical controls on polycrystal anelasticity over a broad frequency range extending into the seismic range. *J. Geophys. Res. Solid Earth*, 119, 5414-5443. doi: 10.1002/2014JB011146

Tanaka, Y., Klemann, V., Martinec, Z., & Riva, R. E. M. (2011). Spectral-finite element approach to viscoelastic relaxation in a spherical compressible Earth: application to GIA modelling. *Geophys. J. Int.*, 184, 220-234. doi: 10.1111/j.1365-246X.2010.04854.x

Tromp, J., & Mitrovica, J. X. (2000). Surface loading of a viscoelastic planet, III. Aspherical models. *Geophys. J. Int.*, 140(2), 425-441. doi: 10.1046/j.1365-246x.2000.00027.x

Tushingham, A. M., & Peltier, W. R. (1992). Validation of the ICE-3G model of Würm-Wisconsin deglaciation using a global data base of relative sea level histories. *J. Geophys. Res. Solid Earth*, 97, 3285-3304. doi: 10.1029/91JB02176

Vacher, P., Mocquet, A., & Sotin, C. (1996). Comparison between tomographic structures and models of convection in the upper mantle. *Geophys. J. Int.*, 124, 45-56.

van den Berg, A. P., Yuen, D. A., & van Keeken, P. E. (1995). Rheological transition in mantle convection with a composite temperature-dependent, non-Newtonian and Newtonian rheology. *Earth Planet. Sci. Lett.*, 129(1), 249 - 260. doi: 10.1016/0012-821X(94)00246-U

van der Wal, W., Whitehouse, P. L., & Schrama, E. J. (2015). Effect of GIA models with 3D composite mantle viscosity on GRACE mass balance estimates for Antarctica. *Earth Planet.*

Sci. Lett., 414, 134–143. van der Lee, S. (2001). Deep below North America. *Science*, 294(5545), 1297–1298. doi: 10.1126/science.1066319

van der Wal, W., Barnhoorn, A., Stocchi, P., Gradmann, S., Wu, P., Drury, M., & Vermeersen, B. (2013). Glacial isostatic adjustment model with composite 3-D Earth rheology for Fennoscandia. *Geophys. J. Int.*, 194(1), 61–77.

van der Wal, W., Wu, P., Wang, H., & Sideris, M. G. (2010). Sea levels and uplift rate from composite rheology in glacial isostatic adjustment modeling. *Journal of Geodynamics*, 50(1), 38–48.

Wahr, J., Wingham, D., & Bentley, C. (2000). A method of combining ICESat and GRACE satellite data to constrain Antarctic mass balance. *J. Geophys. Res. Solid Earth*, 105(B7), 16279–16294. doi: 10.1029/2000JB900113

Wang, H., Wu, P., & van der Wal, W. (2008). Using postglacial sea level, crustal velocities and gravity-rate-of-change to constrain the influence of thermal effects on mantle lateral heterogeneities. *Journal of Geodynamics*, 46, 104 - 117.

Wang, L., Blaha, S., Kawazoe, T., Miyajima, N., & Katsura, T. (2017). Identical activation volumes of dislocation mobility in the [100](010) and [001](010) slip systems in natural olivine. *Geophys. Res. Lett.*, 44, 2687-2692. doi: 10.1002/2017GL073070

Whitehouse, P. L. (2018). Glacial isostatic adjustment modelling: historical perspectives, recent advances, and future directions. *Earth Surface Dynamics*, 6(2), 401–429. doi: 10.5194/esurf-6-401-2018

Whitehouse, P. L., Bentley, M. J., Milne, G. A., King, M. A., & Thomas, I. D. (2012). A new glacial isostatic adjustment model for Antarctica: calibrated and tested using observations of relative sea-level change and present-day uplift rates. *Geophys. J. Int.*, 190, 1464–1482.

Whitehouse, P. L., Bentley, M. J., Vieli, A., Jamieson, S. S. R., Hein, A. S., & Sugden, D. E. (2017). Controls on Last Glacial Maximum ice extent in the Weddell Sea embayment, Antarctica. *J. Geophys. Res. Earth Surface*, 122(1), 371-397. doi: 10.1002/2016JF004121

Wiens, D. A., Conder, J. A., & Faul, U. H. (2008). The seismic structure and dynamics of the mantle wedge. *Ann. Rev. Earth Planet. Sci.*, 36(1), 421-455. doi: 10.1146/annurev.earth.33.092203.122633

Wilch, T., McIntosh, W., & Dunbar, N. (1999). Late Quaternary volcanic activity in Marie Byrd Land: Potential $^{40}\text{Ar}/^{39}\text{Ar}$ -dated time horizons in West Antarctic ice and marine cores. *Geol. Soc. Am. Bull.*, 111, 1563–1580.

Wolf, D., Klemann, V., Wünsch, J., & Zhang, F.-P. (2006). A reanalysis and reinterpretation of geodetic and geological evidence of glacial-isostatic adjustment in the Churchill region, Hudson Bay. *Surveys in Geophysics*, 27, 19–61.

Wolstencroft, M., King, M. A., Whitehouse, P. L., Bentley, M. J., Nield, G. A., King, E. C., ... Gunter, B. C. (2015). Uplift rates from a new high-density GPS network in Palmer Land

indicate significant late Holocene ice loss in the southwestern Weddell Sea. *Geophys. J. Int.*, 203, 737-754. doi: 10.1093/gji/ggv327

Wu, P. (1999). Modelling postglacial sea levels with power-law rheology and a realistic ice model in the absence of ambient tectonic stress. *Geophys. J. Int.*, 139(3), 691-702. doi: 10.1046/j.1365-246x.1999.00965.x

Wu, P. (2002). Effects of nonlinear rheology on degree 2 harmonic deformation in a spherical self-gravitating earth. *Geophys. Res. Lett.*, 29, 40-1-4. doi: 10.1029/2001GL014109

Wu, P. (2005). Effects of lateral variations in lithospheric thickness and mantle viscosity on glacially induced surface motion in Laurentia. *Earth Planet. Sci. Lett.*, 235, 549-563. doi: 10.1016/j.epsl.2005.04.038

Wu, P., Wang, H., & Steffen, H. (2013). The role of thermal effect on mantle seismic anomalies under Laurentia and Fennoscandia from observations of Glacial Isostatic Adjustment. *Geophys. J. Int.*, 192, 7–17.

Xu, Z., Schrama, E. J., van der Wal, W., van den Broeke, M., & Enderlin, E. M. (2016). Improved GRACE regional mass balance estimates of the Greenland Ice Sheet cross-validated with the input-output method. *The Cryosphere*, 10(2), 895–912.

Yuen, D. A., Hansen, U., Zhao, W., Vincent, A. P., & Malevsky, A. V. (1993). Hard turbulent thermal convection and thermal evolution of the mantle. *J. Geophys. Res. Planets*, 98, 5355-5373. doi: 10.1029/92JE02725

Zhao, C., King, M. A., Watson, C. S., Barletta, V. R., Bordoni, A., Dell, M., & Whitehouse, P. L. (2017). Rapid ice unloading in the Fleming Glacier region, southern Antarctic Peninsula, and its effect on bedrock uplift rates. *Earth Planet. Sci. Lett.*, 473, 164 - 176.

Zhong, S., Paulson, A., & Wahr, J. (2003). Three-dimensional finite-element modelling of Earth's viscoelastic deformation: effects of lateral variations in lithospheric thickness. *Geophys. J. Int.*, 155, 679-695. doi: 10.1046/j.1365-246X.2003.02084.x

Zhu, T. (2014). Tomography-based mantle flow beneath Mongolia-Baikal area. *Phys. Earth Planet. Interiors*, 237, 40-50. doi: 10.1016/j.pepi.2014.10.003

Figure Captions

Figure 1. Deviation in shear wave velocity from global average at 300 km depth. This is reported as the Voigt average of a transversely anisotropic shear wave solution described by Lloyd et al. (2020) and by Wiens et al., this volume. Also shown are site names referred to throughout the chapter. The locations are: Amundsen Sea Embayment (ASE), Amundsen Sea Sector (ASS), Bransfield Strait (BS), Balleny Trough (BT), central Antarctic Peninsula (cAP), Central Siple Coast (CSC), Graham Land (GL), Kamb Ice Stream (KIS), Marie Byrd Land (MBL), Ross Island (RI), southern Antarctic Peninsula (sAP), Syowa Coast (SC), South Shetland Islands (SSI), Transantarctic Mountains (TAM), Weddell Sea (WS), Weddell Sea Embayment (WSE), Wilkes Subglacial Basin (WSB). Bathymetry is contoured at -500 m, -1000 m, and -2,500 m. White contours show ice topography. Thick white lines show plate boundaries.

Figure 2. Deformation maps of differential stress as a function of grain-size for olivine at a pressure of 7 GPa and temperature of 1700 ° K. In the Earth's convecting mantle, grain-size may be highly variable (Dannberg et al., 2017). Reprinted from Karato (2010), with permission from Elsevier.

Figure 3. Deformation maps of differential stress as a function of temperature for dunite, with a grain sizes of 10 μ m (a) and 1 mm (b). Light contour lines show constant strain rate. GBS = grain boundary sliding. Most observed grain sizes corresponding to the upper mantle are better reflected by frame (b). Modified from Kohlstedt (2007), with permission from Elsevier.

Figure 4. Shear wave velocity in ANT-20 as a deviation from global average (STW105) at (a) 150 and (b) 550 km depth. Note the differences in the color scale bar. Refer to Figure 1 for the place name abbreviations in map (a) and additional information.

Figure 5. $-\log_{10}\Delta\eta$ vs H_D^* at 150 km depth and rheology used in Approach 2. In this example $\delta\ln\nu_S = -0.02$. The red and blue solid lines refer to the geotherms referenced as 'hot' and 'cold' in Table 2. The grey zone (most probable range) assumes $H_D^* = \xi H^*$ with $0.8 \leq \xi \leq 1.0$, the rule of thumb suggested by Karato (2008). The black dashed line shows the result for a value of T_0 that is assumed in this Chapter for all three inter-comparative approaches for $z = 150$ km.

Figure 6. $-\log_{10}\Delta\eta$ vs H_D^* at (a) $z = 150$ km and (b) 300 km depths for Approach 2. The S-wave velocity anomaly is -2%. A full range of possible H_D^* are shown, but the grey area shows the range of values inferred from Jackson and Faul (2010). The black dashed line in (a) and (b) are for our preferred c_1 at 150 and 300 km, respectively. The vertical dashed-double dot line shows activation enthalpy calculated in experiments of Jackson et al. (2014) with an absorption peak centered at a period of 14.1 s and a more nuanced grain-size sensitivity. Parameters are given in Table 4. Approach 2 predictive maps use H_D^* within the grey shaded region.

Figure 7. $-\log_{10}\Delta\eta$ vs H_D^* at $z = 550$ km with differing c_1 at that depth. The S-wave velocity anomaly is -2%. The orange dashed line is our preferred estimate for mapping at 550 km depth. Other parameters are given in Table 4. Note that there are no experimental results on H_D^* for

ringwoodite, so the grey zone (most probable range) assumes $H_D^* = \xi H^*$ with $0.8 \leq \xi \leq 1.0$, as is assumed in Figures 5 and 6. A steady-state creep value is used for H^* for ringwoodite as determined by Fei et al. (2017).

Figure 8. Maps of the $1-\sigma$ uncertainty propagated in estimation of $\log_{10}\eta$ at the depths of (a) 150, (b) 300 and (c) 550 km for Approach 2. Table 4 gives parameter values along with uncertainty estimates. Units are in viscosity deviation from dimensionless $\Delta\log_{10}\eta$. A reduced color threshold scale for frame (c) aids in revealing a different pattern of uncertainty at 550 km.

Figure 9. $\log_{10}\Delta\eta$ vs H_D^* at the depths of 550 km with fit (a) $n = 3$ (fixed) and (b) $n = 2.4$. $H^* = 345$ kJ/mol and our preferred value for anelastically related activation enthalpy is with $\xi = 0.9$, or $H_D^* = 310.5$ kJ/mol in frame (a). For frame (b) $H^* = 279$ kJ/mol and our preferred value at the same $\xi = 0.9$ is $H_D^* = 251.1$ kJ/mol. Other aspects are the same as in Figures 6 and 7.

Figure 10. Maps of $\log_{10}\eta$ at the depth of 150 km for three approaches. Approach 1 assumes $\beta = 1$ and the flow law for dry olivine from Hirth and Kohlstedt (2004) using $E^* = 375$ kJ/mol and $V^* = 5 \times 10^{-6} \text{ m}^3/\text{mol}$. Approach 2 uses parameters as shown in Table 4. Approach 3 assumes diffusion and dislocation activation parameters are taken from Hirth and Kohlstedt (2004) for dry olivine with a grain-size of 4 mm and stress of 0.1 MPa. Composite component GBS parameters for Approach 3 are discussed in the text.

Figure 11. Maps of $\log_{10}\eta$ at the depth of 300 km for three approaches. Parameters are as in Figure 10 with adjustments for temperature and pressure as in Tables 1 and 2, respectively. Note the close, but serendipitous, similarity of the predicted viscosity in frames (a) and (b).

Figure 12. Maps of $\log_{10}\eta$ at the depth of 550 km for three approaches. Viscosity for Approach 1 assumes $\beta = 1$. While assuming differing anelastic corrections, both Approach 1 and 2 use the flow law for hydrous ringwoodite from Fei et al. (2017), with $E^* = 250.4$ kJ/mol and $V^* = 2.6 \times 10^{-6} \text{ m}^3/\text{mol}$. Approach 2 (frame b) uses parameters as shown in Table 4. Approach 3 of frame (c) assumes $A = 10^{-0.2} \text{ s}^{-1} \text{ MPa}^n$ for dislocation creep (Kawazoe et al., 2016) and $A = 10^{-13.2} \text{ s}^{-1} \text{ MPa}^n$ for diffusion in ringwoodite (Shimojuku et al., 2009). The activation enthalpy assumed for dislocation and diffusion creep at 550 km in frame (c) are $H^* = 345$ kJ/mol and $H^* = 402$ kJ/mol, respectively. No GBS is assumed at this depth.

Figure 13. $\log_{10}\Delta\eta$ vs H_D^* at the depth of 150 km. All parameters are as in Figure 6 (a) with values referred to Table 4. Q_s models, one used in ANT-20 is QL6 of Durek and Ekström (1996) and the other QLM9 by Lawrence and Wysession (2006) used in Table 20.2 of Karato (2008). The differences in prediction are small. The dash and dash-dot lines are for $c_1 = 8$ and solid for $c_1 = 9.4$. The full range of H_D^* are explored that are reported in Jackson and Faul (2010). Expansion of the lower range to account for lower H_D^* is inferred from McCarthy et al. (2011) and Jackson et al. (2014).

Figure A1. Test of the linearization of δT as in Equation (8) versus the exact form from Equation (7). For the exact and 2nd order approximation (see Equation A1), the influence of δT is asymmetric with respect to the sign of δT . The green and blue colors indicate negative and positive temperature deviations, respectively. Solid lines indicate no approximation, while light dashed and lines are for second order approximation (only visible for positive δT case and overlap in the case of negative δT). For the orange dash, the linear approximation (1st order) does not exhibit this asymmetry so that $\pm\delta T$ are coincident. We also plot the Latychev et al. (2005) method with the red dotted curve which here overlays the 1st order approximation.

Figure A2. Positions of the thermal model computed in An et al. (2015) superimposed on a color topography map of Antarctica. Figure A1 assumes values of $T_0 + \delta T$ from the model at $z = 240$ km. The temperature contrast retrieved at the positions in the model ($2 \times \delta T$) is $285^\circ K$. Modified from An et al. (2015).

Table Captions

Table 1. Intercomparison of techniques for scaling Antarctic upper mantle $\log_{10}\eta(r, \theta, \phi)^a$.

Table 2. Temperature T_0 assumed at 150, 300 and 550 km depths.

Table 3. Guide for the three inter-comparative Approaches.[†]

Table 4. Parameters for $\log_{10}\Delta\eta$ in Approach 2.

Table 5. Flow parameters used in Approach 3.

Table 6. Viscosity (10^{19} Pa s): Scaling to $\delta\ln\nu_s$ vs modeled GIA with geodetic data support.

| # | rock microphysics | laboratory experiments |
|----------------|--|--|
| | depth of maps: $z = 150^\dagger \text{ & } 300 \text{ km}^\ddagger, z = 550 \text{ km}^\ddagger$ | |
| 1 [†] | diffusion controlled | dry olivine |
| 2 [†] | grain boundary dislocation sliding | dry olivine |
| 3 [†] | multiple microphysics | olivine sliding + dislocation + diffusion |
| 1 [‡] | dislocation controlled | $\sim 1.5\% \text{ H}_2\text{O}$ by weight ringwoodite |
| 2 [‡] | dislocation controlled | $\sim 1.5\% \text{ H}_2\text{O}$ by weight ringwoodite climb & glide dislocation, |
| 3 [‡] | multiple microphysics | $\sim 2.0\% \text{ H}_2\text{O}$ ringwoodite |

^a $T_0(r)$ is common to all three methods.

Table 1

| depth (km) | T_0 ($^{\circ}$ K) | method |
|-------------------------------------|-----------------------|---|
| ^a 150 (hot continental) | 1680 ± 20 | Jaupart et al. (2015) ($q_{\text{GHF}} = 90 \text{m W/m}^2$) ^b |
| ^a 150 (cold continental) | 1283 ± 20 | McKenzie et al. (2005) ($q_{\text{GHF}} = 58.6 \text{m W/m}^2$) |
| 150 (global average) | 1473 ± 40 | Stacey and Davis (2008) |
| 300 | 1722 ± 42 | Katsura et al. (2010) (isentrope varying with depth) |
| 550 | 1930 ± 50 | Katsura et al. (2010) (computed temperature) |

^a Hot and cold values are for illustration and are not used in the computations of viscosity

^b q_{GHF} is the corresponding regional surface geothermal heat flux.

Table 2

| parameter | rule | subcommonality§ |
|----------------------|--------|----------------------|
| $T_0(r)$ | common | 1, 2, & 3 |
| $\frac{dv_s(r)}{dT}$ | differ | 1, 3 |
| $H^*(r)$ | differ | 1, 2 at z = 550 km |
| $\bar{\eta}$ | common | Equations (4) & (14) |
| $\bar{\eta}_0(r)$ ‡ | differ | none |

†Differences in anelastic correction are discussed in the text.

‡See Equation (4). §Numbers refer to Approaches.

Table 3

| z (km) | $\dagger\alpha_{th}$ ($10^{-5^\circ} K^{-1}$) | P (GPa) | $\ddagger c_1$ | E^* (kJ/mol) | $\downarrow V^*$ ($10^{-6} m^3 /mol$) | $\dagger\dagger H_D^*$ (kJ/mol) |
|----------|---|-----------|----------------|------------------|---|---------------------------------|
| 150 | 4.05 ± 0.36 | 4.78 | 9.4 ± 2.4 | $\$444.2 \pm 20$ | $\$18.0$ | 394 ± 45 |
| 300 | 3.02 ± 0.30 | 9.8 | 7.0 ± 2.0 | $\$444.2 \pm 20$ | $\$18.0$ | 394 ± 45 |
| 550 | 2.60 ± 0.26 | 19.1 | 6.5 ± 2.0 | $\P250.4 \pm 30$ | $\P2.6$ | 269 ± 31 |

\ddagger Isaak et al. (1992), O. L. Anderson (1995), \dagger Katsura et al. (2010), $\$$ L. Hansen et al. (2011), \P L. Wang et al. (2017), $\dagger\dagger$ Jackson and Faul (2010), $<$ no error estimates cited in the reports.

Table 4

| depth (km) | $\dagger E_{diff}^*$ (kJ/mol) | $\dagger E_{disc}^*$ (kJ/mol) | $\S E_{GBS}^*$ (kJ/mol) | $\dagger V_{diff}^*$ ($10^{-6} m^3$ /mol) | $\ddagger V_{disc}^*$ ($10^{-6} m^3$ /mol) | $\ddagger V_{GBS}^*$ ($10^{-6} m^3$ /mol) | σ (MPa) |
|---------------|----------------------------------|----------------------------------|----------------------------|---|--|---|-------------------|
| 150 | 375 | 530 | 445 | 5.0 | 3.0 | 12.0 | 0.1 |
| 300 | 375 | 530 | 445 | 5.0 | 3.0 | 3.0 | 0.1 |
| depth (km) | $\P H_{diff}^*$ (kJ/mol) | $\P H_{disc}^*$ (kJ/mol) | σ (MPa) | | | | |
| 550 | 402 | 345 | 0.002 | | | | |

\dagger Hirth and Kohlstedt (2004), \ddagger Kohlstedt and Hansen (2015), \S L. Hansen et al. (2011)

\P Kawazoe et al. (2016). Stress exponents (n) are: olivine dislocation: 3.5 (Hirth & Kohlstedt, 2004), ringwoodite: 3 (Kawazoe et al., 2016), GBS: 2.9 (L. Hansen et al., 2011).

Table 5

| Region § | Approach 1 | Approach 2 | Approach 3 $z = 150 \text{ km}$ | GIA Viscosity | Study† |
|----------------------|------------------|----------------|------------------------------------|------------------------------------|--|
| GL | $\sim 0.6 - 3$ | $\sim 2 - 6$ | $\sim 9 - 20$ | $7 - 9, 0.06 - 0.2, 0.03 -$ 0.3 | I11 ^a , N14 ^b , S20 |
| SSI | $\sim 2 - 6$ | $\sim 3 - 7$ | $\sim 10 - 30$ | $0.1 - 0.2$ | S12 |
| cAP | $\sim 0.6 - 3$ | $\sim 2 - 6$ | $\sim 9 - 20$ | 2 | Z17 |
| sAP | $\sim 6 - 30$ | $\sim 9 - 40$ | $\sim 9 - 40$ | $10 - 30$ | W15 |
| KIS | $\sim 6 - 20$ | $\sim 10 - 30$ | $\sim 40 - 80$ | ≥ 10 | N16 |
| ASE | $\sim 0.6 - 0.9$ | $\sim 1 - 4$ | $\sim 6 - 20$ | $\sim 0.2, 0.4$ | P20, B18 |
| WSE | $\sim 7 - 40$ | $\sim 10 - 50$ | $\sim 100 - 1000$ | $10, 10 - 30$ | B15, W15 |
| WSB | $\sim 20 - 60$ | $\sim 40 - 80$ | $\sim 200 - 2000$ | 40 | A09 |
| $z = 550 \text{ km}$ | | | | | |
| GL | $\sim 20 - 60$ | $\sim 20 - 60$ | $\sim 70 - 100$ | $7 - 9, 40, 40$ | I11, N14, S20 |
| SSI | $\sim 30 - 70$ | $\sim 20 - 60$ | $\sim 40 - 90$ | $0.1 - 0.2$ | S12 |
| cAP | $\sim 30 - 70$ | $\sim 30 - 70$ | $\sim 70 - 100$ | 4 | Z17 |
| sAP | $\sim 40 - 80$ | $\sim 40 - 80$ | $\sim 50 - 90$ | $10 - 30$ | W15 |
| KIS | $\sim 20 - 60$ | $\sim 20 - 60$ | $\sim 20 - 60$ | ≥ 10 | N16 |
| ASE | $\sim 4 - 9$ | $\sim 6 - 20$ | $\sim 4 - 9$ | 1.5 | B18 |
| WSE | $\sim 9 - 70$ | $\sim 8 - 50$ | $\sim 40 - 80$ | $10, 10 - 30$ | B15, W15 |
| WSB | $\sim 5 - 20$ | $\sim 10 - 50$ | $\sim 10 - 50$ | 40 | A09 |

§ Refer to labels on maps of Figure 1 or Figure 4(a).

†Amalvict et al. (2009) (A09), Barletta et al. (2018) (B18), Bradley et al. (2015) (B15), Ivins et al. (2011) (I11), Nield et al. (2014); Nield et al. (2016) (N14), (N16), Powell et al. (2020) (P20), Samrat et al. (2020) (S20), Simms et al. (2012) (S12), Wolstencroft et al. (2015) (W15), Zhao et al. (2017) (Z17).

^aHalf-space mantle with ice loss since 1930.

^bMantle constant to 400 km depth and 20th century mass gain.

Table 6

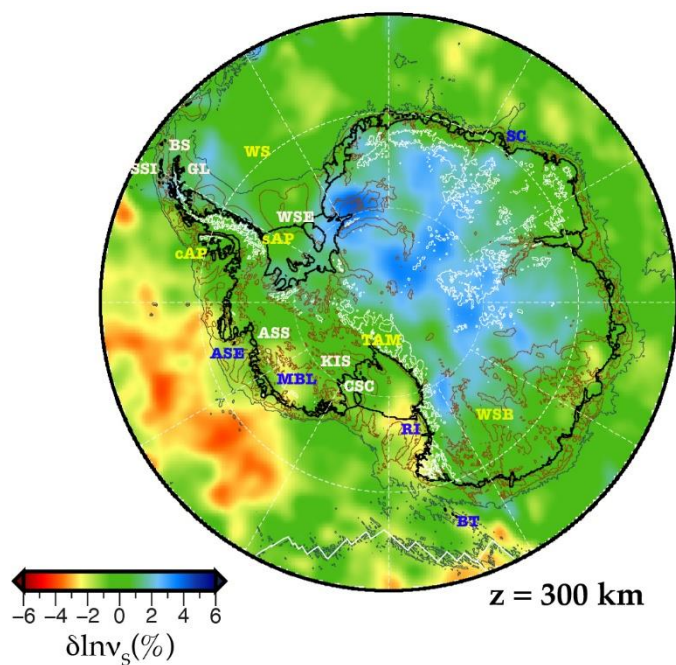


Figure 1

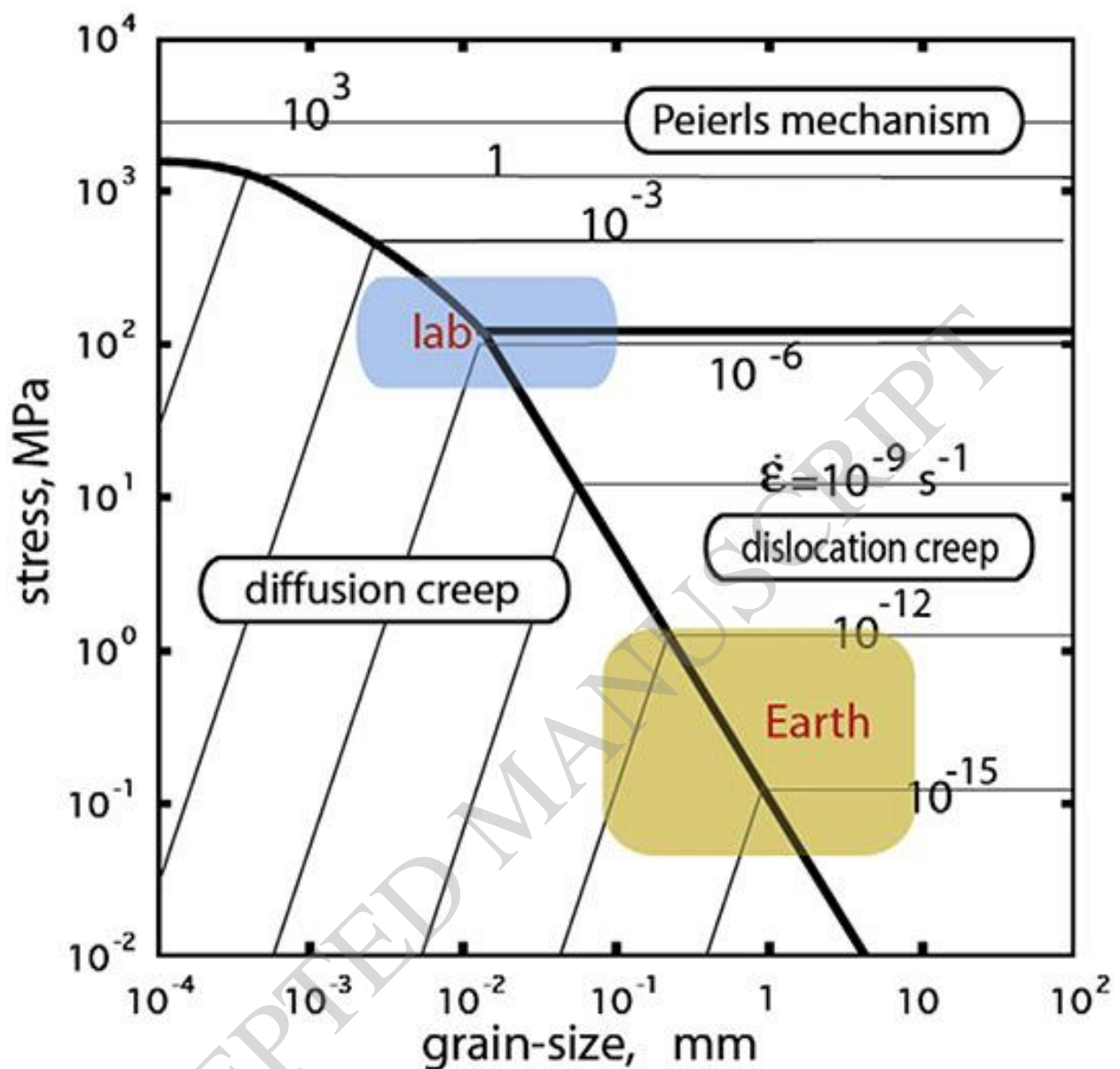


Figure 2

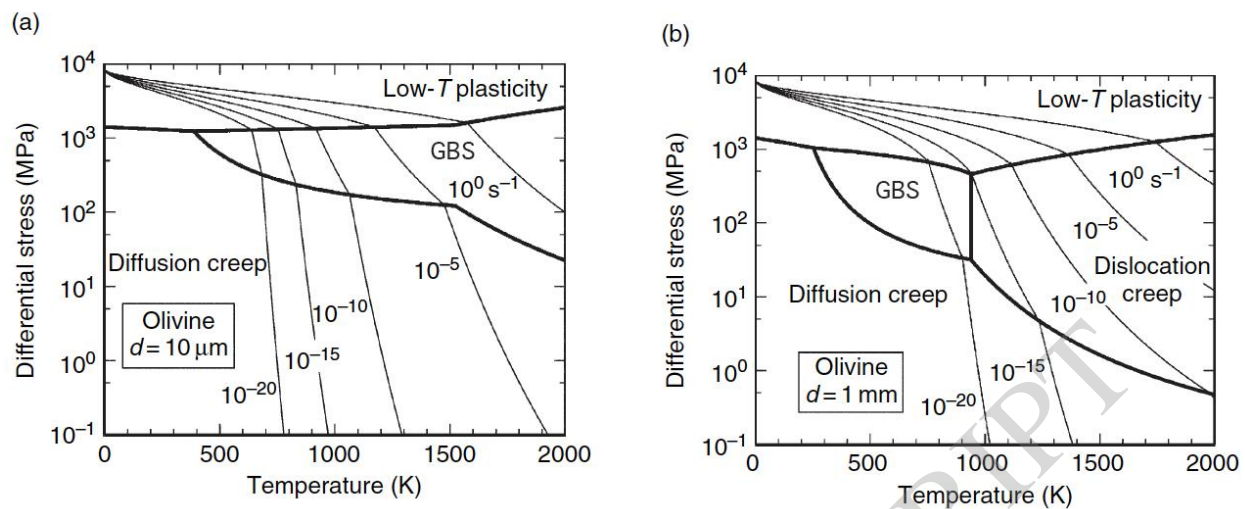


Figure 3

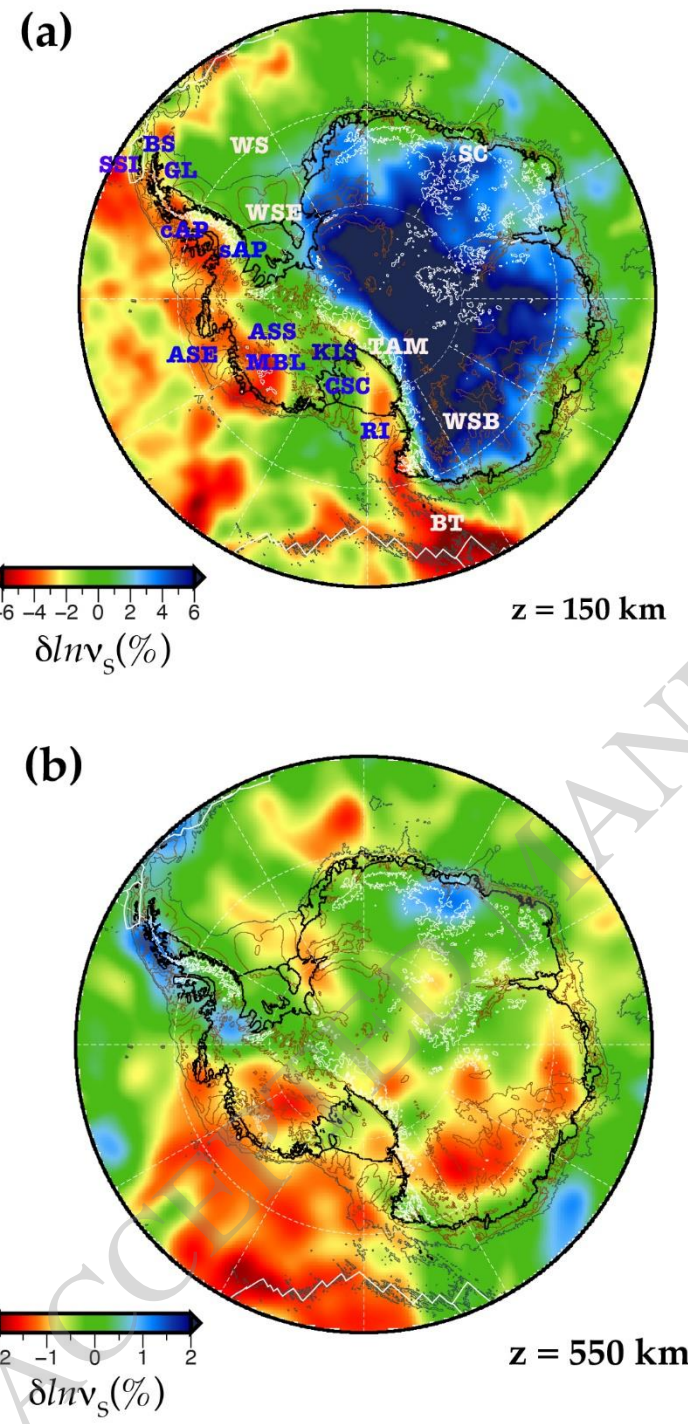


Figure 4

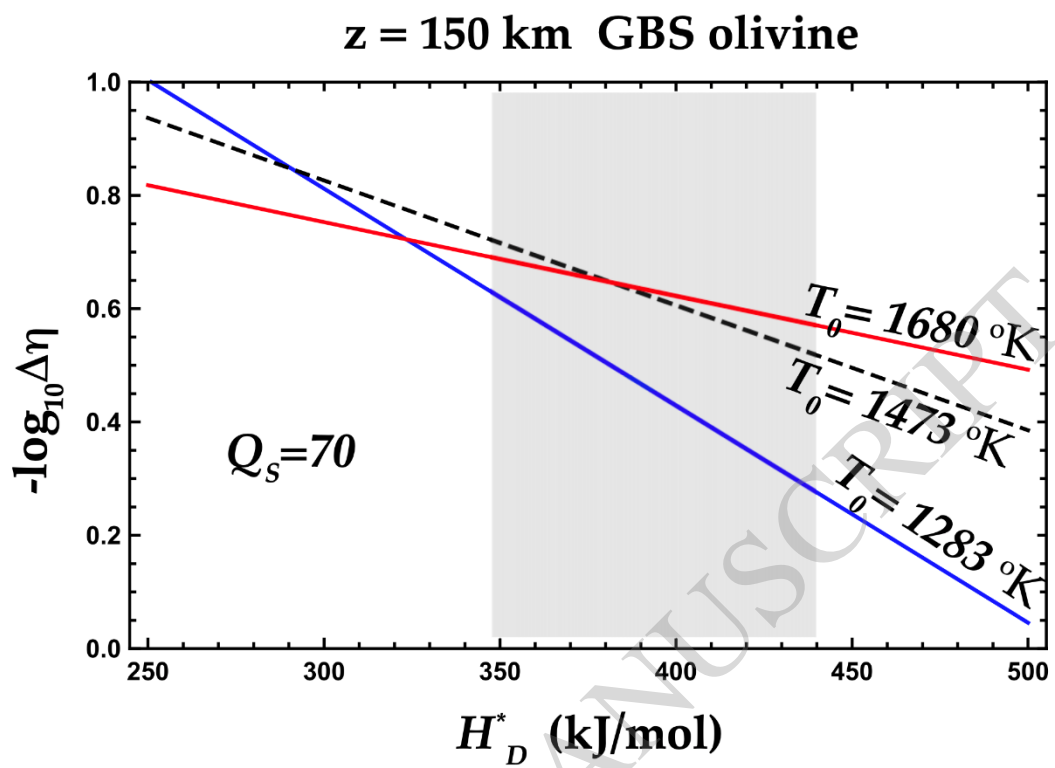


Figure 5

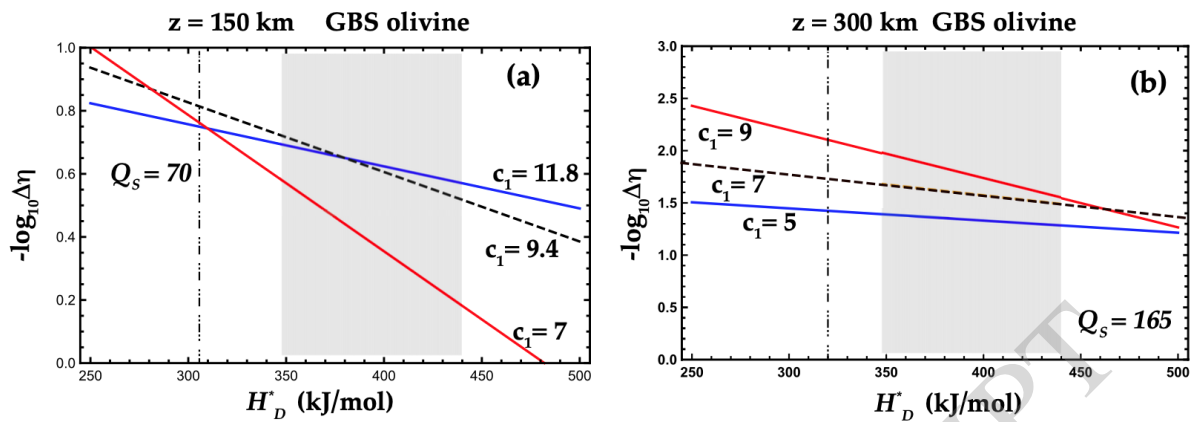


Figure 6

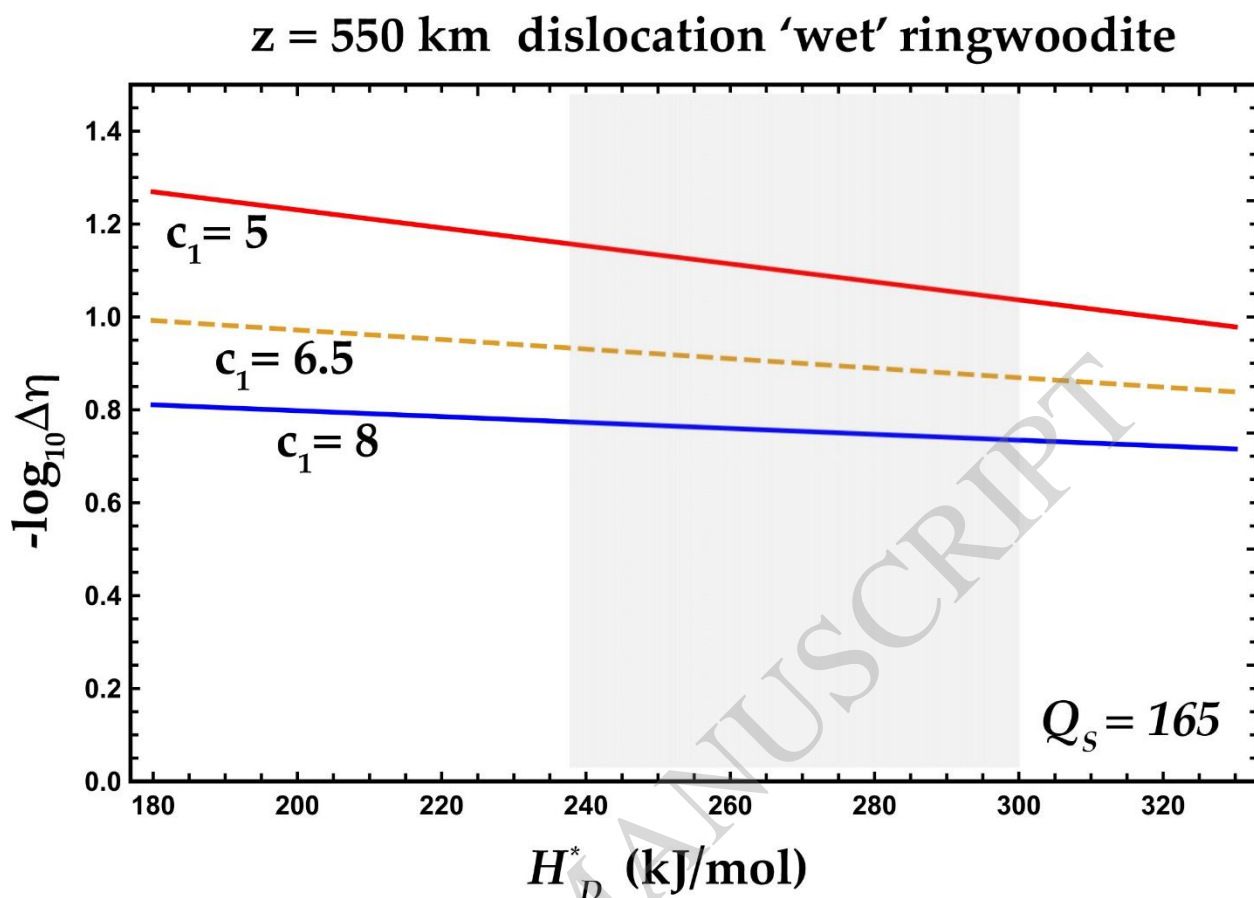


Figure 7

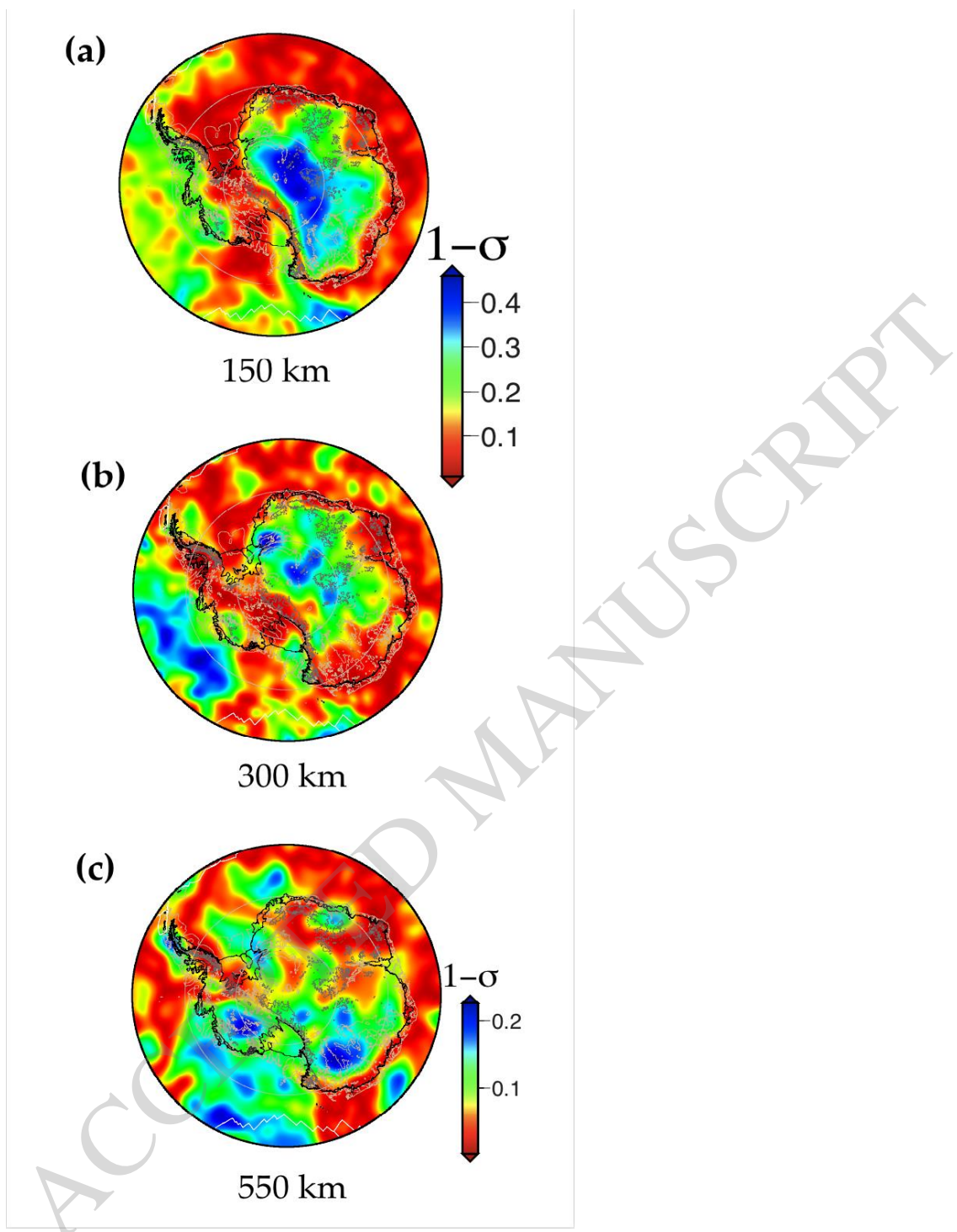


Figure 8

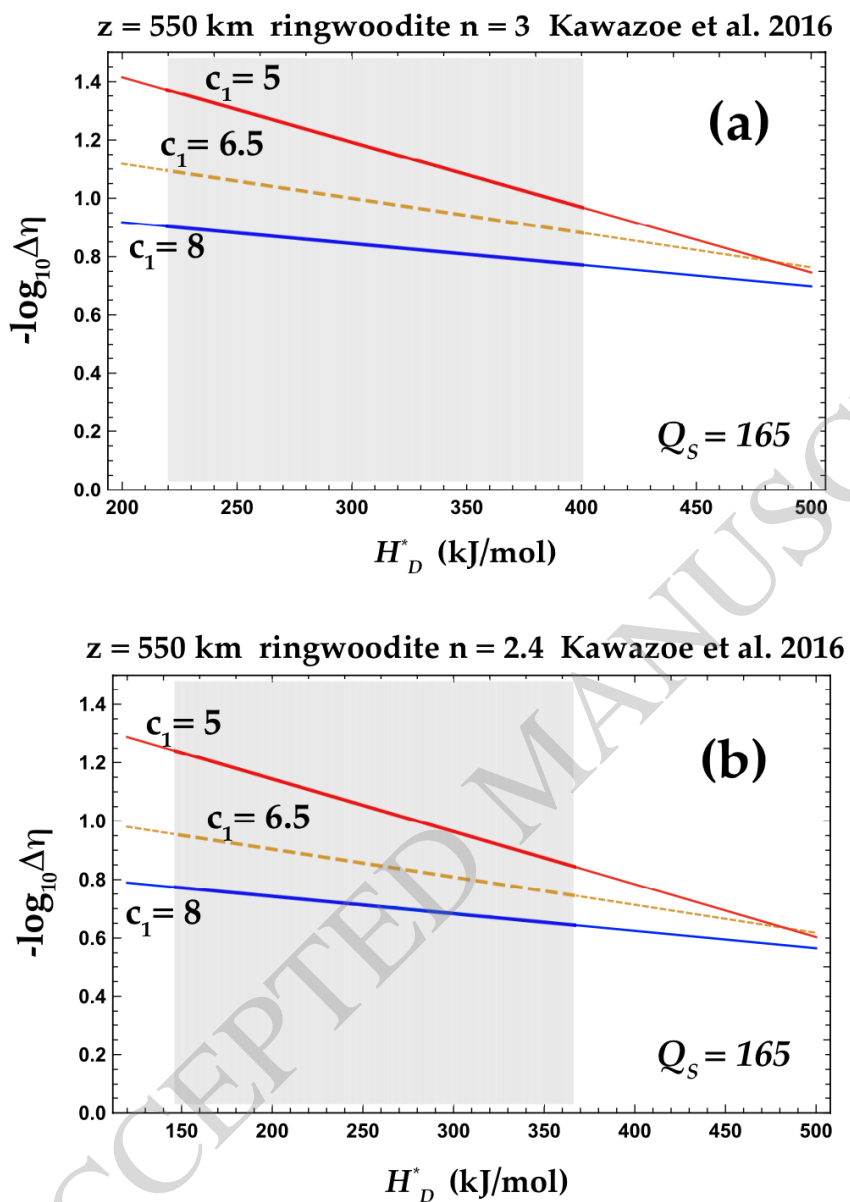


Figure 9

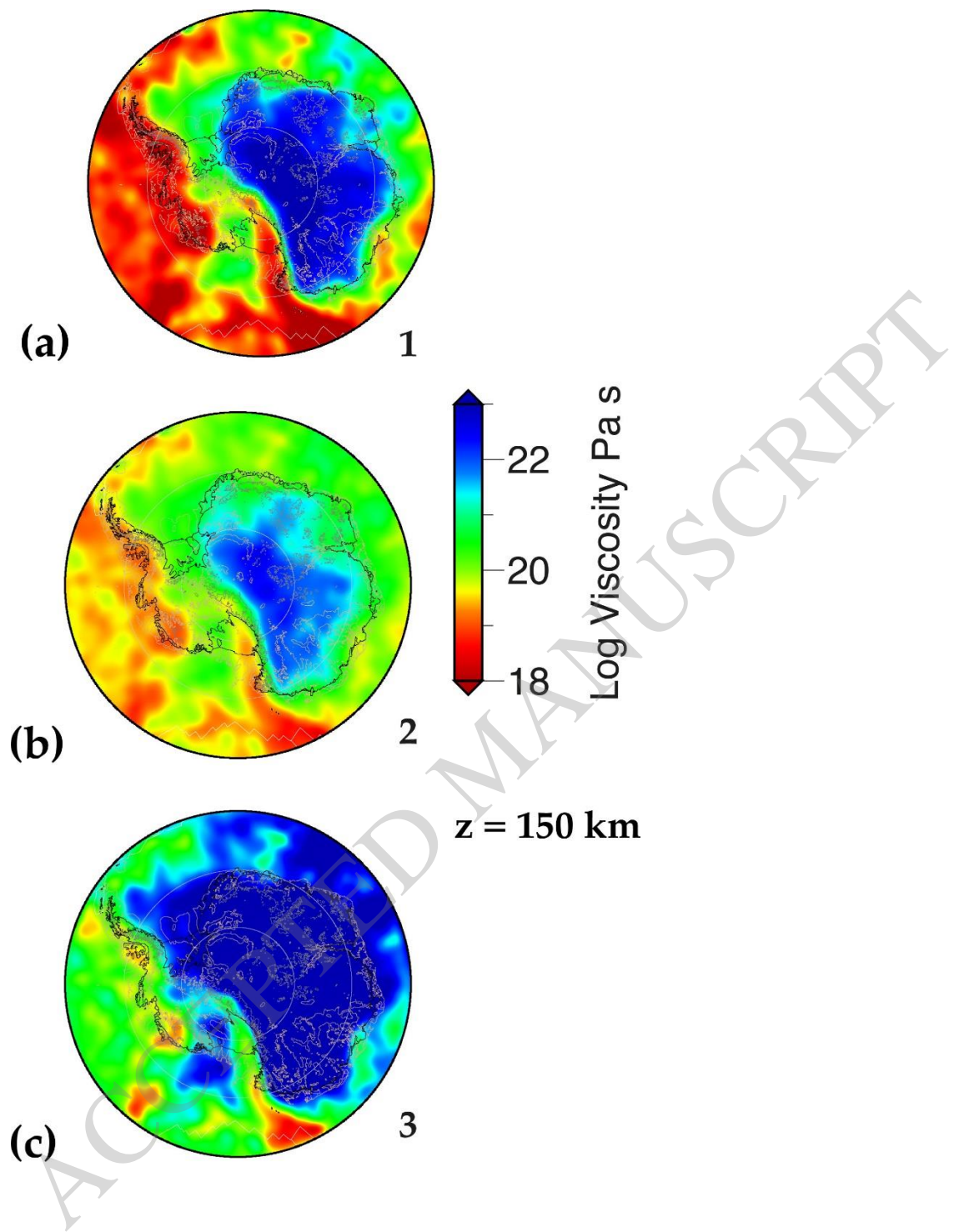


Figure 10

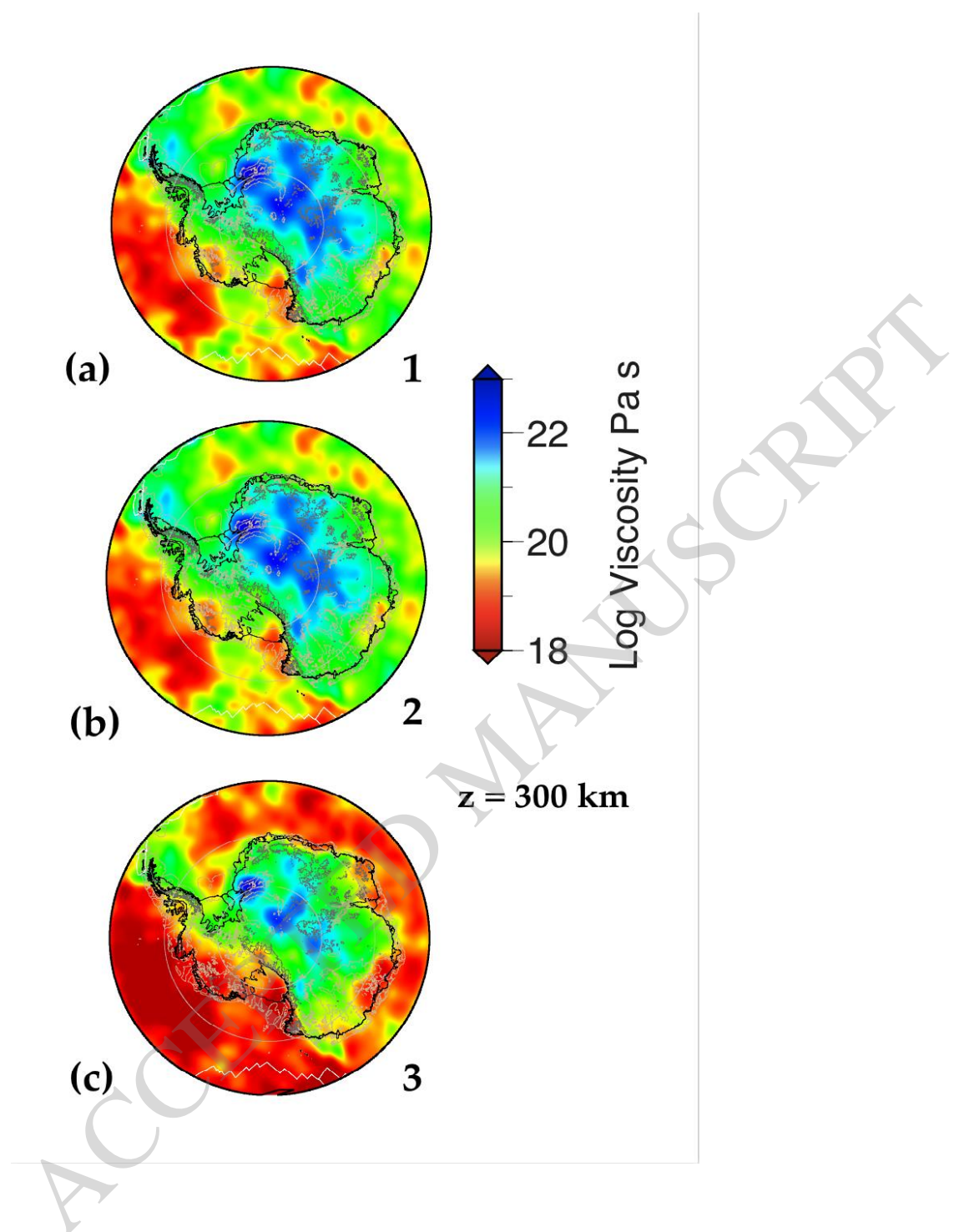


Figure 11

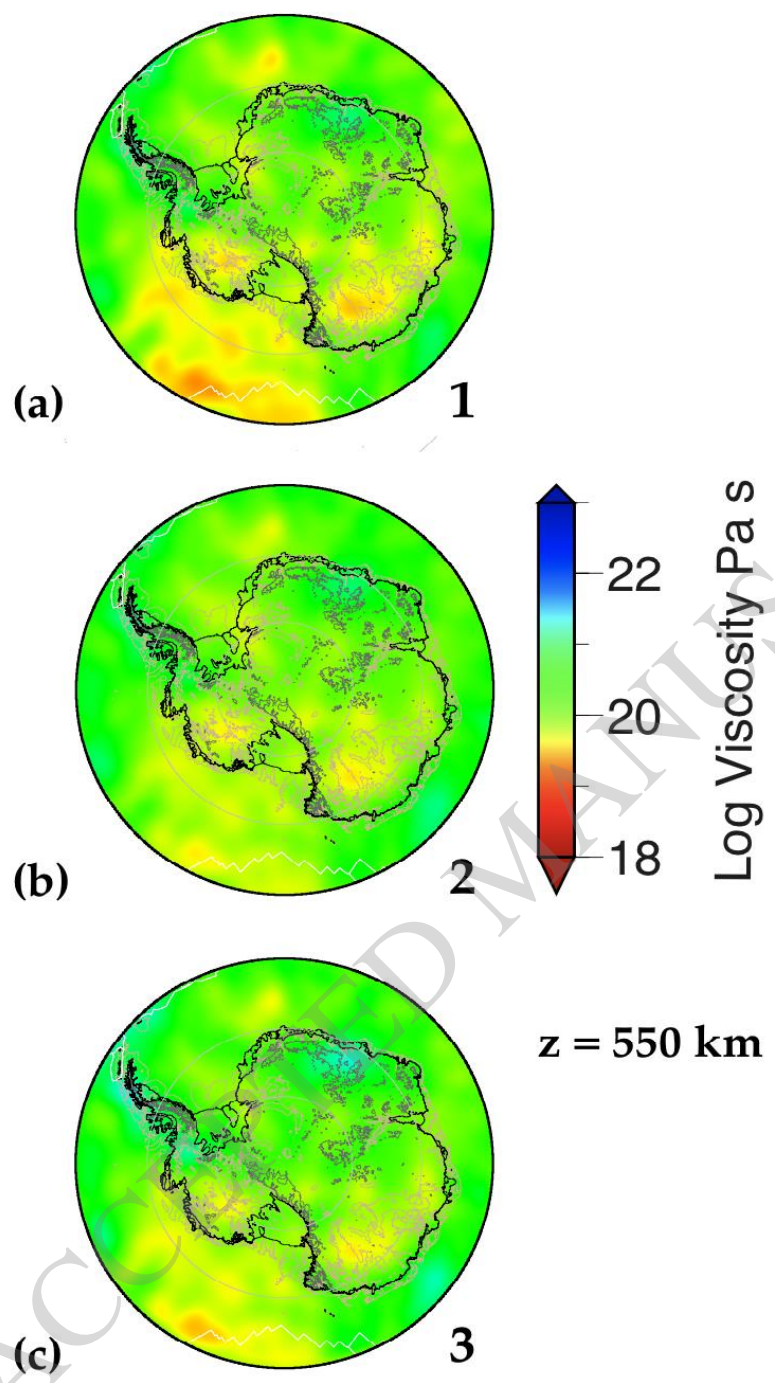


Figure 12

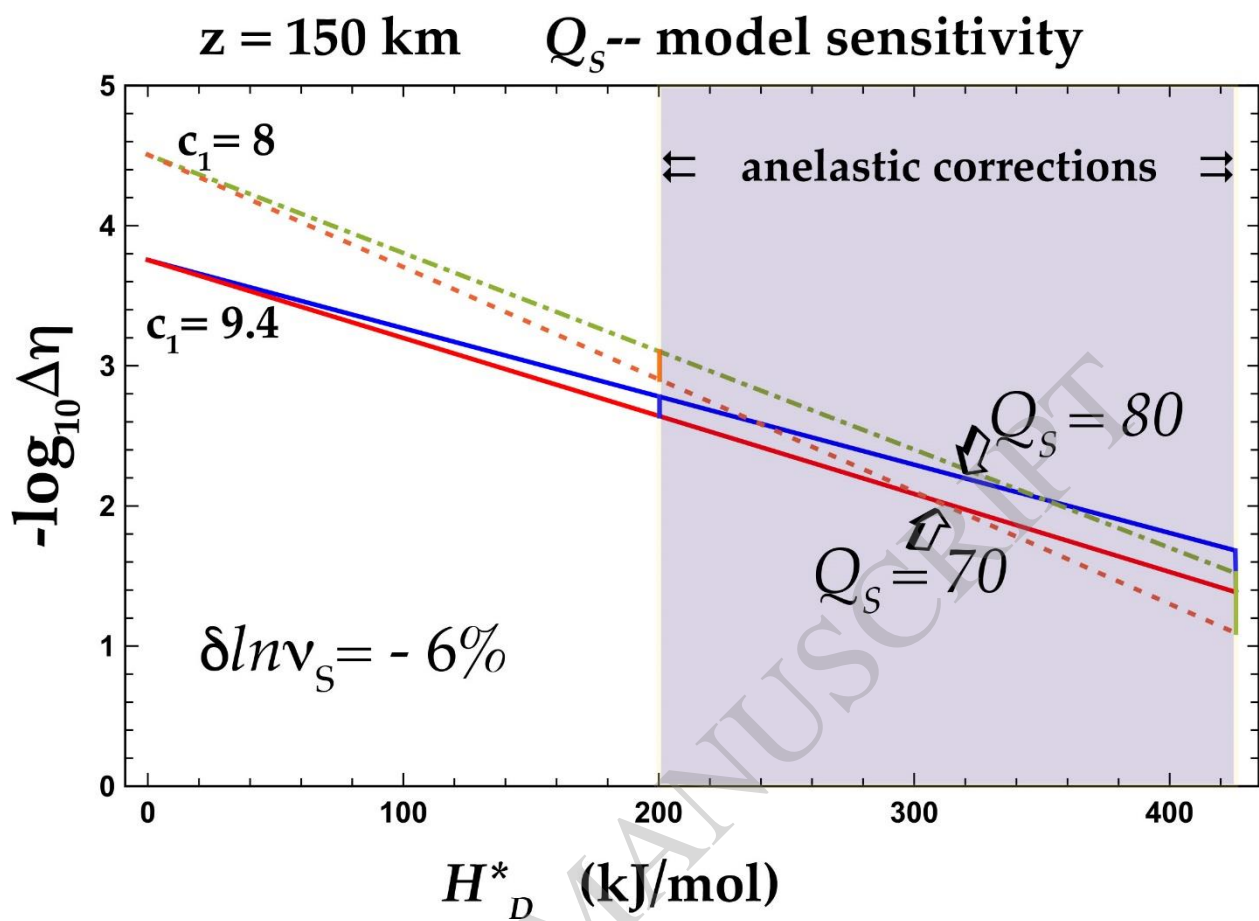


Figure 13

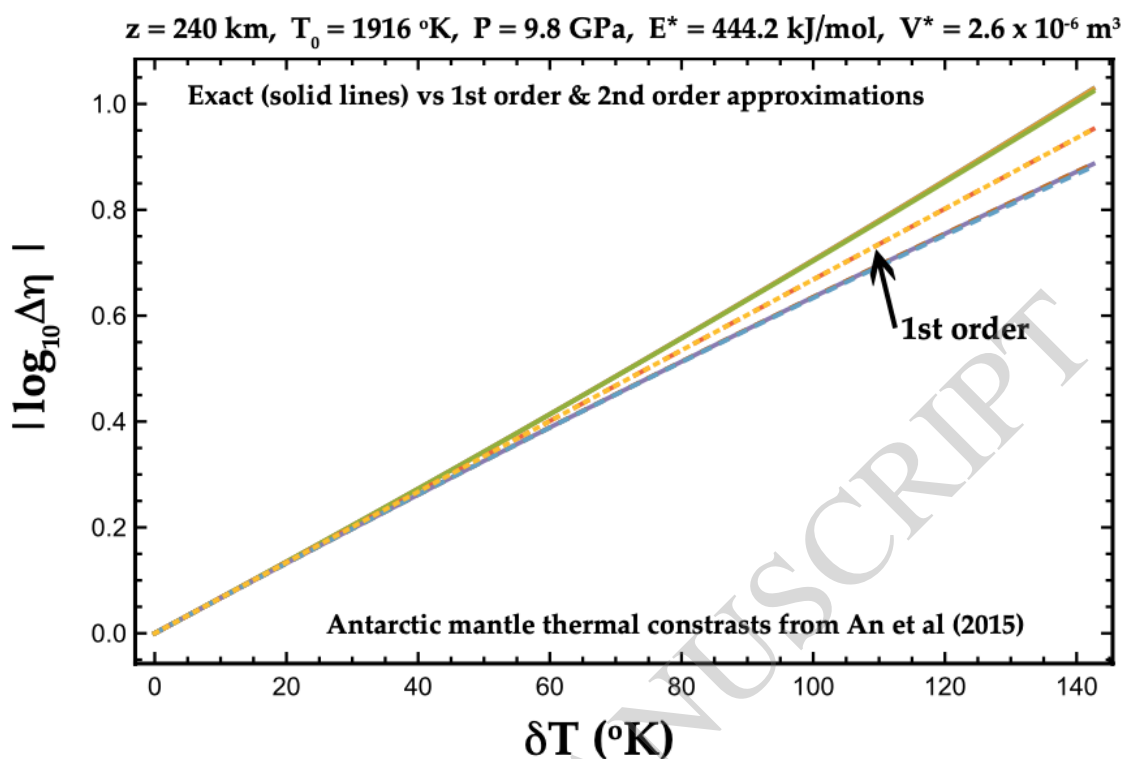


Figure A1

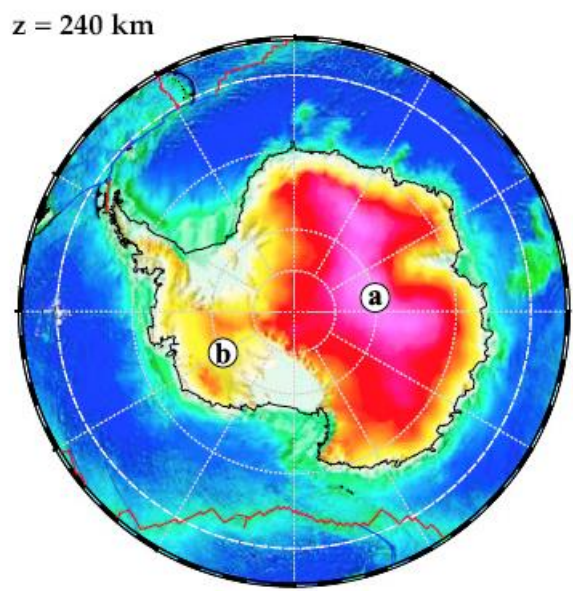


Figure A2